# NUMERICAL SIMULATION OF FLUID FLOW THROUGH POROUS MEDIA USING THE IMMERSED BOUNDARY METHOD

BY

YUYA MATSUMURA

DISSERTATION

Submitted in partial fulfillment of the requirements
for the degree of Doctor of Philosophy in Aerospace Engineering
in the Graduate College of the
University of Illinois at Urbana-Champaign, 2014

Urbana, Illinois

Doctoral Committee:

Professor Joanna Austin, Chair
Professor Thomas L. Jackson, Director of Research
Professor Philippe Geubelle
Professor Kenneth Christensen
Professor Daniel Bodony

# Abstract

The ghost cell immersed boundary method coupled with a finite difference based Navier-Stokes solver has been developed. The flow solver is used to analyze the two-dimensional, unsteady and viscous flow at low Reynolds numbers through packings of ordered or disordered arrays of mono-, bi- and polydisperse cylinders and ellipses. A variety of verification problems are presented. The macroscopic permeabilities of the packs are computed from the well-known Darcy's law in the low Reynolds number regime, and have been investigated through various geometric parameters, such as porosity, polydispersity, numeric distributions of unique diameters and aspect ratios. It is shown that the permeability can be correlated to the statistical descriptor of the underlying microstructure, the mean shortest Delaunay edge. The permeability, which is a function of the geometric parameters, collapses onto the monodisperse data with proper scalings, and the monodisperse data can be then fitted with a universal prediction curve. The effect of the Reynolds numbers in the inertial flow regime has also been studied. The inertial effect at moderate Reynolds numbers can be correlated through a modified friction factors with a parameter, which is also a function of porosity.

# Acknowledgement

The author's first and greatest thanks is to his advisor, Dr. Thomas L. Jackson. This is for his advice, suggestions and guidance in many aspects of his research and dissertation from the first point until its completion, which would not have been possible without his aid.

The author is also thankful to the present and past members of the research group of Dr. Jackson: Dr. Victor Topalian, Dr. Ju Zhang, Mr. Guilherme Amadio and Mr. Jenne Denis, who gave the author various supports and discussions for the code development and testing as well as providing a packing code. This work was supported in part by the Defense Threat Reduction Agency, Basic Research Award No. HDTRA1-13-0010, to University of Illinois at Urbana-Champaign; Dr. Suhithi Peiris, program manager.

Finally, the author is deeply grateful to his mother, who has been patiently supporting and encouraging him in many ways from the beginning of his career. He also would like to pray for his father and grandfather, who inspired him into engineering in his childhood, and passed away before seeing his achievement in the field.

# Contents


**1 Introduction . . . . . 1**
1.1 Motivation and Background . . . . . 1
1.2 Immersed boundary method . . . . . 8
1.2.1 Continuous forcing approach . . . . . 9
1.2.2 Discrete forcing approach . . . . . 10
1.2.3 Choice for the current work . . . . . 12
1.3 Objective and thesis outline . . . . . 13

**2 Numerical method . . . . . 14**
2.1 Governing equations . . . . . 14
2.2 Immersed boundary method . . . . . 17
2.3 Boundary conditions . . . . . 21
2.4 Packing algorithm . . . . . 21
2.5 Figures . . . . . 23

**3 Validation and Verification . . . . . 24**
3.1 Taylor-Green vortex and driven cavity flow . . . . . 24
3.2 Convergence of the ghost cell scheme . . . . . 25
3.3 Flow past an object . . . . . 26
3.4 Flow through a periodic array of cylinders . . . . . 29
3.4.1 Array of monodisperse cylinders . . . . . 30
3.4.2 Array of bidisperse cylinders . . . . . 30
3.5 Summary . . . . . 31
3.6 Figures . . . . . 33

**4 Flow through random packs of particles . . . . . 41**
4.1 Problem outline . . . . . 41
4.1.1 Formulation . . . . . 41
4.1.2 Representative volume element . . . . . 43
4.2 Results for monodisperse cylinders . . . . . 44
4.3 Results for bidisperse cylinders . . . . . 46
4.3.1 Permeability and flow field . . . . . 46

4.3.2 Carman-Kozeny equation . . . 50
4.4 Results for polydisperse cylinders . . . 51
4.4.1 Pack properties . . . 51
4.4.2 Results and scaling . . . 52
4.4.3 Statistical analysis and rare events . . . 53
4.5 Results for ellipses . . . 55
4.5.1 Regular array . . . 55
4.5.2 Random packs . . . 56
4.5.3 Permeability and length scales . . . 56
4.5.4 Carman-Kozeny equation . . . 58
4.6 Inertial effect in non-Darcy's regime . . . 58
4.6.1 Monodisperse cylinders . . . 59
4.6.2 Non-monodisperse cylinders . . . 59
4.7 Figures . . . 62

**5 Conclusions and future work . . . 89**
5.1 Summary and conclusions . . . 89
5.1.1 The ghost cell immersed boundary method . . . 89
5.1.2 The permeability of random packs . . . 90
5.2 Future work . . . 92

**Appendix A Drag computation . . . 93**

**Appendix B Lubrication theory . . . 96**

**Bibliography . . . 101**

# Chapter 1

# Introduction

This dissertation focuses on the numerical simulation of fluid flow through porous media. Fluid flow in porous media has been studied for decades, yet due to wide variations in typical morphologies, it is still difficult to understand flow properties of various materials and its relationship to material characteristics. Accurate predictions of the macroscopic properties depends critically on the details of the microstructure. In general, the microstructure is considerably complex, consisting of random polydisperse, non-spherical particles. We solve the unsteady, two-dimensional Navier-Stokes equations on a staggered Cartesian grid and use the immersed boundary method to treat internal flow properties. To generate complex microstructures, we use the packing code previously developed at Illinois.

## 1.1 Motivation and Background

Porous media, such as fibrous materials and packed beds of particles, have wide applications in many industrial, chemical, biological, environmental and mechanical fields. In oceanography, understanding the water flow along coastal regions is important for wetland protection, restoration, navigation, and effects of storm surge. In the mathematical and numerical modeling of coastal flow, the porous medium is taken to be the vegetated region along the coastline [1]. In the chemical industries, randomly packed beds can be found in a number of

different applications, such as separation and purification, filtration, and reaction [2]. In coal burning plants, where the coal bed is a randomly packed bed, certain characteristics of the coal feed play important roles in determining the gasifier (used for the conversion of coal to synthesis gas) behavior and operational stability [3]. For example, it is well known that the coal particle size distribution determines not only the system stability, but also has an effect on chemical kinetics and hydrodynamic behaviors such as the pressure drop over the bed and the flow distribution through the bed. As an example of the use of random packed beds, the plants in South Africa convert more than 26 million tons of coal per year to synthesis gas [3]. Depending on the process, the Reynolds number can vary over a wide range of values, from creeping flow to fully turbulent flow. It is therefore important to understand the flow in porous media, and to relate the microstructure of the material to the performance of the particular application of interest.

Correlations have been popular for predicting the pressure drop and the velocity in flows through porous media. For example, Darcy [4] was one of the earlier pioneers in the subject, who carried out extensive experiments and proposed the correlation

$$\frac{\Delta p}{L} = \frac{\mu}{K}\langle u \rangle, \tag{1.1}$$

where $\Delta p$ is the pressure drop (difference) across the porous material, $L$ the material length over which the pressure drop is measured, $\langle u \rangle$ the superficial fluid velocity, $K$ the permeability, and $\mu$ the viscosity. Darcy's law is a linear correlation relating the superficial fluid velocity to the pressure drop across the media using the proportionality $\mu/K$.

Although Darcy's law is commonly used in many applications, it is also known that it is valid only in the Stokes limit. At higher Reynolds numbers, the relation of the pressure drop and the superficial velocity is found to be nonlinear due to the presence of inertial effects. To correct for this, Forchheimer [5] proposed a quadratic correlation of the form

$$\frac{\Delta p}{L} = \frac{\mu}{K}\langle u \rangle + \beta \rho \langle u \rangle^2, \tag{1.2}$$

where $\rho$ is the fluid density and $\beta$ is another empirical, material-dependent parameter. The equation is the sum of the viscous resistance giving rise to the linear term and an inertial resistance giving the quadratic term. The Forchheimer equation is useful for modeling many nonlinear porous flows such as gas flow in oil recovery operations [6], combustion gas flow in burning beds of coal [7], and high speed compressible flow in porous media [8]. For typical low porosity materials where the fluid velocity is low, the Forchheimer equation reduces to Darcy's law, but in some applications the inertial term (the second term of equation (1.2)) can be significant. For anisotropic materials $K$ and $\beta$ are taken to be tensors.

The Forchheimer equation is valid over a wider range of Reynolds number when compared to Darcy's law, but it still requires experiments to determine the parameters. Ergun [9] established a semi-empirical, generalized form of the Forchheimer equation for homogeneous packed beds of spheres, by combining two asymptotic solutions, one for low Reynolds number regime and one for the high Reynolds number regime. The Ergun equation is given as

$$\frac{\Delta p}{L} = A\frac{(1-\sigma)^2}{\sigma^3}\frac{\mu\langle u\rangle}{D^2} + B\frac{(1-\sigma)}{\sigma^3}\frac{\rho\langle u\rangle^2}{D}, \tag{1.3}$$

where $\sigma$ is the porosity of the material, $D$ the particle diameter, and $A$ and $B$ are curve fitting parameters. After a series of experiments, Ergun concluded that the best fit would be yielded by $A = 150$ and $B = 1.75$. The Ergun equation has been very successful in chemical engineering; examples of its use may be found in Perry's Chemical Engineer's Handbook [10].

It is common to rewrite the above equations in terms of a non-dimensional friction factor $f_D$ and a Reynolds number $Re_p$. For example, in [11] the authors defined the friction factor as

$$f_D = \frac{\Delta p}{L}\frac{D}{\rho\langle u\rangle^2}\frac{\sigma^3}{1-\sigma}. \tag{1.4}$$

With the friction factor known, Ergun's equation and the Forchheimer equation can be

rewritten as

$$f_D = \frac{150}{Re_p} + 1.75 \tag{1.5}$$

and

$$f_D = \frac{1}{Re_p K'} + \beta' \tag{1.6}$$

respectively, where $K' = K/D^2$ is the non-dimensional permeability parameter and $\beta' = \beta D$ the non-dimensional coefficient. Here, the particle Reynolds number is based on the porosity and is defined as $Re_p = \rho \langle u \rangle D/\mu(1-\sigma)$ [11].

Recent experimental and numerical work have revealed that the constants appearing in Ergun's and Forchheimer equations may vary significantly due to the material microstructure, such as particle shape, size distribution, and orientation. For example, one shortcoming of the Ergun equation (1.3) is that it uses a single parameter $D$ to characterize various particle shapes and distributions, and therefore it is not able to predict pressure drops for packs of highly polydisperse particles. Thus, MacDonald *et al.* [12] proposed generalizing Ergun's equation by replacing the particle diameter with an equivalent particle diameter. Additional numerical work has been carried out demonstrating that Ergun's equation fails to predict the correct pressure drop for highly polydisperse particles. An example of non-spherical particles is the use of plates with low thickness-to-width ratio, such as wood chips used in the paper pulp making industry [13]. Here, a significant amount of the surface area overlaps and is not reached by the flow. Another example is that of [3], who used numerical simulations to show that the pressure drop across a bed of coal particles (randomly shaped polyhedra generated using Voronoi tessellation) changes by more than a factor of 2 when the equivalent particle diameter is kept constant while the polydispersivity of the pack changes.

Martin *et al.* [14] examined two-dimensional square and triangular periodic arrays of cylinders under laminar conditions. The authors solved the steady Navier-Stokes equations in the pore region using a finite volume-based numerical method. They showed that Forch-

heimer equation did not fit the data well, and so proposed a linear combination of Darcy's law at low Reynolds numbers and a fit using Forchheimer equation at higher Reynolds numbers. The disadvantage here is the use of two models.

Additional examples of numerical simulations of fluid flow through packed beds include simulations of flow through random packs of two-dimensional monodisperse cylinders at low and moderate Reynolds numbers [15, 16]; modeling of large packed beds of spheres as unit cells, which essentially reduces the computational burden to flow around one sphere [17, 18]; two-dimensional steady flow past a square array of cylinders [19] as well as square and hexagonal arrays of bidisperse cylinders [11]; flow past a square array of cylinders using unsteady LES simulations for high Reynolds number flows [1]; three-dimensional flow through ordered and random packs of particles [2],[20]-[26]; flow and heat transfer with two layers of 5x5 uniform-size spheres [27]; flow through a two-dimensional porous bed with a porosity jump [28]; and two-phase flow through a random bed of spheres [29].

Although Darcy's law in the non-inertial regime appears straightforward to use in predicting macroscopic flow quantities, its use is complicated by the fact that typical porous media has complex microstructures. Little is known about how the microstructure (polydispersity; particle shape; porosity; inter-particle spacing; higher-order statistics) affects macroscopic quantities such as fluid flow and permeability. There have been limited studies on the effect of polydispersity and particle shape on permeability, and we review some of these below. One example of complex microstructures is natural sandstone. The work presented in [30] investigate three-dimensional pore space geometry for three natural sandstones. The geometries were reconstructed using microtomography. Using local porosity distributions and local percolation probabilities, the authors performed quantitative comparisons between experiments with microscopic pore space models across the three samples. However, due to the complexity of the microstructure, fluid flow through the geometries was not considered.

Another study that used microtomography to generate the microstructure is that of [31]. The authors carried out a comparison of digitized pore structures (microtomography images of real lithofacies samples) and numerical reconstruction of rocks to predict material trans-

port properties of complex, heterogeneous rock. They solve Stokes flow in the pore region using a lattice Boltzmann algorithm and compute, among other quantities, the permeability. The results show good agreement between the tomography images and reconstructed samples, demonstrating the potential use of digitized pore samples and numerical simulations.

Still another study is that of [32], who used both microtomography of a sand sample and an artificial method using a Boolean model for generating various microstructures. The Boolean model is based on a random distribution of overlapping ellipsoids whose size and shape were chosen according to some criteria. The work mainly focused on geometric parameters called Minkowski functionals (volume, surface, curvature, and connectivity) and their effects on permeability. The flow through the samples was solved using a lattice-Boltzmann method. The results show that the Minkowski functionals are not sufficient for the characterization of the geometric properties, whereas the permeability of the scanned and artificial samples were in good agreement.

Another example is that of [3], who used numerical simulations to show that the pressure drop across a bed of coal particles (randomly shaped polyhedra generated using Voronoi tessellation) changes by more than a factor of two when the equivalent particle diameter is kept constant while the polydispersivity of the pack changes. However, this work was limited to only two particle size distributions.

Garcia *et al.* [24] computed the permeability as a function of particle shape and polydispersity for five three-dimensional random packs of non-spherical particles. The particle shape and grain size distribution for three samples were chosen to mimic real sand, while monodisperse and bidisperse packs were generated for comparison. Stokes flow was solved in the three-dimensional pore region by use of a finite element method. Their results show that the permeability is strongly affected by porosity and mean grain size, but particle shape and size distributions have only a small effect.

The permeability and tortuosity was computed for random packs of polydisperse disks in [33]. The particle size distributions were calculated by a Weibull distribution, and random packs were then generated by a discrete element method. The number of different particle

sizes used in the study were chosen according to a gradation curve (cumulative distribution function); only four particle diameters were considered for the steepest gradation, while six particle diameters was taken for the slowest gradation curve. The fluid flow in the pore regions was solved by the lattice Boltzmann method, and the results were correlated via either the Hazen or the Carman-Kozeny equation. The results demonstrated the effects of porosity and specific surface ratio on the permeability.

There have been very few studies on the effect of particle shape on macroscale quantities. To determine the effect of particle shape, Schwartz and Banavar [34] began with three-dimensional packs of polydisperse spheres, and then generated packs of oblate spheroids by stretching the pack in one direction. The authors showed that the particle shape had a strong effect on the permeability anisotropy. A similar method for constructing packs was carried out by Pilotti [35], who used linear and trigonometric mappings to generate packs of ellipses and arbitrarily shaped particles from random packs of spheres, respectively. Using a sequential deposition algorithm, where particles are dropped one at a time under the effect of gravity, Coelho *et al.* [36] generated random packs of monodispersed spheres, ellipsoids, and other analytical shapes. The authors showed that for the packs studied, the permeability was roughly independent of the particle shape. Lehmann *et al.* [32] used overlapping ellipsoids to generate packs that statistically represent tomography images of sand samples. The authors found that the permeability was a function of porosity and surface area. Finally, Garcia *et al.* [24] constructed random packs of non-spherical particles using the discrete element method (DEM). The shape of real particles are determined by scanning, and then modeled using a collection of spheres. Five different packs were examined. The conclusion is that grain shape and size distribution have only a small effect on the permeability. We note that in all of the papers discussed above, results for a single pack realization was discussed. Ensemble averaging was not considered, and so variations in particle locations and orientations was not taken into account. More recently, Yazdchi *et al.* [37, 38] considered cylinders in square and hexagonal arrays, and ellipses and squares in a square array. For squares and ellipses, the orientation angle was varied. At high porosities, particle shape

(circles, squares, and ellipses with aspect ratio of 2) and orientation were found to have little effect on the normalized permeability. At lower porosities the orientation does, however, have an effect on permeability. For ellipses, the permeability is also affected by the aspect ratio. In addition, the tortuosity is found to be a function of particle shape, orientation, and porosity.

An interesting concept in coupling the microscale to the macroscale is to correlate the normalized permeability to some statistical descriptor of the underlying microstructure. This was recently considered for two-dimensional random packs of monodisperse cylinders [37]-[42]. In [39], the authors find that a correlation exists between the permeability and the mean nearest inter-fiber spacing, which takes into account the fluid space between two fibers. In [40], the authors characterize the flow using Delaunay triangulation. In the other works the authors characterize the packs using particle nearest neighbor distances, Delaunay triangulation, and Delaunay edges. Physically, the line segments formed by nearest neighbors or shortest Delaunay edges define, roughly speaking, the edges of two-dimensional channels where the fluid will most likely flow (fast). By examining random packs the authors show that (i) the permeability does not scale with the first nearest neighbor length scale; (ii) the second nearest neighbor is roughly equal to the shortest Delaunay edges; and (iii) a universal curve exists that relates the permeability to the second nearest neighbor.

## 1.2 Immersed boundary method

In this research, we use the ghost cell immersed boundary (IB) method for solving flows with immersed objects. The cell immersed boundary method refers to a group of methods that treat the boundary of immersed bodies on a fixed, non-body conformal grids; the ghost cell immersed boundary method is a variant of the immersed boundary method. Due to its nature, the immersed boundary method do not require the time-consuming process of building non-regular body conforming grids. This is highly advantageous especially when there is a need to handle complex, multiple shapes in the flow and/or moving boundaries;

although moving boundaries are not considered in the current work.

The immersed boundary method was first introduced by Peskin [43] for blood flow in a human heart. Since then, there have been various modifications made on this type of method, extending their applications and/or numerical schemes. Variations of IB methods and their applications are extensively reviewed and discussed in Mittal [44], and more recently in Sotiropoulos [**?**]. In the following section, the IB method will be briefly summarized following the categories proposed by [44].

Immersed boundary methods treat the internal flow boundaries indirectly by modifying the Navier-Stokes equations. Depending on the approach, the IB methods can be categorized into two main groups. The first group is referred to as the continuous forcing approach [44]. In this approach, boundary effects are represented by a source term, or forcing function, employed into the original continuous governing equation. The modified governing equation is then discretized accordingly to the numerical method for the problem. The second group is called the discrete forcing approach [44]. In this group, the discretization of the governing equation is performed before imposing the boundary conditions. The immersed boundary is taken into account by modifying the cell structures near the immersed interfaces. Some details and examples of each category will be presented in the following section.

### 1.2.1 Continuous forcing approach

The continuous forcing approach was the original IB method, proposed by Peskin [43][46] for the flow with elastic immersed bodies. This approach introduces the forcing term into the original governing equation, that represents transmission of stress on the immersed elastic bodies to the surrounding fluid. Relating the stress and deformation of the elastic bodies is introduced by a constitutive law, such as Hooke's law. The forces are distributed over the neighbor nodes by the Dirac delta function, which is then replaced by a smooth distribution function. A choice of the distribution function may have a significant impact on the numerical accuracy and stability, so it is a key considering when using this approach.

Although the continuous forcing approach is relatively easy to implement, applying the

approach to rigid bodies raises the numerical problem since the constitutive laws for the forcing term is often not well posed. Alternative approaches by Beyer and Leveque [47] for one-dimensional problems, and Lai and Peskin [48] for two-dimensional problems, treat the forcing term as a restoring force of a spring attached to the immersed boundary. Goldstein et al. [49] developed a technique to use a feedback scheme of the velocity to impose the effect of the rigid immersed boundary, and demonstrated it on two- and three-dimensional flows. Another variant in this category is the penalization method. The forcing term in this method introduces the mask function instead of the Dirac delta function, that models the entire flow as in porous media, where the fluid and solid regions have infinite/zero permeability. Similar to the other continuous forcing approaches, the mask function needs to be smoothly distributed over near-regions of the immersed bodies. Some examples of this method are found in Angot et al. [50] and Khadra et al. [51].

The continuous forcing approach is especially powerful for elastic bodies due to its relative ease of implementation, although application to rigid bodies is still challenging. One drawback is that it requires solving the governing equation inside the immersed body, which may increase the computational cost. This may become significant when the flow field has large areas of immersed boundaries. Another computational drawback is the need for tuning the distribution function and its parameters. This may have a negative impact on accuracy and/or stability. For the stability analysis of the continuous forcing approach, readers may refer to Stockie and Wetton [52], [53]). Peskin [54] has also presented reviews and applications of this category of the IB methods.

### 1.2.2 Discrete forcing approach

The discrete forcing approach imposes the immersed boundary onto the discretized governing equations by modifying the local nodes in the direct vicinity of the immersed boundaries. This approach does not require the distribution of the forcing term as the continuous forcing approach does, therefore it is suitable for high Reynolds number flows which requires high resolution near boundary surfaces.

One of the methods that belong to this category is the ghost cell method. It was first proposed by Mohd-Yusof [55] coupled with the spectral methods, and later extended to other schemes, such as work by Verzicco [56] using a finite difference scheme, and by Fadlun [57] for large eddy simulations. A key idea of the ghost cell method is to impose the immersed boundaries implicitly through the ghost nodes; i.e., grid nodes that are immediate neighbors of the immersed boundaries. The ghost node is usually defined as a node in the solid with at least one neighboring node in the fluid. The flow variables on the ghost nodes are updated by interpolation schemes using surrounding flow nodes and the given boundary condition.

A type of the interpolation scheme for the ghost nodes is a choice for the method, and is a subject of various research. For example, Majumdar [58] discussed a linear, quadratic and bilinear interpolation in two-dimensional flows. Tseng and Ferziger [59] has also tested the linear and quadratic interpolation schemes. A simple and frequently used scheme is the bilinear interpolation for two-dimensional flows (or trilinear in three-dimensional flows) that ensures second-order accuracy, but higher order of accuracy is also applicable if needed. See Zhang and Zheng [60], Mittal et al [61], Wang and Pletcher [62], and Ghiast et al. [63], for examples.

Another approach in this category is called the cut-cell method. It was first proposed by Clarke [64] for inviscid flow, and later extended to viscous flows by others, such as Ye et al. [65] and Udaykumar et al. [66]. The cells cut by the immersed boundaries are reshaped either by removing the parts of the cell in the solid, or by combining with the neighboring cells. Reshaping of the cells near the immersed boundaries forms the trapezoidal control volume. The fluxes on the reshaped cut-cells for the finite volume discretization are then interpolated from the neighbor regular cells and the immersed boundary conditions. A major advantage of this approach is that it strictly ensures the conservation laws of mass and momentum locally and globally. A drawback is the difficulty of imposing the method in three-dimensional problems, due to the possible complex polyhedral shapes of the cut-cells. Some attempts to apply the cut-cell method to three-dimensional flows are found in Kirkpatrick et al. [67] and Meyer et al. [68].

The discrete forcing approach is highly advantageous for its capability of capturing the sharp interfaces of the immersed bodies, since it does not need to distribute the artificial forces to the surrounding nodes but rather treats only the nodes of the direct neighbor to the immersed surfaces. This feature also eliminates the need for solving the governing equations inside the immersed bodies, reducing the computational cost significantly for some problems. Another advantage is that it does not require user-specified parameters or tuning, which can cause stability constraints on the continuous forcing. One major drawback is that the implementation of the discrete forcing approach is not as straightforward as the continuous forcing. Also some of the direct forcing methods have difficulty in implementation in specific problems, such moving boundaries and three-dimensional flows with the cut-cell method.

### 1.2.3 Choice for the current work

For the scope of the current work, the ghost cell method is selected to treat the immersed bodies for its relative ease of implementation, applicability to two-dimensional as well as three-dimensional problems, relatively cheap computational cost, and capability of handling sharp interfaces. Although a main focus of the current research is two-dimensional flows with smoothly shaped objects such as cylinders and ellipses, future work should be further extended to three-dimensional flows and/or more complicated shapes like polyhedral crystals. Therefore, the ghost cell IB method is found to be suitable also for a scope of the future work. A major drawback of the ghost cell method, difficulty in handling moving boundaries, is not a concern in our work since all of the immersed objects are assumed to be stationary.

To the best of our knowledge, we are not aware of any work that uses the ghost cell IB method for studies of porous media. A majority of the work in this field is adopting a finite element based method ([11][38][94]) or a lattice Boltzmann method ([16][22][69]), with body conforming grids. One purpose of the current work is thus to implement the ghost cell IB method, and to demonstrate its performance on flow through ordered or random packed beds of particles, such as cylinders and ellipses. The standard bilinear interpolation scheme is selected for the ghost cell method as described in [61]. This ensures second-order

accuracy, and the ghost cell method is coupled with a finite-difference based Navier-Stokes solver. Details of the method will be described in Section 2.

## 1.3 Objective and thesis outline

A main objective of this dissertation is to analyze fluid flow through random packs of disks and ellipses, and to establish correlation laws of macroscopic properties such as permeability to the underlying microstructure. A newly developed Navier-Stokes solver, coupled with the ghost cell immersed boundary method, is used to treat objects immersed into the flow. To the best of our knowledge, the immersed method has not been applied to studies in porous media. Thus, another objective of the current work is to demonstrate the method on analysis of the porous media. Once the ghost cell method on the packed bed is developed, it is used for microstructural analysis of the flow through random packs. There has been little work on the analysis of random packs of particles. This work provides some new analysis of these realistic packs, rather than simple regular arrays of circular cylinders.

This thesis is outlined as follows. This Chapter 1 introduced background information and objectives of the current research. In Chapter 2, numerical methods and problem formulation are described in detail. Validation and verification of the numerical method will be presented in Chapter 3. Chapter 4 will discuss the problems and results of flow through random packs of various sizes, polydispersity and shapes. Finally, in Chapter 5, conclusions of the current work will be described and future work will be suggested.

# Chapter 2

# Numerical method

## 2.1 Governing equations

We solve by means of numerical methods the unsteady incompressible Navier-Stokes equations

$$\frac{\partial u_j}{\partial x_j} = 0, \qquad \frac{\partial u_i}{\partial t} + \frac{\partial (u_i u_j)}{\partial x_j} = -\frac{\partial p}{\partial x_i} + \frac{1}{Re}\frac{\partial^2 u_i}{\partial x_j \partial x_j}, \tag{2.1}$$

where $i, j = 1, 2$, $(u_1, u_2) = (u, v)$ are the velocity components in the $x, y$-directions, respectively, $p$ the pressure, and $Re$ the Reynolds number. The variables are scaled by a reference velocity $U_0$, lengths by $L_p$, and pressure by $\rho U_0^2$. The Reynolds number is then defined as $Re = \rho U_0 L_p / \mu$, where $\mu$ is the fluid viscosity assumed constant, $\rho$ the fluid density, and $L_p$ a length scale associated with the microstructure, such as a particle diameter.

The computational domain is discretized using a staggered Cartesian grid with uniform mesh size $dx$ and $dy$. The staggered grid is imposed to prevent odd-even decoupling of the pressure. The $u$-velocity is located at the face-center on horizontal sides, the $v$-velocity is on vertical sides, and the pressure is placed at corners of each cell; Figure 2.2 shows the location of the nodes of the velocity components and pressure. The pressure node is placed at cell corners to take advantage of standard multigrid solvers to apply the boundary conditions

along the unit cell edges, and thus no extrapolation of the pressure at the boundaries is required.

For the temporal integration, the fractional-step method with the four-stage low-dissipation and low-dispersion Runge-Kutta scheme of [70] is employed. A sub-step of each Runge-Kutta stage is given as

$$\frac{\hat{u}_i - u_i^n}{\Delta t} = -\frac{\partial(u_i^n u_j^n)}{\partial x_i} + \frac{1}{Re}\frac{\partial u_i^n}{\partial x_j}, \tag{2.2}$$

with

$$\frac{u_i^{n+1} - \hat{u}_i}{\Delta t} = \frac{\partial p_i^{n+1}}{\partial x_i}, \tag{2.3}$$

where $\hat{u}$ indicates the velocity at a fractional step. At each sub step, the following pressure Poisson equation is solved by an iterative multigrid solver Mudpack [71] to satisfy the constraint of divergence free

$$\begin{aligned} \nabla^2 \hat{p} &= \frac{1}{\Delta t}\frac{\partial \hat{u}_i}{\partial x_i} \\ &= \frac{p_{i+1,j} - 2p_{i,j} + p_{i-1,j}}{dx^2} + \frac{p_{i,j+1} - 2p_{i,j} + p_{i,j-1}}{dy^2}. \end{aligned} \tag{2.4}$$

The convective terms are discretized by a 3rd-order upwinding WENO scheme. WENO, or weighted essentially non-oscillatory, is a numerical scheme for the finite volume or finite difference method derived from the ENO scheme. The ENO scheme chooses a smooth stencil from several possible given stencils to approximate the spatial derivatives. The purpose of this approach is to avoid oscillations near discontinuities such as shocks, providing high-order accuracy and robustness. The WENO scheme, first introduced by Liu et.al [72], constructs a combination of all the possible stencils of the ENO rather than choosing one of them. Each stencil is weighted to construct the target approximation such that with optimal weights it achieve the higher order of accuracy. It has been shown that it is possible to construct a

(2n-1)-th order WENO scheme in the optimal case from the n-th order ENO by maintaining the robustness of the original ENO scheme if the function is smooth. See discussions by Shu et al.[74][73] for more details of the ENO and WENO schemes.

Let $\phi$ be a generic flow variable, then the following operators are introduced

$$\Delta^+\phi_k = \phi_{k+1} - \phi_k, \qquad \Delta^-\phi_k = \phi_k - \phi_{k-1}. \tag{2.5}$$

Then the 2nd-order left-sided ENO scheme takes the following stencils

$$\phi^{-,0}_{x,i} = -\frac{1}{2}\frac{\Delta^+\phi_{i-2}}{dx} + \frac{3}{2}\frac{\Delta^+\phi_{i-1}}{dx}, \qquad \phi^{-,1}_{x,i} = \frac{1}{2}\frac{\Delta^+\phi_{i-1}}{dx} + \frac{1}{2}\frac{\Delta^+\phi_i}{dx} \tag{2.6}$$

Based on the above stencils, the 3rd-order left-sided WENO scheme is reconstructed as

$$\phi^-_{x,i} = \omega_0\phi^{-,0}_{x,i} + \omega_1\phi^{-,1}_{x,i} \tag{2.7}$$

where $\omega_i$ is the weight corresponding to the i-th stencil, that satisfy $\omega_0 + \omega_1 = 1$. By optimizing the weights to yield 3rd-order accuracy, the derivative of the left-sided stencil by the WENO scheme is given as

$$\phi^-_{x,i} = \frac{1}{2dx}\left(\Delta^+\phi_{i-1} + \Delta^+\phi_i\right) - \frac{\omega_-}{2dx}\left(\Delta^+\phi_{i-2} - 2\Delta^+\phi_{i-1} + \Delta^+\phi_i\right), \tag{2.8}$$

where

$$\omega_- = \frac{1}{1+2r_-^2} \quad \text{and} \quad r_- = \frac{\epsilon + (\Delta^-\Delta^+\phi_{i-1})^2}{\epsilon + (\Delta^-\Delta^+\phi_i)^2}. \tag{2.9}$$

Here, $\epsilon$ is inserted to prevent a zero denominator. $\epsilon = 1.0^{-8}$ is selected for the current work. Similarly, the right-sided stencil $\phi_k$, $k = i-1, i, i+1, i+2$ is given as

$$\phi^+_{x,i} = \frac{1}{2dx}\left(\Delta^+\phi_{i-1} + \Delta^+\phi_i\right) - \frac{\omega_+}{2dx}\left(\Delta^+\phi_{i+1} - 2\Delta^+\phi_i + \Delta^+\phi_{i-1}\right), \tag{2.10}$$

where

$$\omega_+ = \frac{1}{1+2r_+^2} \quad \text{and} \quad r_+ = \frac{\epsilon + (\Delta^-\Delta^+\phi_{i+1})^2}{\epsilon + (\Delta^-\Delta^+\phi_i)^2}. \tag{2.11}$$

Upwinding is determined by the velocity sign in the convective terms. Since $u$ and $v$ are on different nodes, the velocity to determine the upwinding is averaged over its neighbor nodes. Readers may refer to Jiang and Shu [73] and Jiang and Peng [75] for more details. The diffusion terms are discretized by the 4th order central difference scheme

$$\phi_{xx,i} = \frac{1}{dx^2}\left\{\frac{4}{3}(\phi_{i+1} - 2\phi_i + \phi_{i-1}) - \frac{1}{12}(\phi_{i+2} - 2\phi_i + \phi_{i-2})\right\}. \tag{2.12}$$

With the discretization described above, the solution has 3rd-order accuracy for the velocities and 2nd-order in pressure. Note that near the immersed bodies, there may be the case that one of the required nodes for the 3rd-order WENO and/or 4th-order central scheme are inside the solid body. In such a case, a simple 1st-order upwinding scheme for the convective terms and a 2nd-order central difference for the diffusion terms are used. This results in loss of order of accuracy to 1st-order locally, but since these regions are limited, it does not appear to affect the overall accuracy significantly; this will be discussed in the validation section.

## 2.2 Immersed boundary method

Implementation of the immersed boundary method begins with identifying the fluid, solid and ghost nodes. The identification of a fluid or solid node begins by defining a level set function $\mathcal{F}(x, y)$ such that a grid point lies in the fluid domain if $\mathcal{F} > 0$ and in the solid domain if $\mathcal{F} < 0$. The fluid/solid boundaries are therefore defined by the level curve $\mathcal{F} = 0$.

Figure 2.1a shows the grid lines of the input levelset function. A value of the function on each node indicates if the node is in the solid or fluid region. The locations of the surface are detected by calculating the coordinates of the points where $\mathcal{F} = 0$ between two adjacent

nodes (one node is in the fluid and the other is in the solid) in either $x$- or $y$-direction along the grid lines. A simple linear interpolation scheme is used to calculate the coordinates of the surface. This procedure yields a set of line segments representing the immersed body surface.

As shown in Figure 2.1b, the boundary intercept BI, the closest point on the surface to the corresponding ghost node (will be defined and discussed below), is then located by drawing a normal line from the ghost node to each line segment of the surface lines. The normal line for BI is selected when it satisfies a) the normal line is the shortest of the normal lines drawn from the node, and b) the normal line intercepts the surface line segment.

Although the ghost cell method implemented here is expected to have second-order accuracy, the surface detection from the levelset function by linear interpolation is only first-order accurate. Therefore, to adequately represent flow boundaries and to interpolate ghost nodes across the fluid/solid boundaries, the level set function needs to reside on a grid that is much finer than the flow domain grid. Numerical tests suggest that a grid that is four times finer than the flow domain is sufficient for convergence; in all of our simulations we take a grid that is six times finer than the flow domain grid.

Figure 2.2 shows a schematic of the ghost nodes, the image points, and the boundary intercepts. A fluid/solid node is a node that lies in the fluid/solid region, respectively. A ghost node (GN) is defined as a node that is located inside the solid body, and at least one of the adjacent north, south, east and west nodes is in the fluid. Since each flow variable is located on a different node due to the staggered grids, the property of the node (fluid, solid or ghost) is determined only by its coordinates. An image point (IP) is defined on the line segment extended from each ghost node normal to the body surface and lies in the fluid domain. A cross point of the line and the body surface is defined as a boundary intercept (BI) located in the midway between IP and GN. A flow variable on IP is calculated by a bilinear interpolation from the values on the surrounding four nodes. A linear interpolation is then applied to determine the values on GN from those on IP and BI (i.e. the given boundary conditions).

Let $\phi$ be a generic flow variable, then the bilinear interpolation is given as

$$\phi(x, y) = C_1 xy + C_2 x + C_3 y + C_4. \tag{2.13}$$

Here, $C_1$ through $C_4$ are unknown coefficients which depend on the variables and the coordinates of the surrounding nodes. They can be determined as

$$\{C\} = \{V\}^{-1}\{\phi\}, \tag{2.14}$$

where

$$\{C\}^T = \{C_1, C_2, C_3, C_4\} \tag{2.15}$$

$$\{\phi\}^T = \{\phi_1, \phi_2, \phi_3, \phi_4\} \tag{2.16}$$

are the vectors of the four unknown coefficients and the variable values on the surrounding nodes. Also,

$$\{V\} = \begin{pmatrix} x_1 x_2|_1 & x_1|_1 & x_2|_1 & 1 \\ & \vdots & & \\ x_1 x_2|_4 & x_1|_4 & x_2|_4 & 1 \end{pmatrix} \tag{2.17}$$

is the Vandermonde matrix which describes the bilinear interpolation. Once these coefficients are obtained, the variables on the image point can be calculated by

$$\phi_{IP} = \sum_{i=1}^{4} \beta_i \phi_i + T.E., \tag{2.18}$$

where $\beta_i$ are the coefficients from the Cs and the coordinates of the image point, and $T.E.$ is a truncation error of order $O(\Delta^2)$. Note that $\beta_i$ are geometry-dependent, so that once the geometry is defined, the coefficients can be determined at the beginning of the computation.

There may appear a case which requires a special treatment when updating the values on GN. One such case is that one of the four surrounding nodes is the ghost cell, which the boundary condition on the BI replaces the row of equation (2.14) corresponding to the ghost cell. Another possibility is that one of the surrounding nodes is another ghost cell. To solve the case, the ghost cells are treated and solved as a coupled set of equations.

Having the values on IPs calculated, the variable on the ghost node is then computed by the linear interpolation on the normal line segment from the obtained image point and the corresponding boundary condition. For Dirichlet boundary conditions for the velocities, the linear interpolation is written as

$$\phi_{BI} = \frac{1}{2}(\phi_{IP} + \phi_{GN}) + O(\Delta l^2), \tag{2.19}$$

where $\Delta l$ is the length of the line segment. This equation leads to

$$\phi_{GN} + \sum_{i=1}^{4} \beta_i \phi_i = 2\phi_{BI}. \tag{2.20}$$

For the pressure, von Neumann boundary conditions on the immersed body are computed by the second-order central difference

$$\left(\frac{\partial \phi}{\partial n}\right)_{BI} = \frac{\phi_{IP} - \phi_{GN}}{\Delta l} + O(\Delta l^2), \tag{2.21}$$

which leads to

$$\phi_{GN} - \sum_{i=1}^{4} \beta_i \phi_i = -\Delta l \left(\frac{\partial \phi}{\partial n}\right)_{BI}. \tag{2.22}$$

At each sub-step of the temporal integration, the variables on the fluid cells are updated by solving the governing equations, and those on the ghost cells are then updated by the above procedures when the boundary conditions are applied. The variables on the solid cells are simply set to be $\phi = 0$. Readers may refer to [44, 61] for more details of the method.

## 2.3 Boundary conditions

In the current work, the immersed bodies are considered to be non-elastic, solid, and stationary objects. Therefore, the non-slip Dirichlet condition is imposed for the velocity components on the surfaces. For the pressure boundary condition, von Neumann condition is usually imposed as

$$\frac{\partial p}{\partial n} \equiv \hat{n} \cdot \nabla p = \hat{n} \cdot \left( \frac{1}{Re} \nabla^2 \vec{u} \right), \tag{2.23}$$

where $\hat{n}$ is the outward pointing normal vector to the boundary. In some works, the right hand side is set to zero (the inviscid limit). These two conditions have been tested on flow past a circular cylinder and through monodisperse packs of random cylinders. The results showed that their difference is negligible (0.1% or less, results not shown). Since our Reynolds numbers are finite, the boundary condition (2.23) is imposed for all simulations.

## 2.4 Packing algorithm

In previous work we described a packing algorithm that can generate packs of polydisperse spheres for mesoscale simulations of solid propellants in an efficient manner [76, 77, 78]. The packing code begins with the basic Lubachevsky-Stillinger (LS) dynamic packing algorithm [79]. The LS algorithm starts by placing $N$ spheres with zero radii (points) at random locations inside a domain of interest. When the spheres have dimensional units associated with the diameters, the packing algorithm uses the largest diameter for nondimensionalization. The packing domain is then scaled to be on the unit cube. The spheres are given random velocities sampled from a Maxwell-Boltzmann distribution at a fixed temperature and are allowed to grow at a specified growth rate. The particles undergo classical (super-)elastic collision dynamics as they grow to fill the space in the domain. The algorithm stops when either a specified packing fraction is reached or when a specified jamming criterion is met. The algorithm was improved by incorporating an event-driven molecular dynamics approach

and a hierarchical cell structure to reduce the overall computational time [78]. Validation of the packing code against existing experimental data of spheres was also reported in [78]. The packing algorithm was recently extended to pack non-spherical convex shapes using a novel method based on level sets [80, 81]. This algorithm extension was necessary because most particles of heterogeneous materials often have non-spherical shapes. Here, we use our packing code to generate two-dimensional random packs of monodisperse and bidisperse cylinders at various porosities. We specify the minimum distance between cylinders to be 0.1 of the radius of the largest particle, necessary for two-dimensional packs to avoid complete blockage of the flow [39]. In the future we plan to use the packing code with suitably defined particles to generate three-dimensional packs that can be used for the study of flow in porous media.

## 2.5 Figures

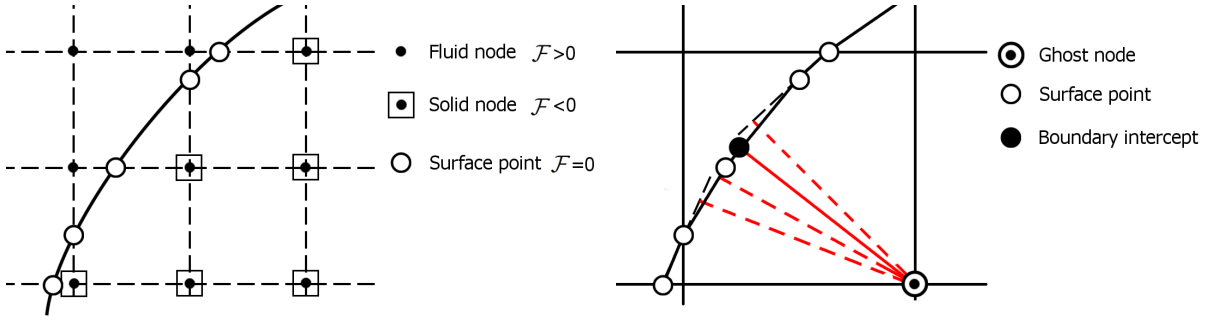


(a) Levelset grid (b) Flow grid

Figure 2.1: Schematics of the input levelset function and detection of the surface. In a) the dashed grid shows the levelset domain and a solid line shows the body surface. In b) the solid grid is the flow domain, red dashed lines are normal lines to each surface segment and a red solid line is a line normal to the boundary intercept.

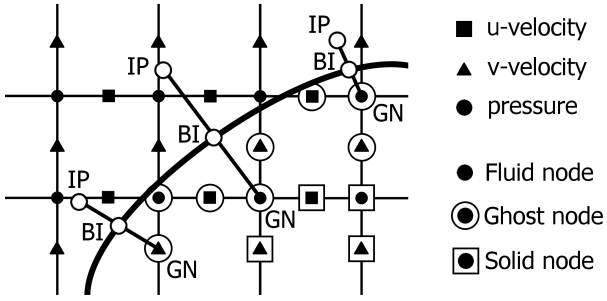


Figure 2.2: Schematic of the flow variables on the staggered grid and the corresponding ghost nodes (GN), image points (IP) and boundary intercepts (BI).

# Chapter 3

# Validation and Verification

This chapter is devoted to the validation and verification of the flow solver. Since the code was newly written for the present work, the Navier-Stokes solver and the ghost cell method are first tested separately. The tests include the Taylor-Green vortex and the driven cavity flow. To verify the coupled solver, we simulate flow flow past an object and flow through a periodic array of cylinders, and compared our results with those reported in the literature.

## 3.1 Taylor-Green vortex and driven cavity flow

The first test case for the Navier-Stokes solver is the Taylor-Green vortex problem, which is one of the few Navier-Stokes problems that has an exact solution. The two-dimensional solutions are given as

$$u(x, y, t) = -\cos(kx)\sin(ky)\exp(-2k^2 t/Re), \tag{3.1}$$

$$v(x, y, t) = \sin(kx)\cos(ky)\exp(-2k^2 t/Re), \tag{3.2}$$

$$p(x, y, t) = -\frac{1}{4}(\cos(kx) + \cos(ky))\exp(-4k^2 t/Re), \tag{3.3}$$

where $k$ is an arbitrary constant. The flow is solved on a square domain with side length of $2\pi$, and the periodic conditions are applied on all the four sides. The problem is solved for $k = 2.0$, $Re = 50$ and $dt = 1.0\text{E-}04$ up to a time of $t = 0.1$ (using 1,000 time steps), with 32 x 32 grid points to 1024 x 1024 grid points, which yields $dx = dy = 1.96\text{E-}01$ to 6.14E-03. The computed solution is compared with the exact solutions by computing the $L_1$ and $L_{max}$ norms of the absolute errors. Figure 3.1 show the error norms as a function of grid size, along with dotted lines showing second-order convergence. The convergence rates of the pressure are approximately 2.0, and those of the velocities are 2.0 to 3.0. It is in good agreement with expectations that the velocities are spatially 3rd-order and the pressure is 2nd-order accurate.

Another benchmark of the Navier-Stokes solver is the driven cavity flow. The free stream condition is imposed at $y = y_{top}$ boundary, and no-slip conditions are applied on the other three sides. The pressure von Neumann boundary condition $\partial p/\partial x = 0.0$ is applied on all four sides of the computational domain. Simulations were carried out for $Re = 100$ and 3200, until the solution reached steady state. Figure 3.2 shows the vorticity of the driven cavity by the current work and by [82]. Similarly, Figure 3.3 are the velocity profiles along the center line of each $x$- and $y$-directions. These plots show good agreement between the current results and previous work at both Reynolds number.

From the results of the TG-vortex as well as the driven cavity flow, we concluded that the Navier-Stokes solver developed for the current work has a good performance with the expected accuracy.

## 3.2 Convergence of the ghost cell scheme

The convergence of the ghost cell scheme (decoupled from the Navier-Stokes solver) is tested next. A domain is set to be a square field with a circular cylinder at its center. The domain size is $2.0 \times 2.0$ times the cylinder diameter. Instead of solving the flow field with the Navier-Stokes equations, the field is expressed by an arbitrary generic function $\phi(x, y)$. $\phi$ is defined

so that it satisfies either a Dirichlet condition or a von Neumann condition, as follows

$$\phi = r - R, \qquad \text{for Dirichlet condition, giving } \phi|_{r=R} = 0; \tag{3.4}$$

$$\phi = r\left(1 - \frac{r}{2R}\right), \qquad \text{for von Neumann condition, giving } \frac{\partial \phi}{\partial r}|_{r=R} = 0. \tag{3.5}$$

Here, $r = \sqrt{x^2 + y^2}$ is the distance from the center and $R$ is the radius of the cylinder. $\phi$ is computed in the fluid domain, and the ghostcell scheme is applied to calculate the values on the ghost cells. The calculations are repeated for each case from grid size $dx = dy =$ 6.25E-02 (32 points in one direction) to 1.95E-03 (1024 points). The values on the ghost cells are compared with the analytical values of equation (3.4) and (3.5) by computing the $L_1$ and $L_{max}$ norms of the absolute errors. Figure 3.4 shows the error norms as a function of the grid size. A dash line shows the second-order convergence. For both Dirichlet and von Neumann conditions, $L_1$ norms remain approximately second-order, with convergence rate ranging from 1.9 to 2.2. $L_{max}$ norms with Dirichlet condition also maintain second-order accuracy (rate of 1.9 to 2.2). Those with von Neumann condition ranges from 1.7 to 2.1. These results suggest that the ghost cell scheme has roughly second-order accuracy up to relatively high resolutions.

## 3.3 Flow past an object

The next tests are to validate the solver on fluid flow with an immersed body. A frequently used benchmark for such problems is flow past a single object. Here, we solve for flow past a circular cylinder, a square rod, and a rod rotated at 45 degrees. The Reynolds number is defined as $Re = U_0 \rho L_p / \mu$, where the reference velocity $U_0$ is the velocity of the uniform inflow and the reference length scale $L_p$ is the height of the object. A flow domain is set to be square with $30.0L_p \times 30.0L_p$, and the center of the object is placed at $(x, y) = (10\,L_p, 15\,L_p)$. The top and bottom boundaries are taken to be periodic for the velocities and the pressure. A uniform inflow of $(u, v) = (U_0, 0)$ is imposed at the inlet, and the convective boundary

[83, 84] is employed for velocity at outflow. The normal pressure gradient is set to zero at the inlet and outlet. Four different resolutions of $dx = dy = 0.156$, 0.078, 0.039, and 0.018 are used to compute the convergence; this resolution gives 7, 13, 25, and 51 grid points along the length scale, respectively.

Results are shown in Figures 3.5 through 3.7, where we plot streamlines for different Reynolds numbers and for the various geometries. For these cases, the flow is steady at Reynolds numbers of 20 and 40, and unsteady at 80.

The drag coefficient $C_D$ is computed for all cases using a control volume analysis (see Appendix A for details). For the steady flows, the length of the bubble (or recirculation zone) in the $x$-direction, $L_w/L_p$, is determined. Here, $L_w$ is measured from the rear of the object. For the unsteady cases, the Strouhal number $St = fL_p/U_0$ is computed, where $f$ is the shedding frequency. In Table 3.1 we compare the drag, length of the recirculation zone and Strouhal number with a number of previous numerical studies and find that our values compare very favorably. The table also shows that our numerical method converges as the grid is refined.

| | | Re=20 | | Re=40 | | Re=80 | |
|---|---|---|---|---|---|---|---|
| | | $C_D$ | $L_w/L_p$ | $C_D$ | $L_w/L_p$ | $C_D$ | $St$ |
| Circular cylinder | Dennis and Chang [85] | 2.05 | 0.94 | 1.52 | 2.35 | - | - |
| | Ye et al [86] | 2.03 | 0.92 | 1.52 | 2.27 | 1.37 | 0.15 |
| | Wang and Jackson [87] | 2.07 | 0.93 | 1.54 | 2.35 | 1.32 | 0.147 |
| | $dx = dy = 0.156$ | 2.07 | 1.21 | - | - | - | - |
| | current $dx = dy = 0.078$ | 2.03 | 0.94 | 1.55 | 2.29 | 1.39 | 0.156 |
| | $dx = dy = 0.039$ | 2.05 | 0.93 | 1.55 | 2.31 | 1.38 | 0.157 |
| Square | Okajima [88] | 2.09 | - | 1.65 | - | 1.46 | 0.12 |
| | Robichaux [89] | - | - | - | - | 1.54 | 0.14 |
| | Sharma and Eswaran [90] | 2.43 | 1.36 | 1.81 | 2.81 | 1.53 | 0.14 |
| | $dx = dy = 0.078$ | 2.37 | 1.37 | 1.74 | 2.98 | 1.64 | 0.13 |
| | current $dx = dy = 0.039$ | 2.33 | 1.33 | 1.73 | 2.82 | 1.54 | 0.14 |
| | $dx = dy = 0.019$ | 2.34 | 1.34 | 1.74 | 2.85 | 1.53 | 0.14 |
| Square rotated 45 degrees | Yoon *et al.* [91] | 1.99 | 0.99 | 1.50 | 2.69 | 1.66 | - |
| | $dx = dy = 0.078$ | 1.90 | 0.78 | 1.44 | 2.15 | 1.47 | 0.18 |
| | current $dx = dy = 0.039$ | 2.04 | 1.06 | 1.56 | 2.65 | 1.62 | 0.17 |
| | $dx = dy = 0.019$ | 2.06 | 1.13 | 1.58 | 2.82 | 1.66 | 0.17 |

Table 3.1: Drag coefficients $C_D$, wake bubble length $L_w/L_p$, and Strouhal number $St$ of flow past a cylinder, square rod, and square rod rotated 45 degrees.

## 3.4 Flow through a periodic array of cylinders

Additional verification tests are carried out by comparing our numerical solutions to those presented in [11]. In this work the authors carried out two-dimensional numerical simulations for flow through monodisperse and bidisperse packs of cylinders in square and hexagonal arrays; see Figure 3.8 for the configurations. For bidisperse packs the relevant parameter is the diameter ratio $D_R = D_1/D_2$, where $D_1$ and $D_2$ are the diameters of the small and large cylinders, respectively. The length scale is set so that the average diameter is 1.0.

To evaluate the accuracy of the Ergun (1.5) and Forchheimer (1.6) equations for predicting the permeability of the flow, the authors plotted the appropriate friction factors as a function of Reynolds number [11]. The authors also proposed a modified Forchheimer equation, defined as

$$\frac{\Delta p}{L} = f_{\sqrt{K}} \frac{\rho \langle u_s \rangle^2}{\sqrt{K}} \frac{1-\sigma}{\sigma}, \qquad Re_{\sqrt{K}} = \frac{\rho \sqrt{K} \langle u_s \rangle}{\mu} \frac{1-\sigma}{\sigma}, \qquad f_{\sqrt{K}} = \frac{1}{Re_{\sqrt{K}}} + F, \quad (3.6)$$

where $f_{\sqrt{K}}$ is the modified friction factor and $Re_{\sqrt{K}}$ the modified Reynolds number. Note that now the length for the friction factor is $\sqrt{K}$ instead of the fiber diameter $D$. This correlation was established on both mono- and bidisperse packs of the ordered hexagonal orientation at $\sigma$=0.3 to 0.4, and the square orientation at $\sigma$=0.3 to 0.6. The authors showed that Ergun's equation was unable to capture the behavior when the flow has a strong contracting/expanding element. And although the original Forchheimer equation (1.6) gave reasonable results, the modified Forchheimer equation (3.6) gave the best fit through the data with $F = 0.08$ over the Reynolds numbers investigated. In the results to be presented below, we compare selected results with those of [11] for code verification. We also take the opportunity to extend the results by taking values of $\sigma$ and $D_R$ not previously considered in [11].

Results from our solver are presented in Figures (3.9) to (3.13). The velocities are assumed to be periodic in both $x$- and $y$-directions, while the pressure in the $y$-direction is periodic. The flow is driven by applying a pressure drop between the inlet and outlet as a Dirichlet

boundary condition. The domain size and the distance between the cylinders are determined from the porosity and $D_R$. The flow is solved until it reaches steady state. The grid resolution used in this section is $dx = dy \sim [0.0065 - 0.01]$, depending on the value of the porosity. These resolutions are selected so that roughly a two times finer resolution yields differences of less that 1.0% (results not shown). Parameters of the flow are the porosity, $D_R$, and the pressure drop across the domain. Friction factors are computed and compared with those by the Ergun's equation (1.5) and the modified Forchheimer equation (3.6).

### 3.4.1 Array of monodisperse cylinders

We first show results for monodisperse cylinders ($D_R = 1$). Figure 3.9a plots the friction factor $f_D$ as a function of the particle Reynolds number $Re_p$ and for various values of the porosity $\sigma$. Also shown as the solid line is Ergun's equation (1.5). It is observed that at $\sigma = 0.5$ and higher, the friction factors fall along Ergun's equation in the range of $0 < Re_p < 1.0$. At $\sigma = 0.4$, however, the friction factors are significantly above Ergun's equation. This suggests that Ergun's equation is not a universal curve. The results are replotted in Figure 3.9b using the modified Reynolds number $Re_{\sqrt{K}}$ as proposed in [11]. The friction factor $f_{\sqrt{K}}$ from the modified Forchheimer equation (3.6) is plotted as a solid curve. In both configurations (square and hexagonal arrays) and at all porosities tested, the predictions of the modified Forchheimer equation are significantly more accurate than those by Ergun's equation, having 1.0% or less difference between the computed results and the modified Forchheimer equation.

### 3.4.2 Array of bidisperse cylinders

We next investigate the effect of the diameter ratio $D_R$ on the friction factor. Figure 3.10 plots the friction factor as a function of the Reynolds number at a porosity of $\sigma = 0.6$. Also plotted is the prediction by Ergun's equation (1.5) as a solid line. It is clearly seen that Ergun's equation does not predict the friction factors accurately, especially when $D_R$ is

small.

Figure 3.11 plots the modified friction factor $f_{\sqrt{K}}$ as a function of the modified Reynolds number $Re_{\sqrt{K}}$ for (a) the square array and (b) the hexagonal array of bidisperse cylinders. For the square array the porosities shown are $\sigma = 0.6$ (open symbols) and 0.7 (closed symbols). For the hexagonal array the porosities shown are $\sigma = 0.5$ (open symbols) and 0.7 (closed symbols); results for $\sigma = 0.6$ show similar trend and are not plotted. In the plots the modified Forchheimer equation (3.6) is shown as the solid curve. Similarly to the case of the monodisperse cylinders, the accuracy of the modified Forchheimer equation is significantly better than that of Ergun's equation (1.5). As previously noted, Papathanasiou *et al.* [11] established the modified Forchheimer equation (3.6) based on their numerical experiments in the porosity range of $\sigma = 0.3$ to 0.6 for square arrays and 0.3 to 0.4 for hexagonal arrays. Our results suggest that equation (3.6) is valid for a wider range of $\sigma$ and $D_R$.

The literature [11] suggests that the presence of strong contraction/expansion of the pressure fails the capillary flow assumption of the Ergun's equation, resulting in over- or under-prediction of the friction factors. Figure 3.12 shows contours of the pressure at $\sigma$=0.4 and 0.7 for monodisperse packs. In the narrow space between cylinders for the low porosity pack, a rapid drop in pressure is observed, whereas the pressure decreases more gradually for the high porosity pack. Similar results are shown for bidisperse packs, see Figure 3.13. These pressure profiles help explain the inaccurate prediction of Ergun's equation at low porosities.

## 3.5 Summary

Extensive validation and verification problems have been conducted and presented for the newly developed Navier-Stokes solver and the ghost cell immersed boundary method. Both the flow solver and the ghost cell method demonstrated the expected order of accuracy. A number of simulations were conducted to test the validity on flow with immersed bodies, which include flow past a single object and flow through square and hexagonal arrays of

cylinders. In all the cases tested, our results agreed excellently with those found in the literature. From these results we have concluded that the new solver has a performance required for our purpose.

## 3.6 Figures

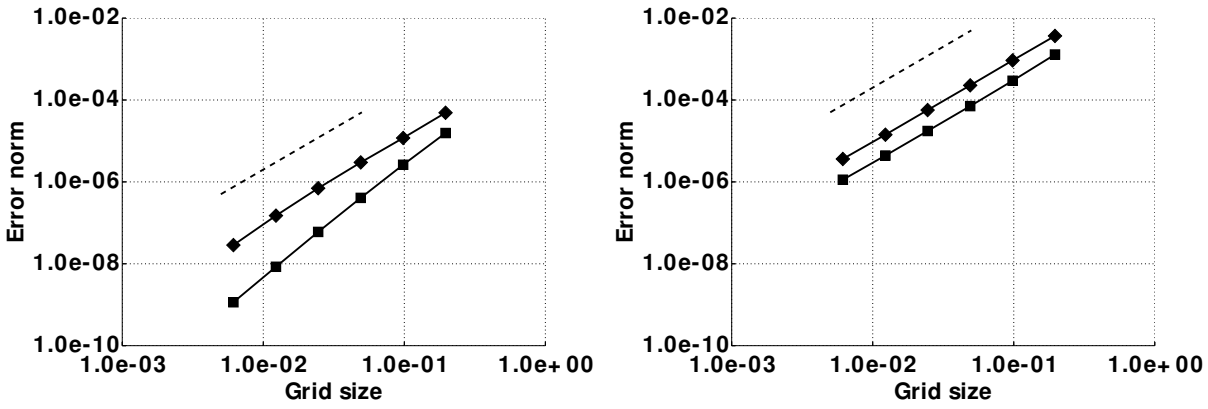


(a) Velocity

(b) Pressure

Figure 3.1: Error norms of the Taylor-Green vortex as a function of the grid size: $L_1$ norm (square); $L_{max}$ norm (diamond). Also shown is the 2nd-order convergence (dash).

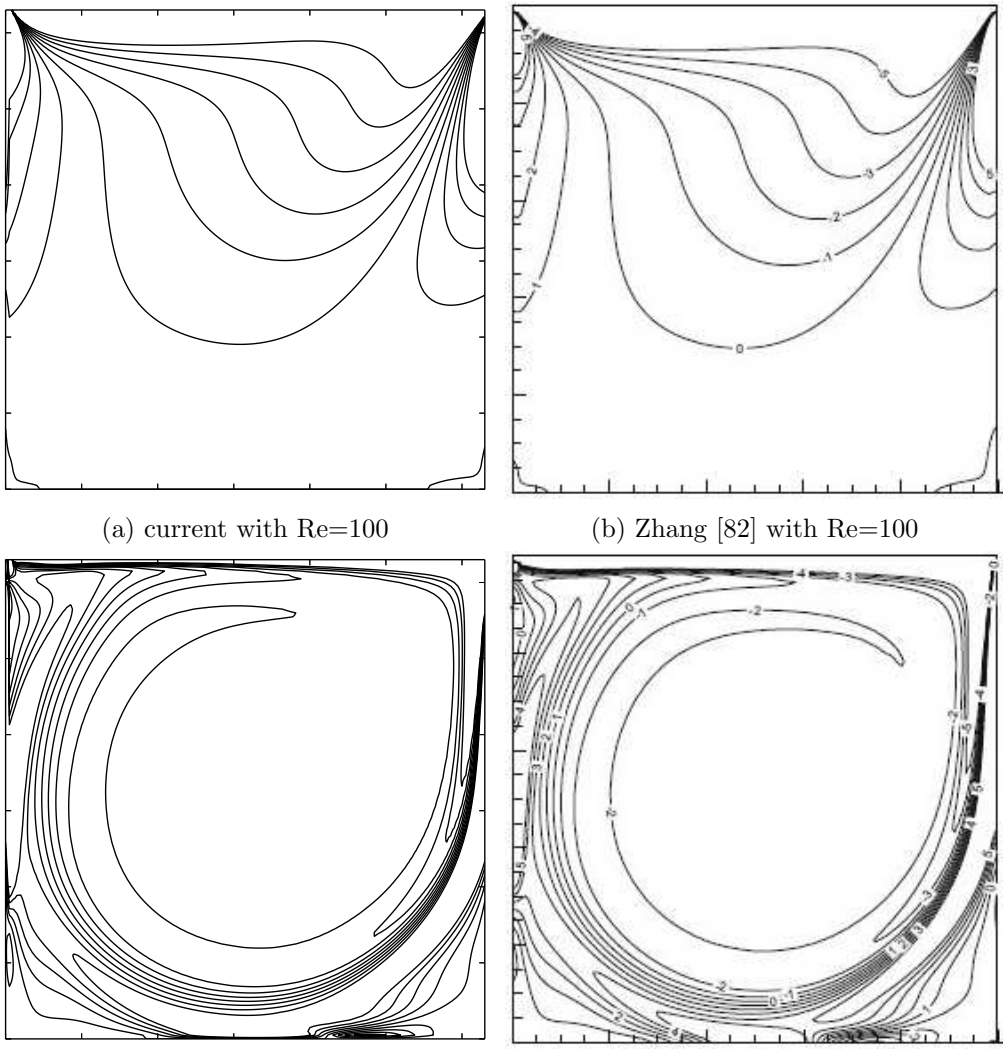

(a) current with Re=100

(b) Zhang [82] with Re=100

(c) current with Re=3200

(d) Zhang [82] with Re=3200

Figure 3.2: Vorticity contours for the driven cavity flow.

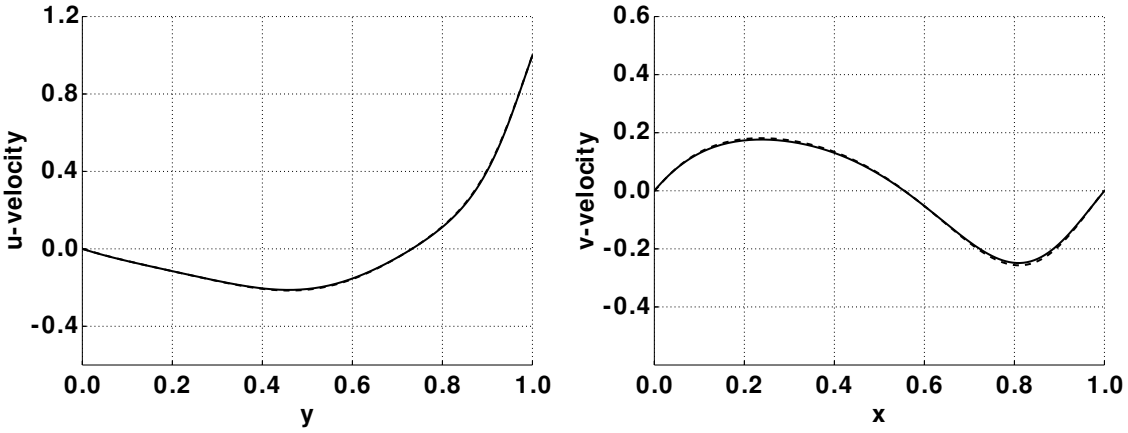


(a) $u$-velocity at $Re = 100$

(b) $v$-velocity at $Re = 100$

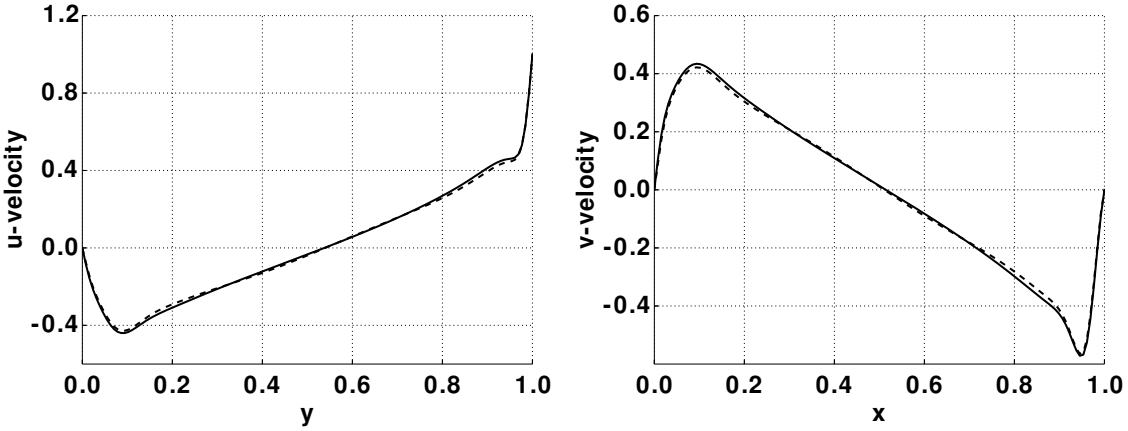


(c) $u$-velocity at $Re = 3200$

(d) $v$-velocity at $Re = 3200$

Figure 3.3: Velocity profiles for the driven cavity flow by current work (solid), and Zhang [82] (dashed).

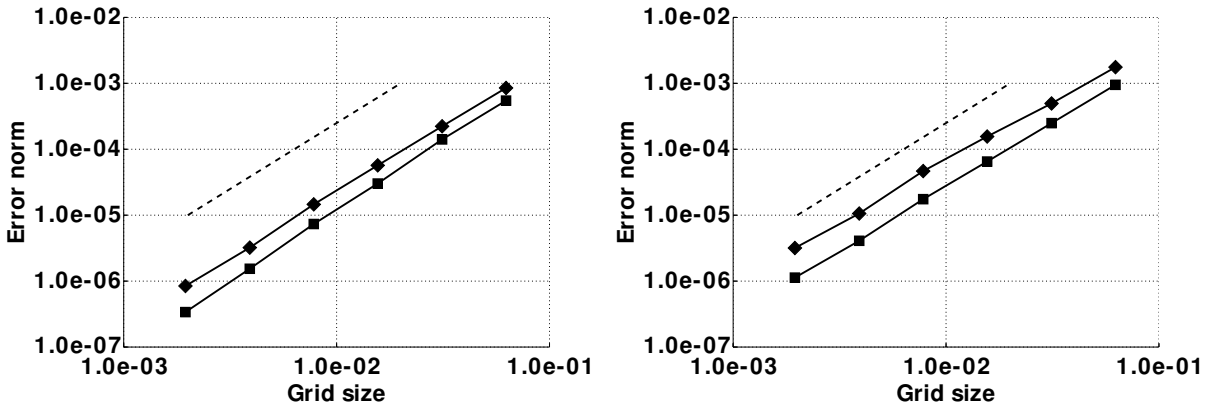


(a) Dirichlet condition

(b) von Neumann condition

Figure 3.4: Error norms of the ghost cell immersed boundary method as a function of the grid size: $L_1$ norm (square); $L_{max}$ norm (diamond). Also shown is the 2nd-order convergence (dash).

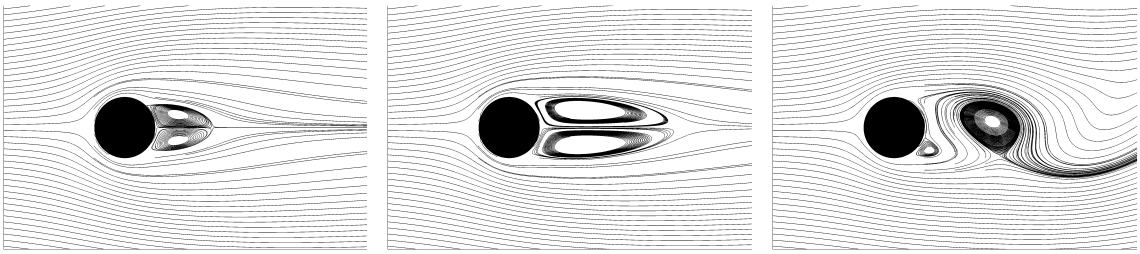

(a) Re=20 (b) Re=40 (c) Re=80

Figure 3.5: Streamlines for flow past a circular cylinder.

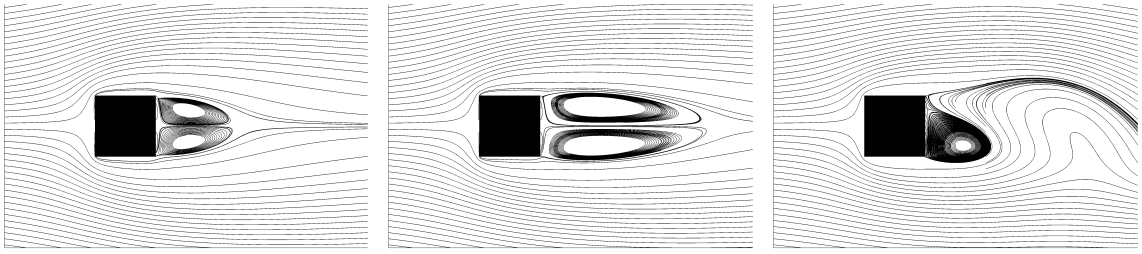

(a) Re=20 (b) Re=40 (c) Re=80

Figure 3.6: Streamlines for flow past a square rod.

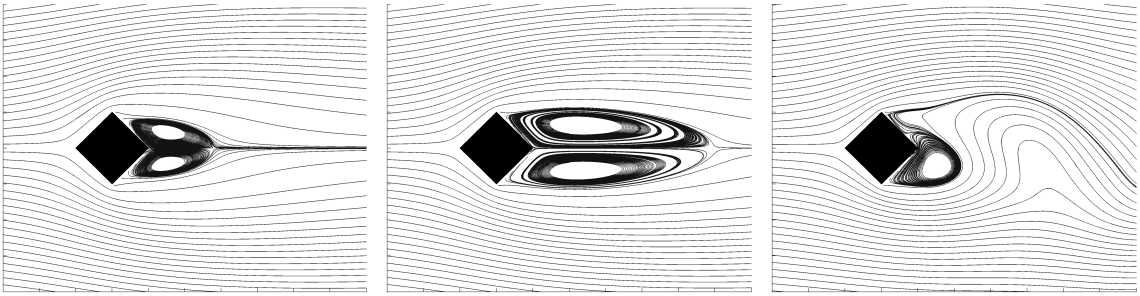

(a) Re=20 (b) Re=40 (c) Re=80

Figure 3.7: Streamlines for flow past a square rod at 45 degrees.

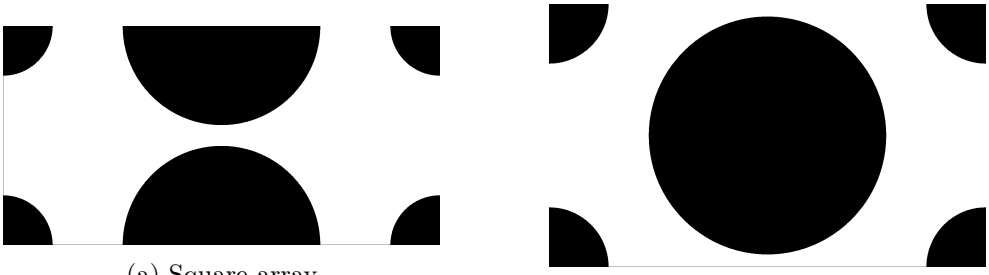

(a) Square array

(b) Hexagonal array

Figure 3.8: Schematics of square and hexagonal arrays of bidisperse cylinders with porosity $\sigma = 0.6$ and diameter ratio $D_R = 0.5$.

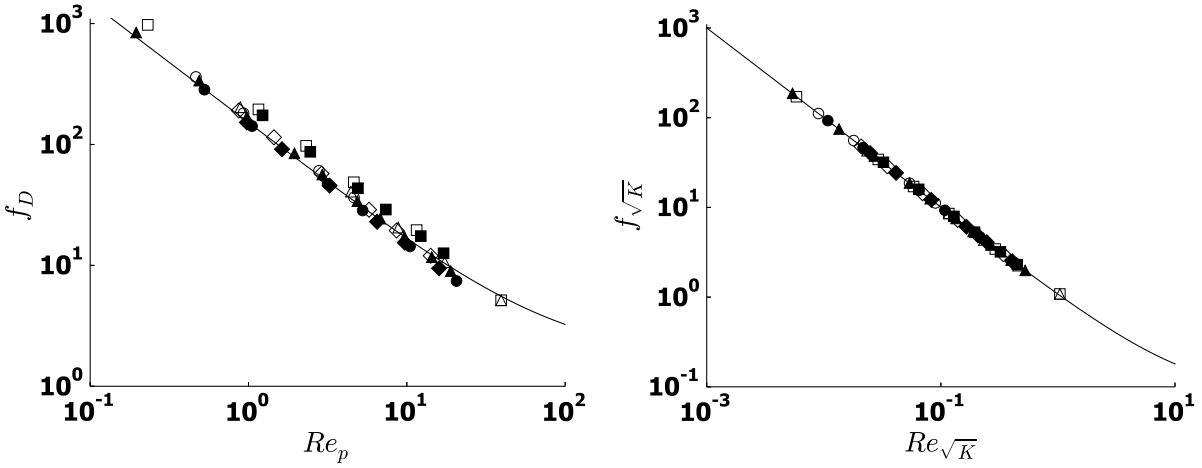


(a) Ergun's equation

(b) Forchheimer equations

Figure 3.9: (a) Plot of friction factor $f_D$ as a function of Reynolds number $Re_p$ (symbols) and Ergun's equation (1.5; solid line). (b) Plot of friction factor $f_{\sqrt{K}}$ as a function of modified Reynolds number $Re_{\sqrt{K}}$ (symbols) and modified Forchheimer equation (3.6; solid line) with $F = 0.08$. Here, porosity $\sigma = 0.4$ (square); 0.5 (triangle); 0.6 (diamond); 0.7 (circle). The filled symbols correspond to the square array and the open symbols correspond to the hexagonal array. Note the difference in scales between the two plots.

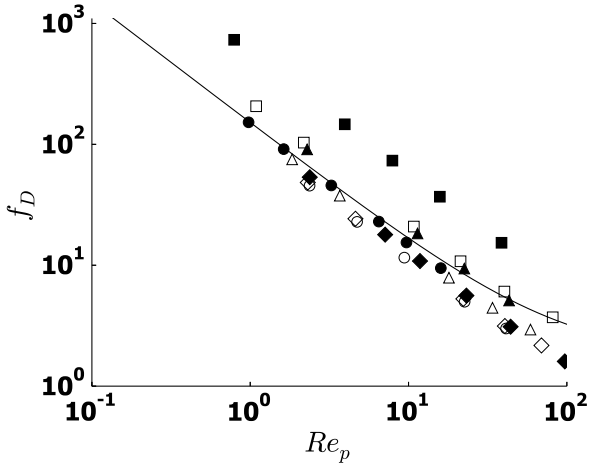


Figure 3.10: Plot of friction factor $f_D$ as a function of Reynolds number $Re_p$ for bidisperse cylinders and for $D_R = 0.5$ (square); 0.7 (triangle); 0.9 (diamond); 1.0 (circle). The filled symbols correspond to the square array and the open symbols correspond to the hexagonal array. Also shown is Ergun's equation (1.5; solid line). Here, porosity $\sigma$=0.6.

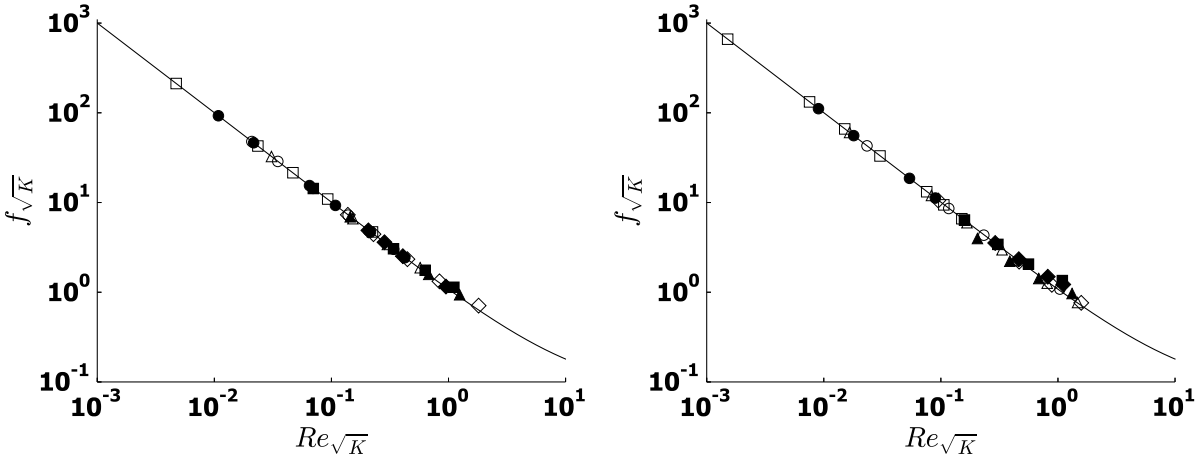


(a) Square array

(b) Hexagonal array

Figure 3.11: Plot of friction factor $f_{\sqrt{K}}$ as a function of modified Reynolds number $Re_{\sqrt{K}}$ for (a) square array and (b) hexagonal array of bidisperse cylinders. Here, $D_R = 0.5$ (square); 0.7 (triangle); 0.9 (diamond); 1.0 (circle). In (a) $\sigma = 0.6$ (open symbols) and 0.7 (closed symbols). In (b) $\sigma = 0.5$ (open symbols) and 0.7 (closed symbols); results for $\sigma = 0.6$ show similar trend and are not plotted. In each figure the modified Forchheimer equation (3.6) is shown as the solid curve with $F = 0.08$.

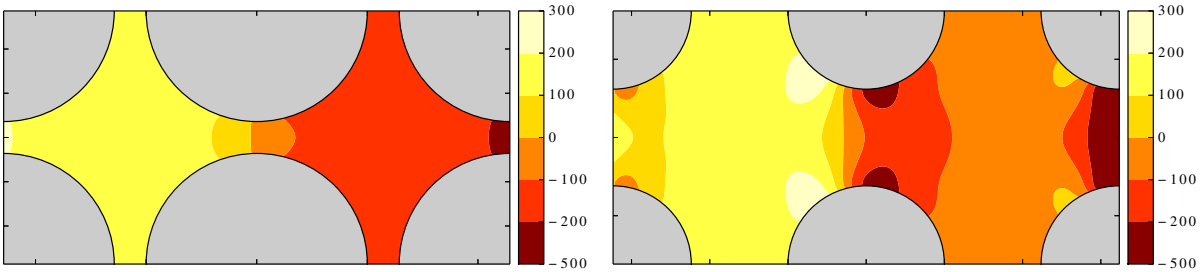


(a) $\sigma$=0.4 (b) $\sigma$=0.7

Figure 3.12: Pressure contours of flow past a square array of monodisperse cylinders.

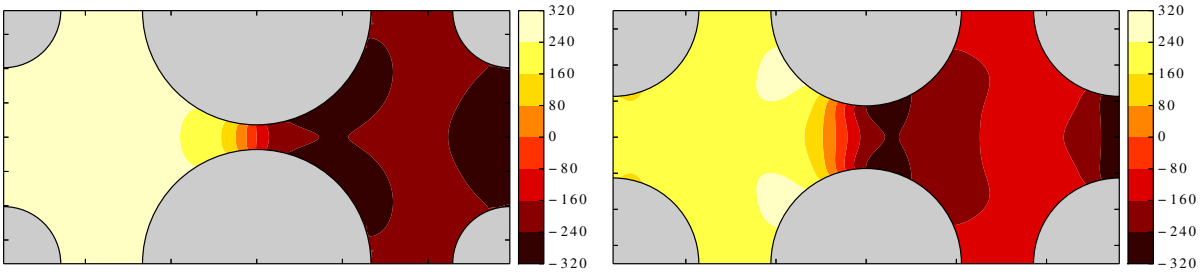


(a) $D_R$=0.5 (b) $D_R$=0.9

Figure 3.13: Pressure contours of flow past a square array of bidisperse cylinders at $\sigma$=0.6.

# Chapter 4

# Flow through random packs of particles

As discussed in Chapter 1, although flow through porous media has been studied for years, work on flow through random packs of polydisperse particles is still an area of active research. In this chapter we investigate flow through two-dimensional random packs of monodisperse, bidisperse and polydisperse circular cylinders, as well as monodisperse ellipses. Based on the results of flow solution, we establish a correlation between the macroscopic property of the packs and their corresponding microstructure. Finally, packs in the inertial flow regime are also analyzed by means of friction factors, in hopes of building better prediction equations that takes into account various pack geometries.

## 4.1 Problem outline

### 4.1.1 Formulation

We use our packing code to generate two-dimensional random packs of cylinders and ellipses at various porosities. We specify the minimum distance between any two particles to be 0.1 of the radius (or major axis) of the largest particle, necessary for two-dimensional packs to avoid complete blockage of the flow [39]. For each pack considered, we compute the permeability and the tortuosity. The permeability $K$ is scaled by the square of the particle

length $L_p$, and is determined using Darcy's law. That is, for a given pressure drop across the unit cell, the superficial (or average) velocity is first determined from the numerical simulation, and then the normalized permeability $K'$ is solved for using Darcy's law

$$K' \equiv \frac{K}{L_p^2} = -\frac{\langle u_s \rangle}{Re_p \Delta p / L}, \tag{4.1}$$

where $L_p$ is the particle length, $Re_p = \rho U_0 L_p / \mu$ the particle Reynolds number with fluid density $\rho$, velocity scale $U_0 = \langle u \rangle$, and viscosity $\mu$; $\langle u_s \rangle$ the non-dimensional superficial velocity; $\Delta p$ the non-dimensional pressure drop imposed across the unit cell in the transverse $x$-direction; and $L = L^*/L_p$ with $L^*$ the dimensional length of the pack domain in the flow direction. For monodisperse particles, $L_p = 4$ area/circumference, with

$$L_p = 2R = D \ \text{ for circle}, \qquad L_p = c \ \text{ for square}, \qquad L_p = 4\pi ab/A_L \ \text{ for ellipse}. \tag{4.2}$$

Here, $R$ is the radius of the circle; $c$ the length of one side of the square; and $a$ and $b$ the major and minor lengths of the ellipse, respectively, with $A_L$ the corresponding circumference. For polydisperse particles, we have

$$L_p = \sum_{i=1}^{M} n_i L_{p,i}. \tag{4.3}$$

Here, $M$ is the total number of unique particle sizes and $n_i$ is the number fraction for particle $i$ with length scale $L_{p,i}$. For example, for bidisperse cylinders with $M = 2$, denote the small cylinders with the subscript 1 and large cylinders with subscript 2, then $n_1 = N_1/N_p$ and $n_2 = N_2/N_p$ are the number fractions of the small and large cylinders, respectively, with $N_p$ the total number of cylinders.

The tortuosity $\tau$ is defined as the ratio of the length of the actual flow path of the fluid particles to the shortest path length in the direction of the mean flow; thus, $\tau \geq 1$. Physically, tortuosity shows the microscopic complexity of flow paths through a given microstructure.

In our numerical solver the tortuosity is calculated using [92, 93]

$$\tau = \frac{\sum_{i,j}\ u_{mag}(i,j)}{\sum_{i,j}\ |u(i,j)|}, \tag{4.4}$$

where $u(i,j)$ is the mean flow at the fluid grid points $(i,j)$, and $u_{mag}$ is the velocity magnitude

$$u_{mag}(i,j) = \sqrt{u(i,j)^2 + v(i,j)^2}, \tag{4.5}$$

Since a staggered grid is used, the velocity components are averaged to obtain values at the cell corners (where the pressure is located). Note that the fluid grid points $i,j$ refer to those points that lie inside the fluid domain and outside the immersed body domain.

### 4.1.2 Representative volume element

When two- and three-dimensional random packs are used in numerical simulations, it is necessary to carry out ensemble averaging to account for the effect of orientations, spacing, etc., on quantities of interest such as permeability. The ensemble average of the permeability and its standard deviation are defined as

$$\langle K \rangle = \frac{1}{N_r}\sum_{i=1}^{N_r} K_i, \qquad \sigma_{std}(K) = \sqrt{\frac{1}{N_r - 1}\sum_{i=1}^{N_r}(K_i - \langle K \rangle)^2}, \tag{4.6}$$

where $N_r$ is the ensemble size and $K_i$ is the permeability for the $i^{th}$ pack. The corresponding mean normalized permeability is therefore defined to be $K' = \langle K \rangle / L_p^2$. Similar definitions are used for the tortuosity. As pointed out in [39], when the representative volume element (RVE) is sufficiently large, or under the assumption of ergodicity, when a sufficiently large ensemble size is used for relatively smaller RVEs, the mean permeability should converge.

To determine the appropriate RVE for a finite ensemble size, we first fix the number of particles $N_p = 200$ and increase the ensemble size $N_r$ from one. Results are presented in Figure 4.1, where we plot the mean (solid) and the standard deviation (dash) of the

normalized permeability as a function of ensemble size $N_r$ and for porosities of $\sigma = 0.45$ and 0.7. Note that the mean and standard deviations vary little beyond $N_r = 10$.

We next fix $N_r = 20$ and vary the particle number $N_p$. Results are presented in Figure 4.2, where we plot the mean (symbol) and the standard deviation (error bars) of the normalized permeability as a function of particle number $N_p$ and for porosities of $\sigma = 0.45$ and 0.7. From the figure we see little variations in the mean and standard deviation beyond $N_p = 200$. We note that the convergence rate as a function of particle number is somewhat faster than that shown in Figure 4 of [39]. This is likely due to the fact that our unit cells use periodic boundaries, whereas in [39] the authors use unit cells with non-periodic boundaries and therefore have boundary effects.

In all of the results presented below we fix $N_p = 200$ and $N_r = 10$ for circular cylinders. These values are deemed sufficient for our purposes. The same tests were conducted for ellipses and the results will be presented in a later section. The grid resolution is $dx = dy \sim [0.02 - 0.035]$, depending on the value of the porosity.

## 4.2 Results for monodisperse cylinders

Results for random packs of monodisperse cylinders are shown in Figure 4.3, which plots the normalized permeability as a function of porosity, and the relevant data is given in Table 4.1. Recall that for monodisperse packs the length scale $L_p$ is the diameter $D$ of the cylinder. For comparison we also present results from [15, 39]. The results show excellent agreement between the current work and the literature.

As previously mentioned, a number of length scales can be defined in an attempt to relate macroscopic quantities, namely permeability, to some statistical descriptor of the underlying microstructure [37]-[42]. The most relevant scalings are based on nearest neighbor $\gamma_n$ and shortest Delaunay edges $\gamma_1^T$. The definition of the relevant length scales are given in Table 4.2. In the table, $\langle D_n \rangle$ is the mean distance for the $n$-th nearest neighbor; $D$ is the particle diameter; and $\langle e_1^T \rangle$ is the mean value of the shortest Delaunay edges, $\hat{R}$ represents the sum

| Porosity | Current | Sangani and Yao[15] | Chen and Papathanasiou[39] |
|---|---|---|---|
| 0.45 | 1.13E-03 | - | - |
| 0.50 | 2.01E-03 | 2.35E-03 | 2.1E-03 |
| 0.60 | 5.94E-03 | - | - |
| 0.70 | 2.34E-02 | 2.55E-02 | 2.28E-02 |
| 0.90 | - | 4.18E-01 | 4.1E-01 |

Table 4.1: Results for mean normalized permeability $K' = \langle K \rangle / L_p^2$ as a function of porosity $\sigma$.

of the two radii that make up the shortest edge or nearest neighbor, and $L_p$ is the length scale given by equation (4.3). For ellipses, $\hat{R}$ is a portion of the length inside the particles that make up the shortest edge or nearest neighbor. $\langle\rangle$ represents the mean of the shortest values for each particle neighbor or Delaunay triangle. Thus, the difference between $e_1^T$ and $\hat{R}$ represents the interparticle spacing. In addition, $\gamma_n$ is the mean of the $n$-th shortest interparticle spacing for each particle, and $\gamma_1^T$ is the mean of the shortest spacing for each Delaunay triangle. Figure 4.4 shows particles and the corresponding normalized shortest Delaunay edges for packs of bidisperse cylinders and monodisperse ellipses.

| | |
|---|---|
| Nearest neighbor | $\gamma_n = \langle D_n - \hat{R} \rangle / L_p$ |
| Delaunay edge | $\gamma_1^T = \langle e_1^T - \hat{R} \rangle / L_p$ |

Table 4.2: Relevant length scales [41, 42].

By examining random packs of monodisperse cylinders, [41, 42] showed that $\gamma_2 \approx \gamma_1^T$ and that the permeability scales with respect to $\gamma_2$ with scaling

$$\frac{\langle K \rangle}{L_p^2} = C_1 \, \gamma_2^{2.5} \left(1 - C_2 \, e^{-C_3 \, \gamma_2}\right), \tag{4.7}$$

with $C_1 = 0.2$, $C_2 = 0.5$, and $C_3 = 3$. The exponent of 2.5 in equation (4.7) is derived from lubrication theory for square and hexagonal arrays of monodisperse and bidisperse cylinders [94, 95]. The exponential correction factor accounts for disordered arrays.

We perform a similar analysis to that of [41, 42] for our packs. The length scales $\gamma_1$, $\gamma_2$,

and $\gamma_1^T$ are plotted as a function of porosity in Figure 4.5(a), and the values compare well with Figure 8 of [41]. Figure 4.5(b) plots the mean normalized permeability as a function of the scaling $\gamma_1^T$. A least squares fit through the data leads to the scaling

$$K'_{fit} \equiv \frac{\langle K \rangle}{L_p^2} = \hat{C} \left(\gamma_1^T\right)^{2.5+\nu}, \qquad \hat{C} = 0.3354,\ \nu = 0.5426, \tag{4.8}$$

which gives a slightly better fit than equation (4.7) especially at the higher values of porosity (plot not shown). Our results confirm the findings of [41, 42], in that there exists a universal curve (either equation (4.7) or the slightly better fit given by (4.8)) relating the permeability to the length scale $\gamma_1^T$ of the underlying microstructure. It should be remembered that the fit has only been shown to be valid for two-dimensional random packs of monodisperse cylinders. It has yet to be determined if the fit is also valid for polydisperse particles, for non-spherical particles or in three-dimensional flows. Contours of the velocity magnitude and pressure, and the corresponding streamlines, are shown in Figure 4.6 for $\sigma = 0.7$. Also shown with the velocity magnitude in white lines are $\gamma_1$ and $\gamma_1^T$. From the velocity magnitude, we observe that the flow paths are mostly through the regions without lines, indicating that the flow tends to go through the large spacing between particles. Note that, however, $\gamma_1^T$ has more lines compared to $\gamma_1$, and some of the lines are across the flow paths.

## 4.3 Results for bidisperse cylinders

### 4.3.1 Permeability and flow field

We next compute the permeability for random packs of bidisperse cylinders as a function of diameter ratio $D_R = R_1/R_2$, large-to-total particle ratio $\mathcal{N} \equiv N_2/N_p$, and porosity $\sigma$. Recall that for monodisperse packs the length scale $L_p = D$ is the particle diameter while for bidisperse packs the length scale is given by equation (4.3), i.e., $L_p = 2((1-\mathcal{N})R_1 + \mathcal{N}R_2)$, where $R_1$ is the radius of the small particle and $R_2$ is the radius of the large particle. In all of these calculations we keep the number of cylinders fixed with $N_p = 200$ and vary the

number of large cylinders $N_2$. The number of small cylinders is then $N_1 = N_p - N_2$.

Tests were first conducted keeping $\mathcal{N} = 0.5$ fixed and varying $D_R = 0.3$, 0.5 and 0.7. Figure 4.7(a) shows the various lengths $\gamma$ as a function of porosity at $D_R = 0.3$ and 0.7. As shown for the monodisperse case, $\gamma_2$ and $\gamma_1^T$ are close, and the diameter ratios cause significant difference in all $\gamma$. Figure 4.7(b) is a plot of the normalized permeability as a function of various $\gamma$. Again, as observed in monodisperse packs, $\gamma_1^T$ shows the best agreement with the prediction given by Eq.4.8. Thus, it is confirmed that $\gamma_1^T$ is appropriate for the length scale for the bidisperse cases.

The mean normalized permeability as a function of porosity is plotted in Figure 4.8(a). It can be seen that the permeability increases as the diameter ratio decreases or as the porosity increases. From the figure it is tempting to see if a scaling exists that collapses the data onto a single curve. And so we show in Figure 4.8(b) the results with the following scaling,

$$K'_s = s_1(D_R)\, K', \qquad \text{with } s_1 = a_0 + a_1\, D_R + a_2\, D_R^2, \tag{4.9}$$

where $K'_s$ is the scaled normalized permeability, $s_1 = s_1(D_R)$ is a quadratic function in $D_R$, and a least squares fit results in $a_0 = 0.282$, $a_1 = 1.302$, and $a_2 = -0.588$. With this scaling the data essentially collapses onto the monodisperse results $D_R = 1.0$, with differences of less than $\pm 10\%$. The corresponding length scale $\gamma_1^T$ as a function of porosity is plotted in Figure 4.9(a) for various values of $D_R$. From the figure we see that the value of $\gamma_1^T$ increases as the diameter ratio decreases or as the porosity increases. Again it is tempting to determine a scaling that will collapse the data onto the monodisperse case, which is given by

$$(\gamma_1^T)' = t_1(D_R)\, \gamma_1^T, \qquad \text{with } t_1 = b_0 + b_1\, D_R + b_2\, D_R^2, \tag{4.10}$$

with $b_0 = 0.463$, $b_1 = 1.083$, and $b_2 = -0.550$ determined using a least squares fit. Figure 4.9(b) plots the scaled results. Finally, we plot in Figure 4.10(a) the permeability as a function of $\gamma_1^T$ for various values of $D_R$. The corresponding plot for the scaled permeability $K'_s$ as a function of the scaled mean shortest Delaunay edge $(\gamma_1^T)'$, shown in Figure 4.10(b),

shows that the data essentially collapses onto the monodisperse case, and that the universal fit given by equation (4.8) remains valid.

The next tests compute the permeability as a function of the large-to-total particle ratio, $\mathcal{N}$. Note that $D_R = 1$ or $\mathcal{N} = 0, 1$ corresponds to the monodisperse case. Figure 4.11a is a plot of the various lengths $\gamma$ as a function of porosity at $\mathcal{N} = 0.25$ and 0.75 with $D_R = 0.5$ fixed. Similar to the fixed $\mathcal{N}$ cases, $\gamma_2$ and $\gamma_1^T$ are close compared to $\gamma_1$. The influence of $\mathcal{N}$ is slightly less than that of the diameter ratios. Figure 4.11b shows the normalized permeability as a function of various $\gamma$ at $\mathcal{N} = 0.25$ and 0.75 with $D_R = 0.5$ fixed. It is again observed that good agreement with the prediction by equation 4.8 is found with $\gamma_1^T$. This confirms that $\gamma_1^T$ should be used as a length scale for the bidisperse cases with various $\mathcal{N}$.

Figure 4.12(a) plots the permeability as a function of $\mathcal{N}$ and for various values of the diameter ratio $D_R$ and porosity $\sigma$. From the figure we see that a maximum in the permeability exists at approximately $\mathcal{N} = 0.25$. Again, it is tempting to find a fit that collapses the data onto a single curve for each value of the porosity. The figure suggests the following functional form,

$$K'_s = s_2(D_R, \mathcal{N})\, K'. \tag{4.11}$$

The function $s_2$ should have the following properties: (i) $s_2 = 1$ at $\mathcal{N} = 1$ and at $\mathcal{N} = 0$, and (ii) $s_2$ has a maximum at $\mathcal{N} = 0.25$. And so we choose the functional form

$$s_2 = 1 + (c_0 + c_1\, D_R + c_2\, D_R^2)\mathcal{N}(1 - \mathcal{N}) \exp(-c\mathcal{N}). \tag{4.12}$$

The expression $\mathcal{N}(1 - \mathcal{N})$ is a quadratic function that is zero at $\mathcal{N} = 0,\ 1$ and thus satisfies (i); the constant $c = 8/3$ in the exponential term is chosen so that the location of the maximum shifts to $\mathcal{N} = 0.25$ and thus satisfies (ii). Setting $s_2(D_R, 1/2) = s_1(D_R)$ yields the coefficients $c_0 = -10.90$, $c_1 = 19.78$, and $c_2 = -8.923$. The scaled permeability is plotted in Figure 4.12(b), and shows that the data collapses to the monodisperse case for each value

of the porosity. We make no claim that the strategy just outlined is unique. For example, using a least squares fit to define the coefficients rather than equating $s_2(D_R, 1/2) = s_1(D_R)$ yields the coefficients $c_0 = -11.73$, $c_1 = 24.24$, and $c_2 = -12.88$. The resulting plots (not shown) gives a slightly better fit at $\sigma = 0.7$. Absent a rigorous theory to guide in the fitting process, our only purpose here is to show that a scaling does exist.

Figure 4.13(a) plots $\gamma_1^T$ as a function of $\mathcal{N}$ and for various values of $D_R$ and $\sigma$. Similar to the plot of the permeability, a maximum exists at $\mathcal{N} = 0.25$. To collapse the data and each value of $\sigma$, we use the scaling

$$(\gamma_1^T)' = t_2(D_R, \mathcal{N})\, \gamma_1^T, \tag{4.13}$$

where

$$t_2 = 1 + (d_0 + d_1\, D_R + d_2\, D_R^2)\mathcal{N}(1 - \mathcal{N}) \exp(-c\mathcal{N}). \tag{4.14}$$

Setting $t_2(D_R, 1/2) = t_1(D_R)$ yields the coefficients $d_0 = -8.15$, $d_1 = 16.43$, and $d_2 = -8.35$. Figure 4.13(b) plots $(\gamma_1^T)'$ as a function of $\mathcal{N}$. Note that although the fit to the monodisperse results is reasonably good, there is some small scatter in the data.

Figure 4.14(a) plots the mean normalized permeability as a function of $\gamma_1^T$ and for various values of $\mathcal{N}$, $\sigma$, and $D_R$. The corresponding plot for the scaled permeability $K_s'$ as a function of the scaled mean shortest Delaunay edge $\left(\gamma_1^T\right)'$ in Figure 4.14(b) shows that the data essentially collapses onto the monodisperse case, and that the universal fit given by equation (4.8) remains valid.

Finally, we show contour plots of velocity magnitude in Figure 4.15 for $\sigma = 0.6$, $D_R = 0.5$, and for two values of $\mathcal{N}$. Also shown as white line segments are (a,c) the first nearest neighbors and (b,d) the shortest Delaunay edge for each Delaunay triangle. The corresponding streamlines and contours of pressure are plotted in Figures 4.16 and 4.17, respectively. As observed on the monodisperse cylinders, the flow paths are found where the interparticle spacing is large.

### 4.3.2 Carman-Kozeny equation

As discussed in [37], the Carman-Kozeny (CK) equation is widely used in the porous media literature to relate the permeability to the porosity of the microstructure via

$$K' \equiv \frac{\langle K \rangle}{L_p^2} = \frac{1}{\psi_{CK}} \frac{\sigma^3}{(1-\sigma)^2}, \tag{4.15}$$

where the Carman-Kozeny factor, $\psi_{CK}$, is related to the tortuosity via

$$\psi_{CK} = \Phi \tau^2. \tag{4.16}$$

Here, $\Phi$ represents the effect of particle shape, and can be seen as a fitting parameter. For a given simulation, once the mean normalized permeability and tortuosity parameters have been computed, the Carman-Kozeny factor can be determined from equation (4.15), and then the shape factor can be found using equation (4.16). The Carman-Kozeny factor is plotted in Figure 4.18(a) as a function of porosity and for various values of the diameter ratio $D_R$ and for $\mathcal{N} = 0.5$. It can be seen that the Carman-Kozeny factor decreases as the porosity increases for a fixed value of $D_R$, or for a fixed value of the porosity as $D_R$ decreases.

We note that in classical literature, the Carman-Kozeny factor is taken to be a constant. As pointed out in [39, 37], the Carman-Kozeny factor is not constant but depends on the details of the microstructure. Indeed, our results show that the factor depends not only on the porosity but also the diameter ratio. However, a scaled Carman-Kozeny factor can be defined using the scaled permeability $K'_s$ defined in equation (4.9), as follows

$$\psi'_{CK} = \frac{\sigma^3}{(1-\sigma)^2} \frac{1}{K'_s}. \tag{4.17}$$

The scaled Carman-Kozeny factor is plotted in Figure 4.18(b) and shows that the data collapses onto a single curve, although there is slightly more scatter than the corresponding permeability plot shown in Figure 4.8(b).

## 4.4 Results for polydisperse cylinders

### 4.4.1 Pack properties

In this section we simulate flow through random packs of polydisperse cylinders. The particle size distribution is generated using a Gaussian distribution, defined by

$$f(D_i) = \frac{1}{D_\sigma\sqrt{2\pi}} e^{-\frac{(D_i-\bar{D})^2}{2D_\sigma^2}}, \tag{4.18}$$

where $f(D_i)$ is the probability with standard deviation $D_\sigma$ and mean $\bar{D}$. The mean diameter is scaled such that $\bar{D} = 1.0$ and we use nine diameters; these are chosen to be 1.0, $1.0\pm0.5D_\sigma$, $1.0 \pm 1.0D_\sigma$, $1.0 \pm 1.5D_\sigma$, and $1.0 \pm 2.0D_\sigma$. To investigate the effect of polydispersity, we take $D_\sigma = 0$, 0.125, 0.25, and 0.375. Note that $D_\sigma = 0.0$ indicates a monodisperse pack. For each value of $D_\sigma$, packs with porosity of $\sigma = 0.45$, 0.60, and 0.70 are generated. The distributions used in this study are plotted in Figure 4.19(a). The corresponding diameters and number of cylinders for each value of $D_\sigma$ are tabulated in Table 4.3. A representative random pack is shown in Figure 4.19(b) for $D_\sigma = 0.25$ and porosity $\sigma = 0.45$.

| Diameter | | | No. of cylinders |
|---|---|---|---|
| $D_\sigma = 0.375$ | $D_\sigma = 0.25$ | $D_\sigma = 0.125$ | |
| 0.25 | 0.50 | 0.75 | 5 |
| 0.44 | 0.63 | 0.81 | 13 |
| 0.63 | 0.75 | 0.88 | 24 |
| 0.81 | 0.88 | 0.94 | 36 |
| 1.00 | 1.00 | 1.00 | 40 |
| 1.19 | 1.13 | 1.06 | 36 |
| 1.38 | 1.25 | 1.13 | 24 |
| 1.56 | 1.38 | 1.19 | 13 |
| 1.75 | 1.50 | 1.25 | 5 |

Table 4.3: Particle size distributions and number of cylinders for polydisperse packs for various values of $D_\sigma$.

### 4.4.2 Results and scaling

Figure 4.20(a) is a plot of the various relevant length scales $\gamma$ as a function of porosity and for $D_\sigma = 0.0$ and 0.375. Note that $\gamma_2$ and $\gamma_1^T$ are relatively close compared to $\gamma_1$. In Figure 4.20(b) the mean normalized permeability as a function of various $\gamma$ is shown with the fit given by equation 4.8. The best agreement with the fit is seen with $\gamma_1^T$, as observed for the mono- and bidisperse packs.

The mean normalized permeabilities as a function of porosity and for various values of $D_\sigma$ are plotted in Figure 4.21(a). The figure shows that the permeability increases as the porosity and polydispersity increase. From the figure it is tempting to see if a scaling exists that collapses the data onto a single curve. And so we show in Figure 4.21(b) the results with the following scaling,

$$K_s' = s_3(D_\sigma)\frac{\langle K\rangle}{L_p^2}, \qquad \text{with } s_3 = a_0 + a_1 D_\sigma + a_2 D_\sigma^2, \tag{4.19}$$

where $K_s'$ is the scaled normalized permeability and $s_1 = s_1(D_\sigma)$ is a quadratic function in $D_\sigma$. A least squares fit results in the values $(a_0, a_1, a_2) = (1.016, -0.489, -0.595)$. With this scaling the data essentially collapses onto the monodisperse results $D_\sigma = 0.0$.

From the figure we see that the value of $\gamma_1^T$ increases as the porosity and polydispersity increase. Again it is tempting to determine a scaling that will collapse the data onto the monodisperse case, which is found to be

$$(\gamma_1^T)_s' = t_3(D_\sigma)\gamma_1^T, \qquad \text{with } t_3 = b_0 + b_1 D_\sigma + b_2 D_\sigma^2, \tag{4.20}$$

with $(b_0, b_1, b_2) = (1.006, -0.144, -0.824)$. Figure 4.22(b) plots the scaled results.

Finally, the mean normalized permeabilities as a function of $\gamma_1^T$ and for various values of $D_\sigma$ and $\sigma$ are plotted in Figure 4.23(a), and the scaled values in Figure 4.23(b). In each figure the prediction given by (4.8) is plotted as the solid line. It can be seen from Figure 4.23(b) that the scaled permeability is well predicted by (4.8).

Plot of mean normalized permeability $K' = \langle K \rangle / L_p^2$ as a function of mean shortest Delaunay edge $\gamma_1^T$ and for various values of porosity $\sigma$ and diameter variation $D_\sigma$. In (b) the permeability and $\gamma_1^T$ are scaled. Also shown in (b) is the fit given by equation (4.8) (solid), with $\pm 20\%$ variations (dash). Here, $D_\sigma = 0.0$ (circle); 0.125 (square); 0.25 (triangle); 0.375 (diamond). Values of $\sigma$ are marked.

### 4.4.3 Statistical analysis and rare events

It is well known that when the number of random samples is sufficiently large, there may appear a case when the result is drastically off of the mean. Such a case is called a rare event, usually defined when a value is larger or smaller than the mean plus/minus three times the standard deviation.

To investigate if such events exist for packs of polydisperse cylinders, the permeability of 500 samples with $\sigma = 0.45$ and $D_\sigma = 0.25$ are computed. The results are plotted along with the mean and standard deviations in Figure 4.24(a) for the normalized permeability and Figure 4.24(b) for $\gamma_1^T$. From the figure we see that the permeability at six points are found to be rare events, and six points as well for $\gamma_1^T$; however, these rare events occur for different packs for the permeability and $\gamma_1^T$. This suggests that rare events can exist, and that rare events in the permeability do not necessarily correspond to those of $\gamma_1^T$. We comment that a grid resolution study was carried out for the rare events to ensure that the value of the permeability did not change with resolution; we find that doubling the grid in both directions only changed the value of the permeability by less than 2%.

To analyze the microstructural behavior of rare events, pressure contours with permeability close to the mean ($K'$=1.41e-3) and close to a rare event ($K'$=0.81e-3) are shown in Figure 4.25. The mean shortest Delaunay edges are also plotted as white line segments. Note that the pressure region (yellow) is narrower in the flow direction when the normalized permeability is close to the mean, compared to that of the rare event. This is probably due to the fact that the cylinders are more homogeneously packed when the permeability is close to the mean, whereas for the rare event the pack has a large voidage region at roughly

$(x, y) = (-3.0, 6.0)$ and a dense region at roughly $(x, y) = (7.5, -8.0)$.

The pressure distribution is also analyzed by plotting the pressure profile along the flow direction. The pressure in the fluid region is averaged over $y$-axis as

$$p(x) = \frac{1}{L_{fluid}(x)} \int_{ymin}^{ymax} p_{fluid}(x, y) dy \tag{4.21}$$

where $L_{fluid}(x)$ is the vertical length of the fluid region. $p(x)$ is plotted for packs with the permeability close to the mean ($K'$=1.41e-3), a rare event with the permeability lower than $-3\sigma$ ($K'$=0.81e-3) and higher than $+3\sigma$ ($K'$=1.83e-3) in Figure 4.27. It shows that the rare event with the low permeability has some regions where the pressure drops rapidly as well as where the pressure remains relatively flat. This characteristic agrees with an observation of the pressure contours described above. The pressure profile with the mean permeability, on the other hand, decreases more uniformly. However, the rare event with the high permeability case does not show a distinct difference in pressure profile from the mean permeability profile.

The corresponding contour plot of the velocity magnitude (not shown) for the rare event shows a peak magnitude of roughly 0.07 in the dense region; this value is about twice that of the case where the permeability is close to the mean. The corresponding streamlines are plotted in Figure 4.26.

Finally, to examine the statistical nature of the permeability, we show in Figure 4.28(a) the probability using a normal distribution and in Figure 4.28(b) using a Weibull distribution. For the normal distribution, the mean and standard deviations are found to be $\mu$=1.42e-3 and $\sigma_{std}$=0.12e-3, respectively; for the Weibull distribution the scale and shape parameters are found to be $a = 0.00147$ and $b = 12.21$, respectively. From the figures we see that although the data is well represented by a normal distribution, with the data in the tails falling outside the fit, the fit to the Weibull distribution is better, especially in the tails. Figure 4.29 compares the normal distribution (solid) to the Weibull distribution (dash). Note that since the value of $b > 3.7$, the Weibull distribution is negatively skewed (left tail).

The skewness in the data can be traced back to the fact that there are no values of the permeability greater then $\mu + 3\sigma_{std}$, but there are values below $\mu - 3\sigma_{std}$. Therefore, it might be better to describe the data using a Weibull distribution rather than assuming a normal distribution.

## 4.5 Results for ellipses

In this section we investigate the effect of particle shape on permeability by examining random packs of ellipses. The aspect ratio of an ellipse is defined by $AR = a/b$, where $a$ is the major and $b$ the minor lengths of the ellipse. Similar to [37, 38, 39], a minimal distance is required in two-dimensions to avoid complete blockage, and we therefore set the minimum inter-fiber distance $\delta = 0.1a$. Figure (4.30) show periodic packs with different aspect ratios $AR$ and porosity $\sigma$, with $N_p = 100$ particles.

### 4.5.1 Regular array

We first consider the flow past a single ellipse recently analyzed in [37]. With periodic boundaries, this configuration emulates the flow through a pack of ellipses in a regular square array. Two orientations are examined. An ellipse with angle $0^o$ implies that the major axis is aligned with the flow (i.e., along the $x$-axis), while an angle of $90^o$ implies that the major axis is aligned vertical to the flow (i.e., along the $y$-axis); see Figure (5b) of [37] for a sketch of the orientation. The normalized permeability and tortuosity for angles $0^o$ (filled triangle) and $90^o$ (filled square) are plotted in Figure 4.31 as a function of porosity $\sigma$ and for an aspect ratio of $AR = 2.0$. Also plotted as corresponding open symbols are results taken from Figures (5b) and (10a) of [37], showing an excellent agreement with our results. In addition, we show in Figure 4.31 results for a random pack of 100 ellipses with aspect ratio $AR = 2.0$ (filled circle). From the figure we see that the permeability corresponding to the random pack is bounded above and below by the permeability of a single ellipse in a square array at an orientation of $0^o$ and $90^o$, respectively. The tortuosity, on the other hand,

lies above the single ellipse cases. This is to be expected since a particle path through a random pack is longer than a particle path around a single ellipse. In the results presented here we use $512 \times 512$ grid points in the $x, y$-directions, respectively. Some cases required a finer mesh. Grid independence was spot checked by increasing the number of grid points for a number of different cases.

### 4.5.2 Random packs

To determine the appropriate RVE for a finite ensemble size for ellipses, we take $N_r = 15$ and vary the particle number $20 \leq N_p \leq 140$ for a fixed porosity $\sigma = 0.7$ and aspect ratio $AR = 2.5$. Results are present in Figure 4.32, where we plot the mean (symbol) and the standard deviation (error bars) of the normalized permeability and tortuosity as a function $N_p$. We see little variation in the means beyond 80 ellipses. As observed for packs of circular cylinders, the convergence rates as a function of particle number are somewhat faster than that shown in Figure (4) of [39]. In all of the results presented below we fix $N_p = 100$ and $N_r = 10$. These values were deemed sufficient for our purposes.

### 4.5.3 Permeability and length scales

Figure 4.33 plots the normalized permeability and tortuosity as a function of porosity and aspect ratio. Interestingly, when the permeability is scaled by the square of the particle length $L_p^2$, so that different aspect ratios have different values of $L_p$, the results are roughly linear on a log plot. This suggests that the aspect ratio has little effect on the normalized permeability, and that the permeability using random packs of ellipses can well be approximated by random packs of disks. On the other hand, there is a strong effect of aspect ratio on the tortuosity.

Figure 4.34(a) plots the length scales $\gamma$ as a function of porosity at $AR = 1.5$ and 3.0. The aspect ratio has a relatively strong effect on the length scales. $\gamma_2$ and $\gamma_1^T$ are nearly identical compared to circular cylinder cases. Figure 4.34(b) is a plot of the normalized permeability as a function of various $\gamma$ at the same aspect ratios. Also shown is the prediction given

by equation (4.8) as a solid line. Although there is a slight deviation observed, it is again confirmed that the best fit is obtained with $\gamma_1^T$.

Figure 4.35(a) plots $\gamma_1^T$ as a function of porosity and for different aspect ratios. Unlike permeability, $\gamma_1^T$ shows significant variations due to aspect ratio. Again, a scaling was attempted to collapse the data onto $AR = 1.0$ (i.e. monodisperse circular cylinders), and is given by

$$(\gamma_1^T)'_s = t_4(AR)\gamma_1^T, \qquad t_4(AR) = h_0 + h_1 AR + h_2 AR^2, \tag{4.22}$$

with $(h_0, h_1, h_2) = (0.091, -0.566, 1.474)$. Figure 4.35(b) plots the scaled results and shows the data collapses onto a single curve, except at the higher values of the porosities where some variations are still observed.

The normalized permeability is plotted as a function of $\gamma_1^T$ in Figure 4.36(a). Introducing the scaling

$$K'_s = s_4(AR)\frac{\langle K \rangle}{L_p^2}, \qquad s_4(AR) = g_0 + g_1 AR + g_2 AR^2, \tag{4.23}$$

with $(g_0, g_1, g_2) = (0.094, -0.329, 1.232)$. The scaled results are plotted in Figure 4.36(b). Also shown is the prediction given by equation (4.8). The deviations and scattering of the data are significantly larger for ellipses compared to any of the cylinder cases, but it is still observed that the less uniformity of the pack causes the higher permeability. Therefore, although the data are essentially collapsed onto the monodisperse case, it still diverges from the prediction especially at high porosity.

Finally, Figures 4.37-4.39 shows selected results of the flow patterns through random packs of ellipses with aspect ration $AR = 2.5$. Contours of the velocity magnitudes are shown in Figure 4.37. From these figures we see how the microstructure can alter the flow as it passes around the immersed bodies. Contours of pressure are shown in Figure 4.38. Note that at the higher porosity, the higher pressure field at the left end is felt deeper in the pack. This suggests that the pressure field is being blocked at the lower porosity. Note also

that the pressure inside the pack can exceed the absolute value of the prescribed pressures at the two ends of the pack. Finally, corresponding streamlines are plotted in Figure 4.39, which directly shows the flow pattern through the random pack.

### 4.5.4 Carman-Kozeny equation

The Carman-Kozeny and shape factors are plotted in Figure 4.40 as a function of porosity and for different values of the aspect ratio. Also shown as dash lines are the corresponding factors for slab flow; $\psi_{CK} = 120$ and $\Phi = 60$ assuming $\tau = \sqrt{2}$ [39]. In both cases the values used for slab flow under predict the computed values using random packs of ellipses. As pointed out in [39], the Carman-Kozeny and shape factors are not constant but depend on the details of the microstructure. Indeed, our results show that the factors depend not only on the porosity but also the aspect ratio.

## 4.6 Inertial effect in non-Darcy's regime

In this section inertial effects on the permeability in the non-Darcy's regime (i.e. $Re > 1.0$) is considered for random packs of monodisperse, bidisperse and polydisperse cylinders as well as ellipses. For this study, we selected one representative pack for each set of configurations with a permeability close to the mean (that is, $N_r = 1$), and tested the packs at $Re > 1.0$ up to the critical Reynolds number at which the flow becomes unsteady. The flow is solved until it reaches steady state, and the modified friction factors and the modified Reynolds numbers are computed by equation (3.6). Note that due to the randomness of the cylinder locations, the critical Reynolds number varies depending on the pack. The critical $Re$ is generally small at low porosity.

### 4.6.1 Monodisperse cylinders

To show the effect of Reynolds number, we first plot the friction factors for random packs of monodisperse cylinders. Figure 4.41(a) plots the friction factor $f_D$ as a function of particle Reynolds number and for porosities of $\sigma = 0.45$ and 0.7. Also shown as the solid line is Ergun's equation (1.5). It can be seen that Ergun's equation fails to predict the friction factor at the lower values of the porosity. This characteristic was observed for packs of regular arrays as shown on Section 3.4. The results are replotted in Figure 4.41(b) using the modified Reynolds number $Re_{\sqrt{K}}$. The friction factor $f_{\sqrt{K}}$ from the modified Forchheimer equation (3.6) is plotted as a solid curve. From the figure we see that Forchheimer equation predicts the modified friction factor, although at the higher Reynolds numbers the friction factors for the higher porosity begins to deviate from the curve. In the following sections, the Ergun's equation will not be considered and we will focus on the modified Forchheimer equation. We also show in Figure 4.42 contours of the velocity magnitude for creeping flow and for the inertial regime ($Re = 37.8$). It is quite notable that the flow paths remain almost unchanged in low and high $Re$ regimes.

### 4.6.2 Non-monodisperse cylinders

To examine the friction factor in the inertial regime, we have examined the following configurations. For each configuration, a representative pack (which has the permeability close to the mean value) is selected and tested.

1. Bidisperse cylinders at $\sigma = 0.45$, 0.60, 0.70, $D_R = 0.3$, 0.5, 0.7, $\mathcal{N} = 0.25$, 0.50 and 0.75
2. Polydisperse cylinders at $\sigma = 0.45$, 0.60, 0.70, $D_\sigma = 0.125, 0.250, 0.375$
3. Ellipses at $\sigma = 0.5$, 0.6, 0.7, 0.8, 0.9, $AR = 1.5$, 2.5, 3.0

.

The computed data are shown in Figure 4.43 for bidisperse cylinders, Figure 4.44 for polydisperse cylinders, and Figure 4.45 for ellipses. It is clearly seen that in the inertial flow regime, the modified Forchheimer equation cannot predict the friction factors, especially when the pack is less uniform. Hence the plots suggest that the fitting function $F$ should be a function of porosity as well as particle shapes. Here we propose the following form

$$F = \mathcal{F}\mathcal{C}\left(a + b\sigma + c\sigma^2\right), \tag{4.24}$$

where $\mathcal{F}$ is a function of particle shape, $\mathcal{C}$ is the circularity (sphericity in three dimensions), and $(a, b, c)$ are constants. First, it is required to have $\mathcal{F} = \mathcal{C} = 1$ for cylinders. The least square fit through the mono-, bi- and polydisperse cylinders yields $(a, b, c) = (0.8, -2.8333, 3.333)$. This form is similar to that given by [96], namely

$$F_{TWB} = \frac{\sigma}{1-\sigma}\left(A + B\sigma\right)^{-1/C}, \tag{4.25}$$

where $A, B, C$ are empirically fitted parameters that depend on the microstructure.

The circularity $\mathcal{C}$ is defined as $\mathcal{C} = 4\pi A/P^2$, where $A$ is the area of the disk and $P$ the perimeter, approximated for an ellipse by $P = \pi b\left[3(AR+1) - \sqrt{10AR + 3(AR^2+1)}\right]$. Since we lack the physical derivation of $\mathcal{F}$, we again use a least square fit to the following function

$$\mathcal{F} = AR\left[1 - d_0(AR-1)e^{[-d_1(AR-1)]}\right]. \tag{4.26}$$

And we found that $(d_0, d_1) = (0.8, 0.5)$. The fits are given in Figures 4.43 - 4.45 as solid lines, along with the original curve with $F = 0.08$ as a dashed line.

Finally, we show in Figure 4.46 contours of the velocity magnitude for a pack of polydisperse cylinders at creeping flow and for the inertial regime ($Re = 51.9$) and for $\sigma = 0.7$, $D_\sigma = 0.375$. Also shown in Figure (4.47) are contours of the velocity magnitude for a pack of ellipses at $\sigma = 0.6$ and $AR = 2.5$. Note the difference in scales of the magnitude. In both

cases it is observed that the flow paths remain approximately the same at both low and high $Re$, with only the magnitude increased.

## 4.7 Figures

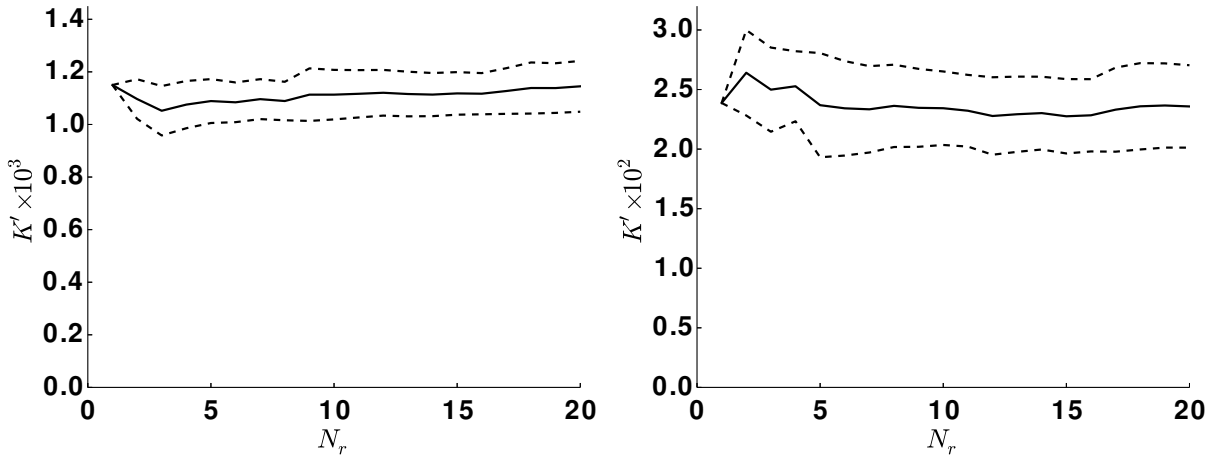


(a) $\sigma$=0.45 (b) $\sigma$=0.7

Figure 4.1: Mean normalized permeability $K' = \langle K \rangle / L_p^2$ (solid line) and standard deviation (dashed line) as a function of ensemble number $N_r$ for random packs of monodisperse cylinders. Here, particle number $N_p = 200$.

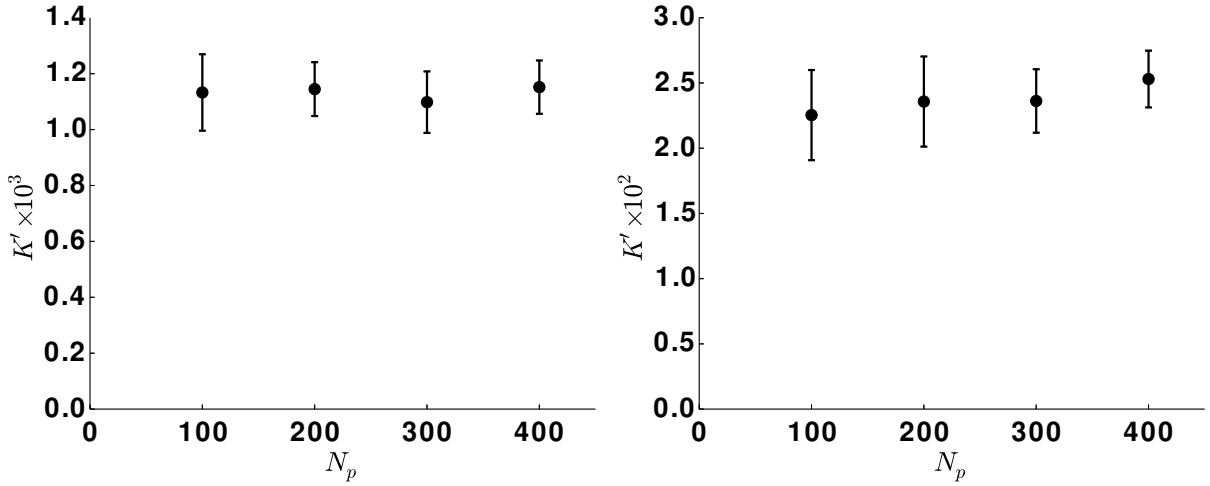


(a) $\sigma$=0.45 (b) $\sigma$=0.7

Figure 4.2: Mean normalized permeability $K' = \langle K \rangle / L_p^2$ (symbol) and standard deviation (error bar) as a function of particle number $N_p$ for random packs of monodisperse cylinders. Here, ensemble number $N_r = 20$.

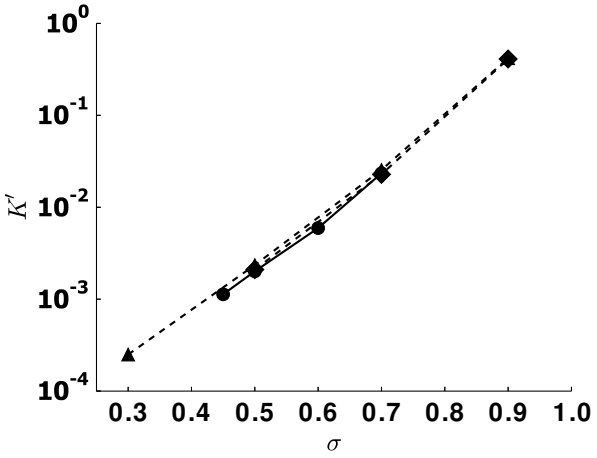


Figure 4.3: Plot of mean normalized permeability $K' = \langle K \rangle / L_p^2$ as a function of porosity $\sigma$ (circle). Also shown are results from [15] (triangle) and [39] (diamond).

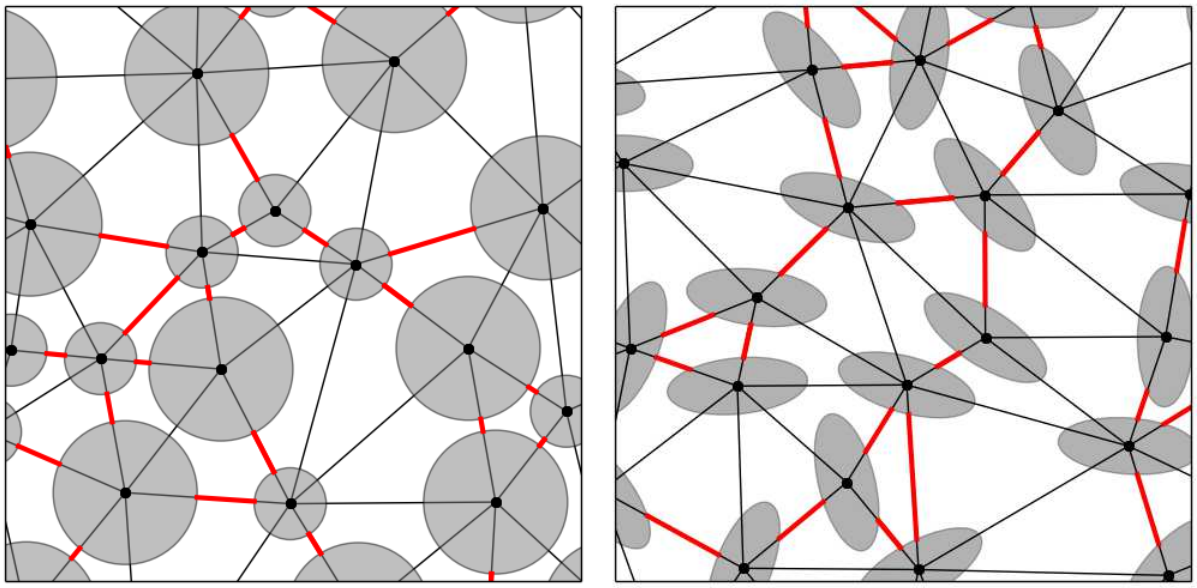

(a) Bidisperse cylinders (b) Monodisperse ellipse

Figure 4.4: Particles and the corresponding shortest Delaunay edges for the packs of (a) bidisperse cylinders and (b) monodisperse ellipses. Shown are the edges of Delaunay triangles (black line) and the shortest Delaunay edge for each triangle (red line) defined on table (4.2).

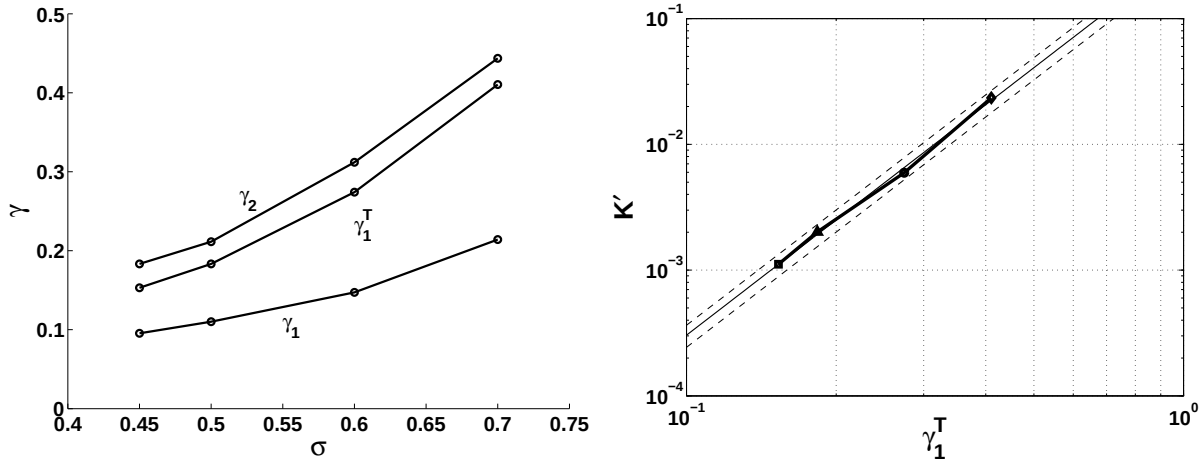


(a) Relevant length scale (b) Mean normalized permeability

Figure 4.5: (a) Plot of $\gamma_1$, $\gamma_2$, and $\gamma_1^T$ as a function of porosity $\sigma$. (b) Plot of mean normalized permeability $K' = \langle K \rangle / L_p^2$ as a function of $\gamma_1^T$ for $\sigma = 0.45$ (square), $\sigma = 0.5$ (triangle), $\sigma = 0.6$ (circle), and $\sigma = 0.7$ (diamond). Also shown is the fit given by equation (4.8) (solid), with $\pm 20\%$ variations (dash).

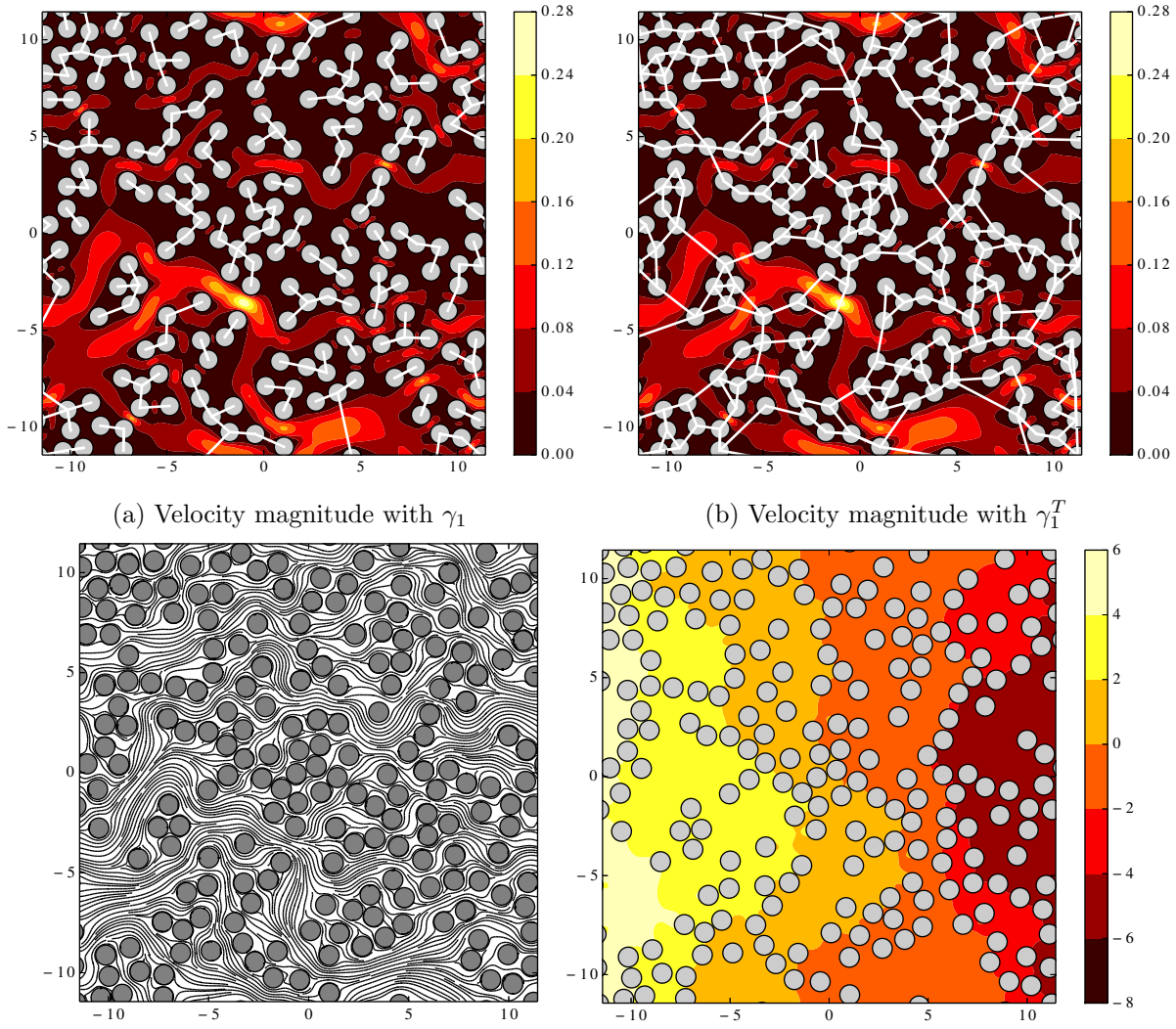


(a) Velocity magnitude with $\gamma_1$

(b) Velocity magnitude with $\gamma_1^T$

(c) Streamlines

(d) Pressure

Figure 4.6: Flow field of a monodisperse pack for $\sigma = 0.7$. (a) Contour of velocity magnitude with $\gamma_1$ (white line), (b) Contour of velocity magnitude with $\gamma_1^T$ (white line), (c) Streamlines, (d) Contour of pressure

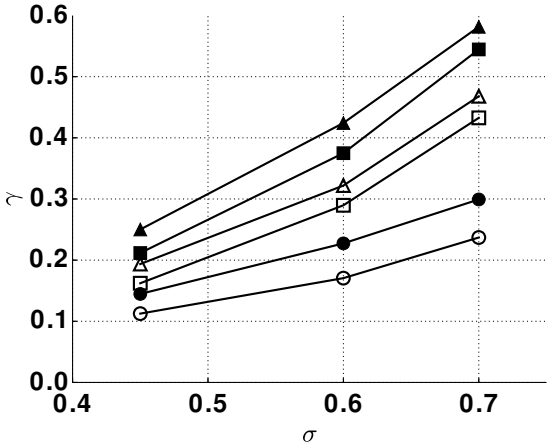


(a) Relevant length scale

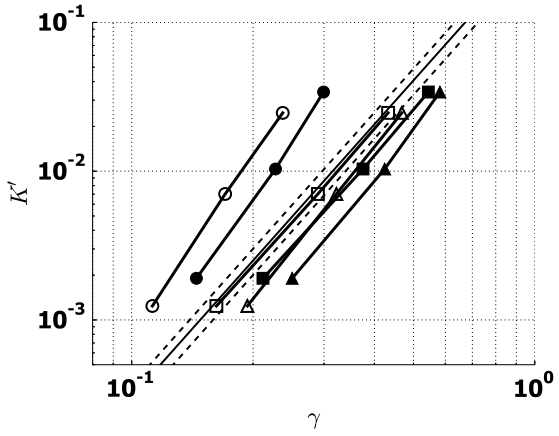


(b) Mean normalized permeability

Figure 4.7: (a) Plot of $\gamma_1$ (circle), $\gamma_2$ (triangle) and $\gamma_1^T$ (square) as a function of porosity $\sigma$. (b) Plot of the normalized permeability $K' = \langle K \rangle / L_p^2$ as a function of porosity $\sigma$ and diameter ratio $D_R$ at large-to-total particle ratio $\mathcal{N} = 0.5$ fixed. Here, $D_R = 0.3$ (filled); 0.7 (blank). Also shown is the fit given by equation (4.8) (solid line) with $\pm 20\%$ variations (dashed line).

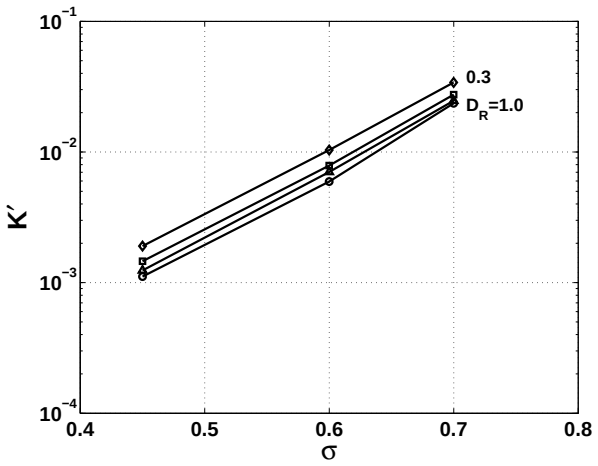


(a) Unscaled

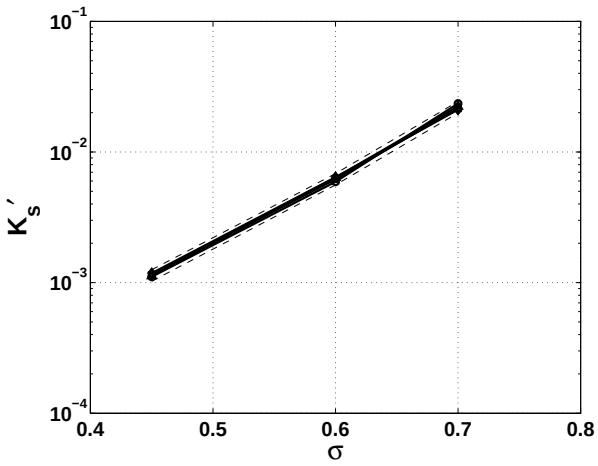


(b) Scaled

Figure 4.8: Plot of mean normalized permeability $K' = \langle K \rangle / L_p^2$ as a function of porosity $\sigma$ and for various values of the diameter ratio $D_R$ at large-to-total particle ratio $\mathcal{N} = 0.5$ fixed. In (b) the mean normalized permeability is scaled according to equation (4.9). The dashed lines in (b) corresponds to $\pm 10\%$ of the mean. Here, $D_R = 1.0$ (circle); 0.7 (triangle); 0.50 (square); and 0.30 (diamond). Diameter ratios of 1.0 and 0.3 are marked in (a).

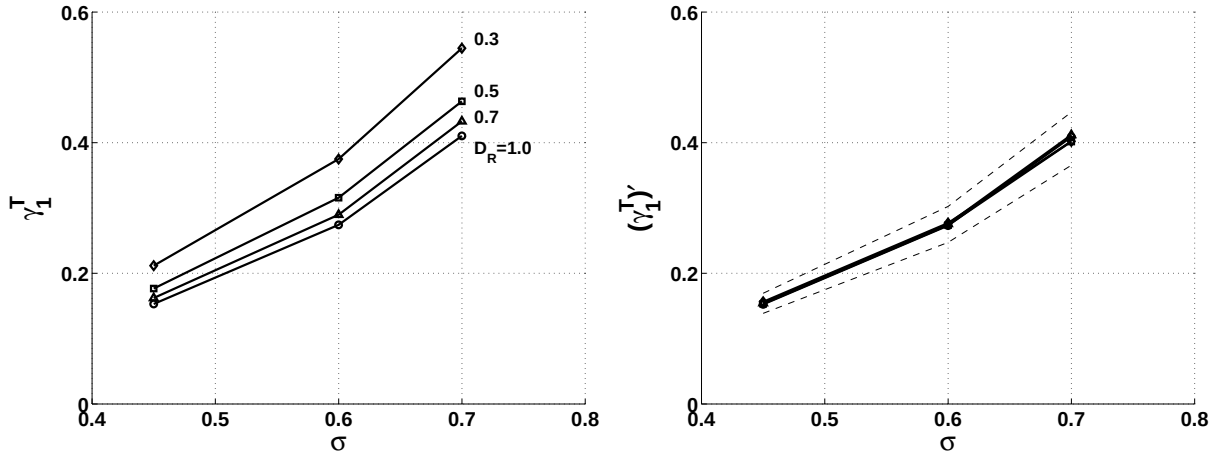


(a) Unscaled (b) Scaled

Figure 4.9: Plot of mean shortest Delaunay edge $\gamma_1^T$ as a function of porosity $\sigma$ and for various values of the diameter ratio $D_R$ at large-to-total particle ratio $\mathcal{N} = 0.5$ fixed. In (b) $\gamma_1^T$ is scaled according to equation (4.10). The dashed lines in (b) corresponds to $\pm 10\%$ of the mean. Here, $D_R = 1.0$ (circle); 0.7 (triangle); 0.50 (square); and 0.30 (diamond). Diameter ratios are marked in (a).

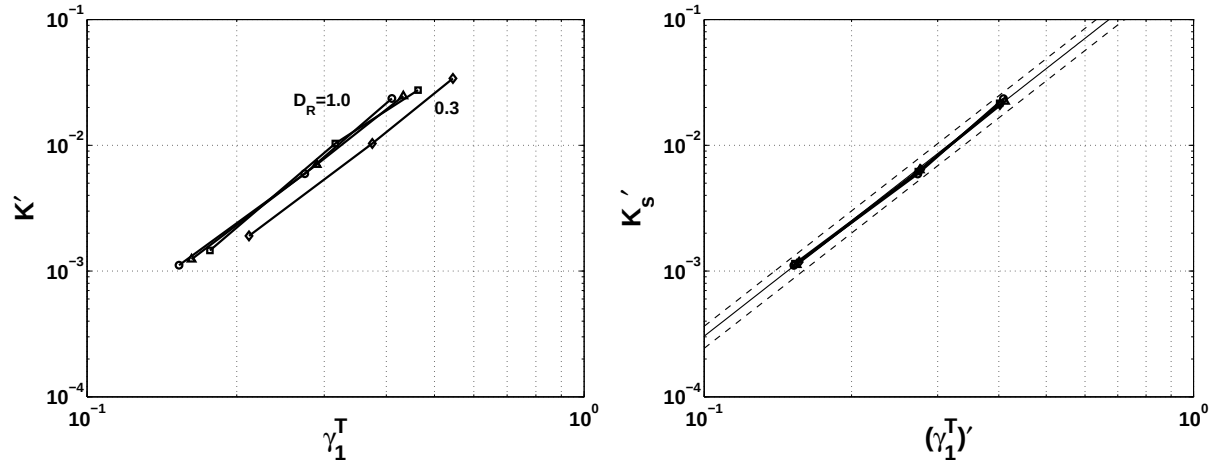


(a) Unscaled (b) Scaled

Figure 4.10: Plot of mean normalized permeability $K' = \langle K \rangle / L_p^2$ as a function of $\gamma_1^T$ and for various values of the diameter ratio $D_R$ at large-to-total particle ratio $\mathcal{N} = 0.5$ fixed. In (b) the mean normalized permeability and $\gamma_1^T$ are scaled. Also shown in (b) is the fit given by equation (4.8) (solid), with $\pm 20\%$ variations (dash). Here, $D_R = 1.0$ (circle); 0.7 (triangle); 0.50 (square); and 0.30 (diamond). Diameter ratios of 1.0 and 0.3 are marked in (a).

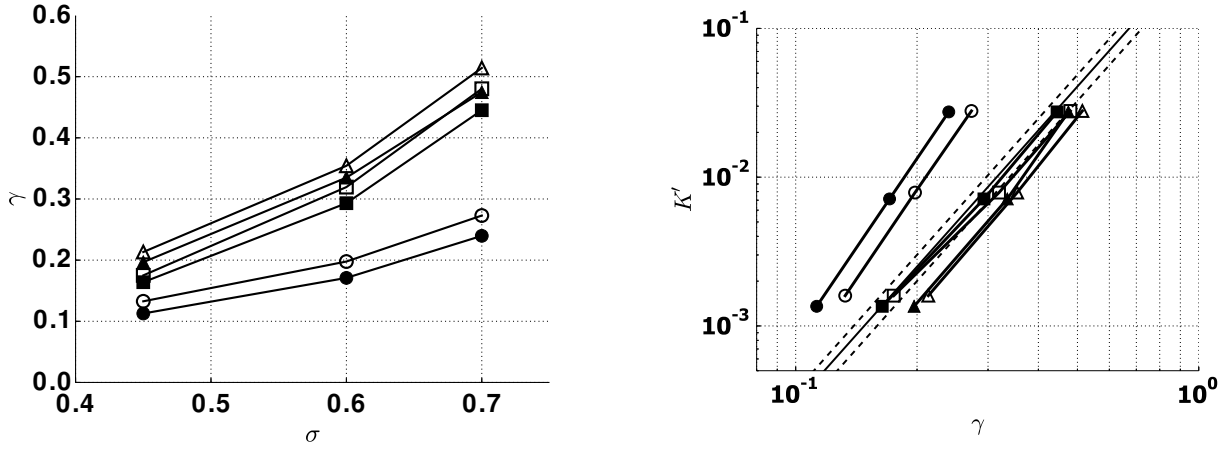


(a) Relevant length scale

(b) Mean normalized permeability

Figure 4.11: (a) Plot of $\gamma_1$ (circle), $\gamma_2$ (triangle) and $\gamma_1^T$ (square) as a function of porosity $\sigma$. (b) Plot of the mean normalized permeability $K' = \langle K \rangle / L_p^2$ as a function of various $\gamma$ at diameter ratio $D_R = 0.5$ fixed. Here, large-to-total particle ratio $\mathcal{N} = 0.25$ (filled); 0.75 (blank). Also shown is the fit given by equation (4.8) (solid line) with $\pm 20\%$ variations (dashed line).

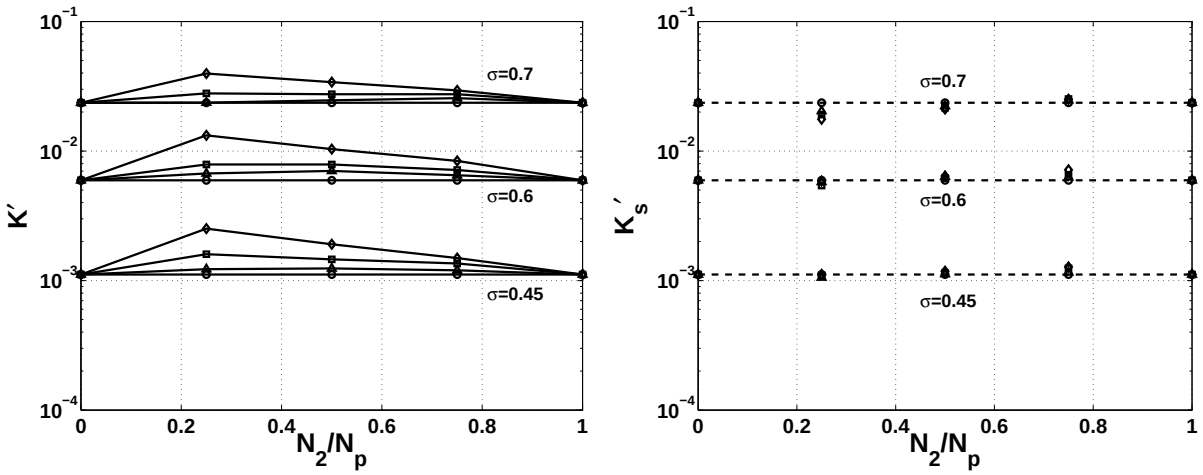


(a) Unscaled

(b) Scaled

Figure 4.12: Plot of mean normalized permeability $K' = \langle K \rangle / L_p^2$ as a function of large-to-total particle ratio $\mathcal{N}$ and for various values of the porosity $\sigma$ and diameter ratio $D_R$. In (b) the permeability is scaled according to equation (4.11). Here, $D_R = 1.0$ (circle); 0.7 (triangle); 0.50 (square); and 0.30 (diamond). Values of $\sigma$ are marked.

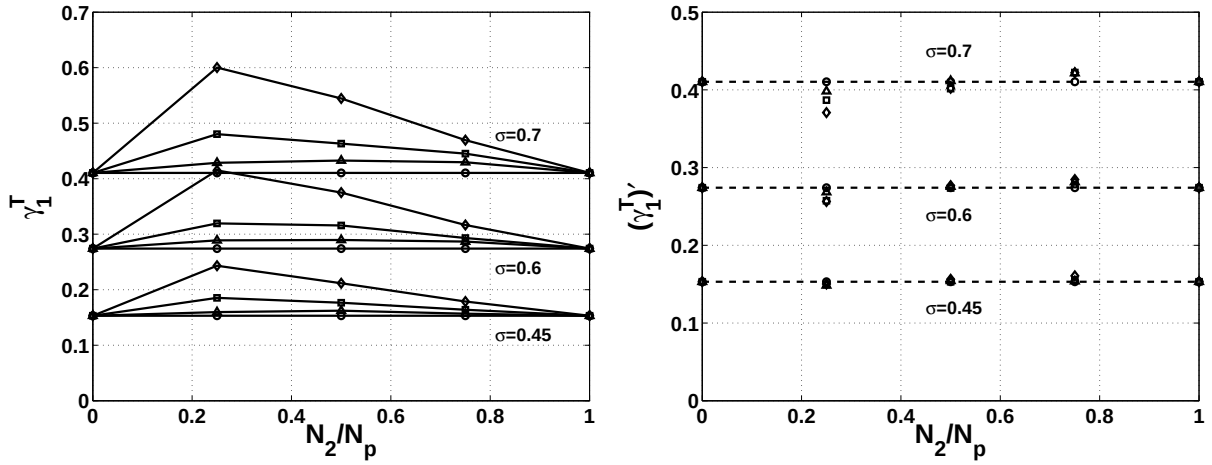


(a) Unscaled (b) Scaled

Figure 4.13: Plot of mean shortest Delaunay edge $\gamma_1^T$ as a function of large-to-total particle ratio $\mathcal{N}$ and for various values of the porosity $\sigma$ and diameter ratio $D_R$. In (b) the permeability is scaled according to equation (4.13). Here, $D_R = 1.0$ (circle); 0.7 (triangle); 0.50 (square); and 0.30 (diamond). Values of $\sigma$ are marked.

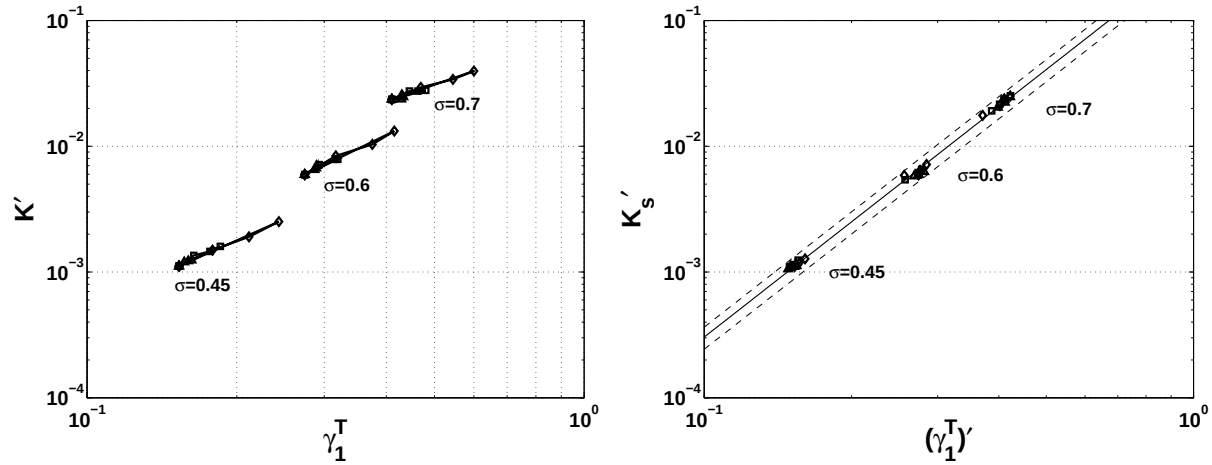


(a) Unscaled (b) Scaled

Figure 4.14: Plot of mean normalized permeability $K' = \langle K \rangle / L_p^2$ as a function of mean shortest Delaunay edge $\gamma_1^T$ and for various values of large-to-total particle ratio $\mathcal{N}$, porosity $\sigma$, and diameter ratio $D_R$. In (b) the permeability and $\gamma_1^T$ are scaled. Also shown in (b) is the fit given by equation (4.8) (solid), with $\pm 20\%$ variations (dash). Here, $D_R = 1.0$ (circle); 0.7 (triangle); 0.50 (square); and 0.30 (diamond). Values of $\sigma$ are marked.

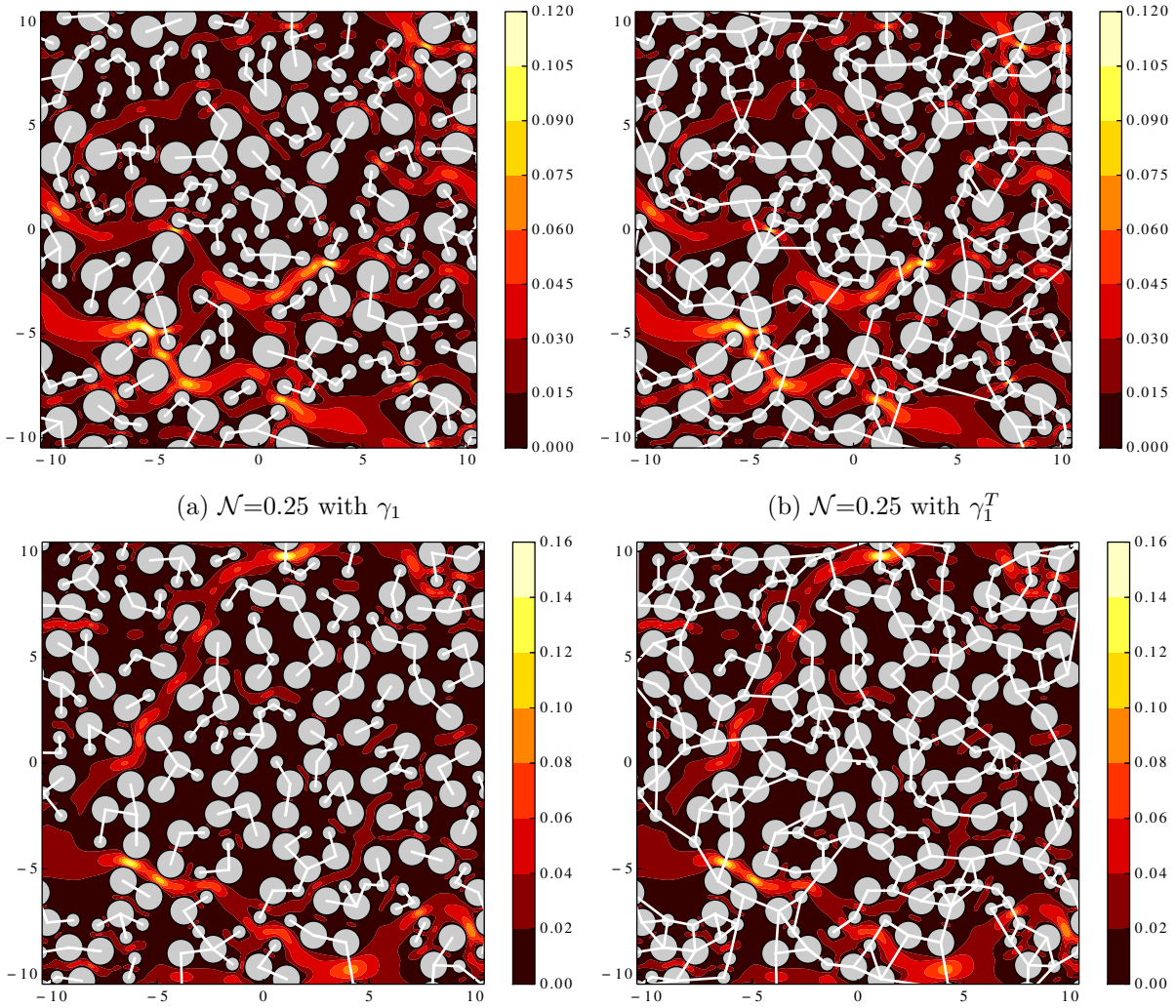


(a) $\mathcal{N}$=0.25 with $\gamma_1$

(b) $\mathcal{N}$=0.25 with $\gamma_1^T$

(c) $\mathcal{N}$=0.50 with $\gamma_1$

(d) $\mathcal{N}$=0.50 with $\gamma_1^T$

Figure 4.15: Contour plot of velocity magnitude for bidisperse packs with $\sigma = 0.6$, $D_R = 0.5$, and for large-to-total particle ratio $\mathcal{N} = 0.25$ with (a) first nearest neighbor and (b) for shortest Delaunay edges; and for $\mathcal{N} = 0.5$ with (c) first nearest neighbor and (d) for shortest Delaunay edges.

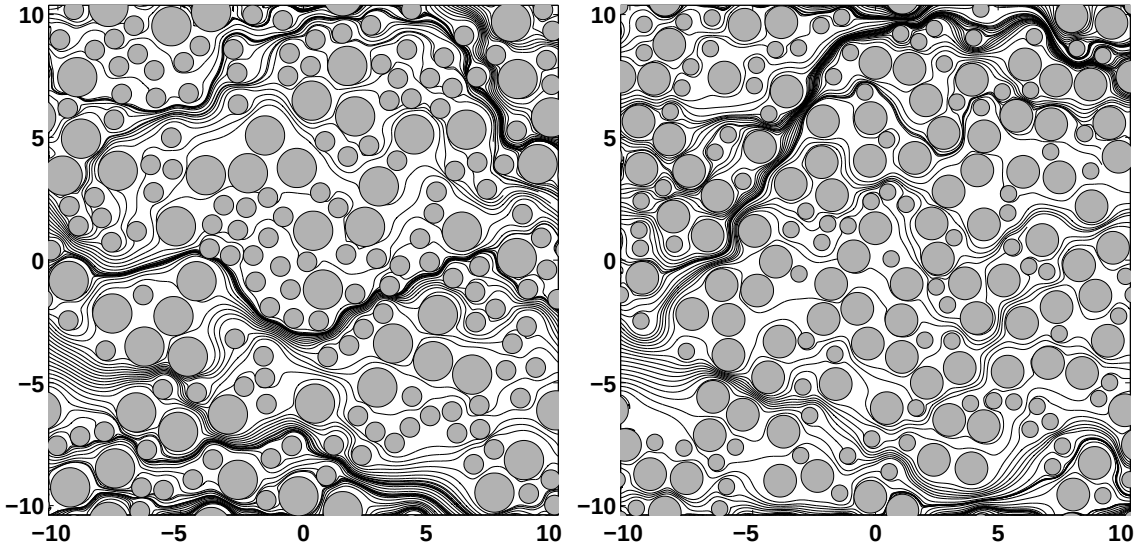


(a) $\mathcal{N}$=0.25 (b) $\mathcal{N}$=0.50

Figure 4.16: Streamlines of bidisperse packs for $\sigma = 0.6$, $D_R = 0.5$ and large-to-total particle ratio (a) $\mathcal{N} = 0.25$ and (b) $\mathcal{N} = 0.5$.

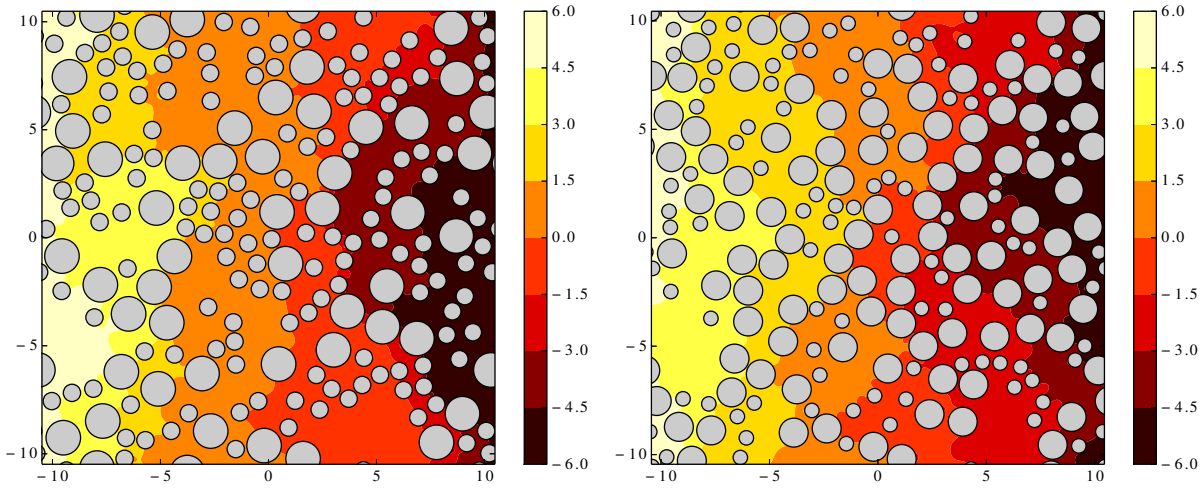


(a) $\mathcal{N}$=0.25 (b) $\mathcal{N}$=0.50

Figure 4.17: Pressure contours of bidisperse packs for $\sigma = 0.6$, $D_R = 0.5$ and large-to-total particle ratio (a) $\mathcal{N} = 0.25$ and (b) $\mathcal{N} = 0.5$.

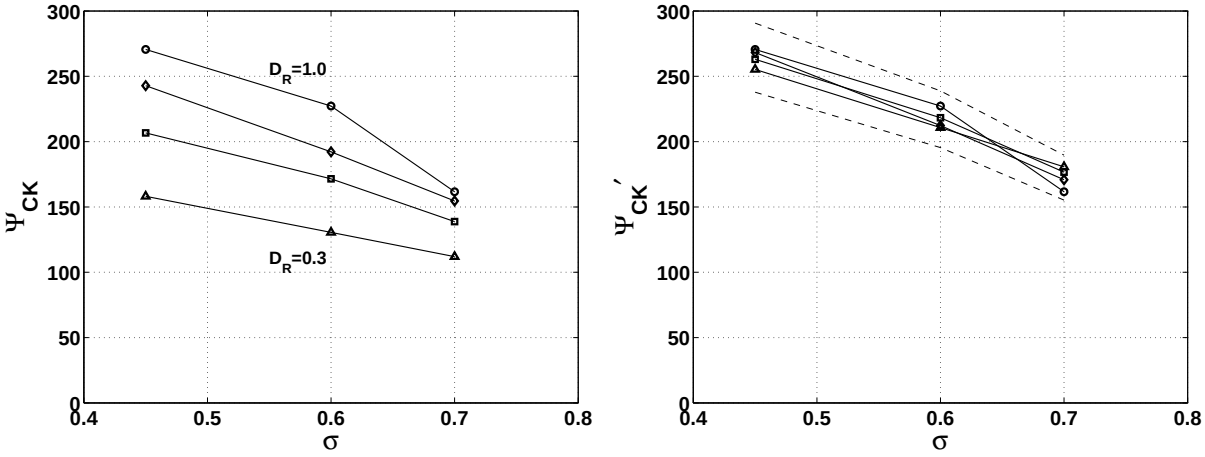


(a) Unscaled

(b) Scaled

Figure 4.18: Carman-Kozeny factor ($\Psi_{CK}$) as a function of porosity $\sigma$ at large-to-total particle ratio $\mathcal{N} = 0.5$ fixed. In (b) $\Psi_{CK}$ is scaled according to equation (4.17) with $\pm 10\%$ of the mean (dashed line). Here, $D_R = 1.0$ (circle); 0.7 (diamond); 0.50 (square); and 0.30 (triangle).

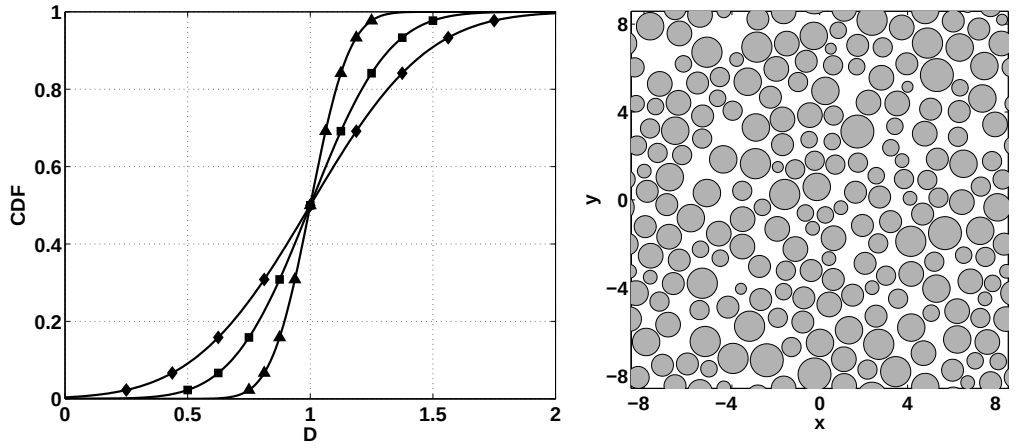


(a) CDF

(b) Random pack

Figure 4.19: (a) Plot of cumulative distribution function (CDF) as a function of diameter $D$ showing particle size distributions with $D_\sigma = 0.125$ (triangle), 0.25 (square), and 0.375 (diamond). (b) Representative random pack for $D_\sigma = 0.25$ and porosity $\sigma = 0.45$.

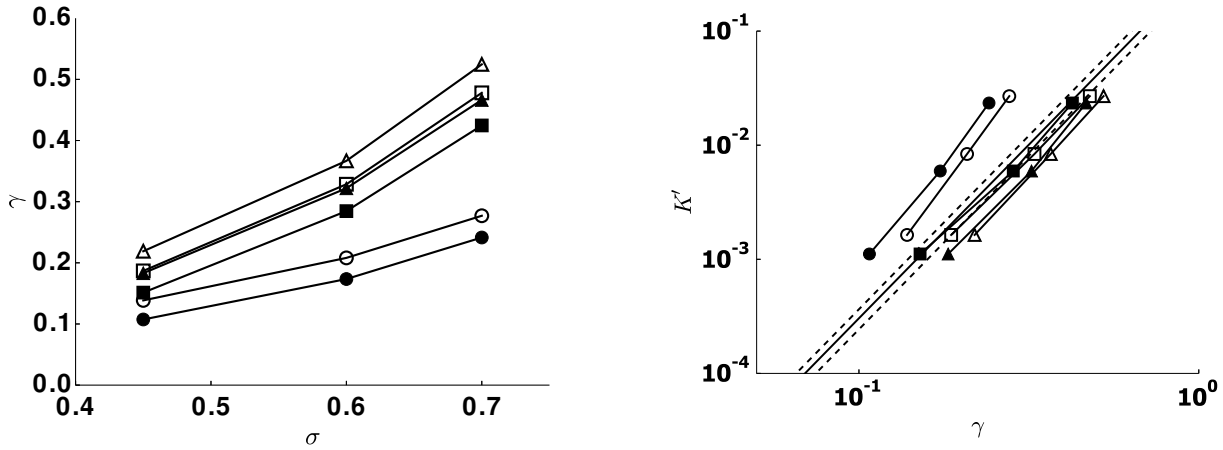


(a) Relevant length scale

(b) Mean normalized permeability

Figure 4.20: (a) Plot of $\gamma_1$ (circle), $\gamma_2$ (triangle) and $\gamma_1^T$ (square) as a function of porosity. (b) Plot of the normalized permeability $K' = \langle K \rangle / L_p^2$ as a function of porosity. Here, $D_\sigma = 0.0$ (filled); 0.375 (blank). Shown as a dashed line is the fit by equation 4.8.

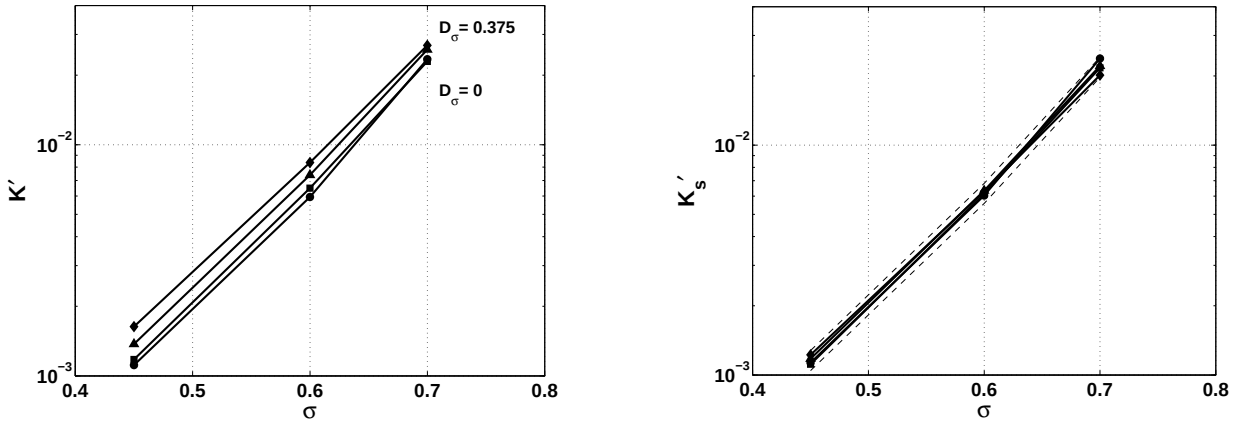


(a) Unscaled (b) Scaled

Figure 4.21: Plot of mean normalized permeability $K' = \langle K \rangle / L_p^2$ as a function of porosity and for various values of $D_\sigma$. In (b) the permeability is scaled according to equation (4.19). The dashed lines in (b) corresponds to $\pm 10\%$ of the mean. Here, $D_\sigma = 0.0$ (circle); 0.125 (square); 0.25 (triangle); 0.375 (diamond). Diameter variations are marked in (a).

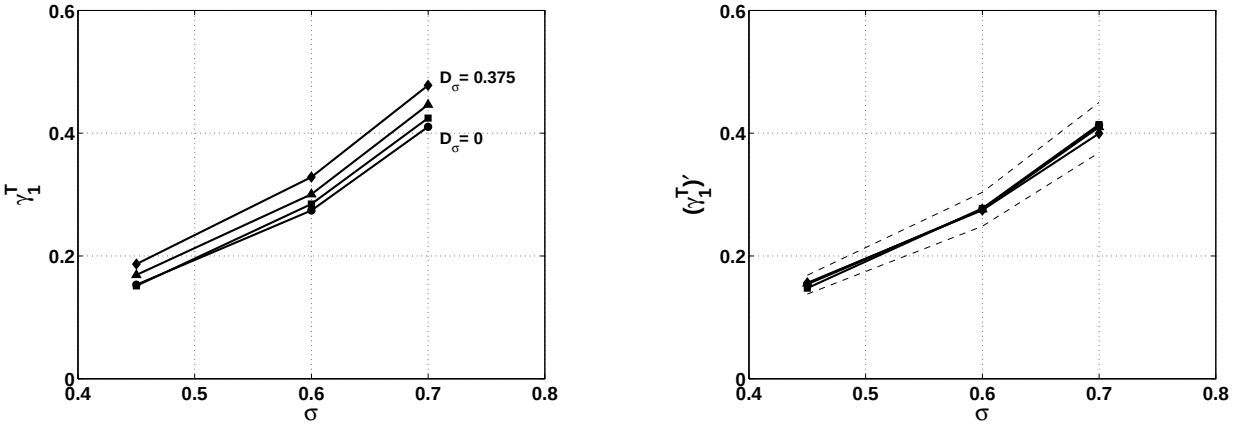


(a) Unscaled (b) Scaled

Figure 4.22: Plot of mean shortest Delaunay edge $\gamma_1^T$ as a function of porosity and various values of diameter variations $D_\sigma$. In (b) $\gamma_1^T$ is scaled according to equation (4.20). The dashed lines in (b) corresponds to $\pm 10\%$ of the mean. Here, $D_\sigma = 0.0$ (circle); 0.125 (square); 0.25 (triangle); 0.375 (diamond). Values of $D_\sigma$ are marked in (a).

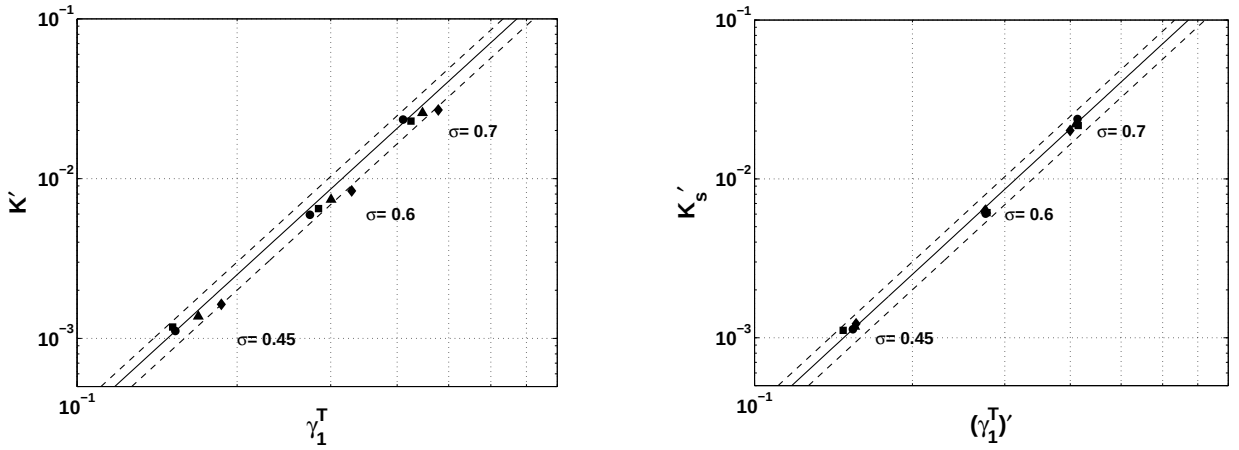


(a) Unscaled (b) Scaled

Figure 4.23: Plot of mean normalized permeability $K' = \langle K \rangle / L_p^2$ as a function of mean shortest Delaunay edge $\gamma_1^T$ and for various values of porosity $\sigma$ and diameter variation $D_\sigma$. In (b) the permeability and $\gamma_1^T$ are scaled. Also shown in (b) is the fit given by equation (4.8) (solid), with $\pm 20\%$ variations (dash). Here, $D_\sigma = 0.0$ (circle); 0.125 (square); 0.25 (triangle); 0.375 (diamond). Values of $\sigma$ are marked.

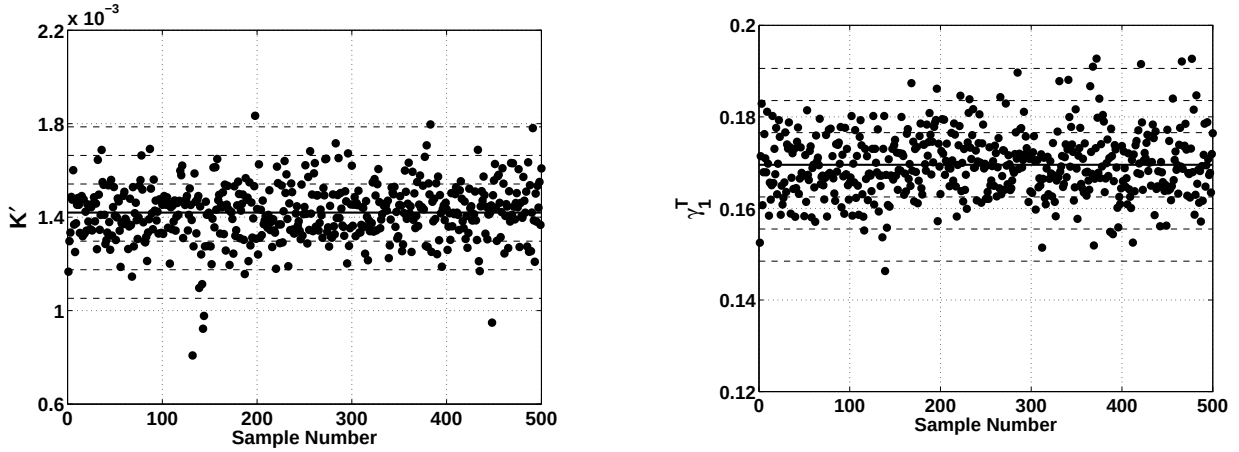


(a) $K'$ (b) $\gamma_1^T$

Figure 4.24: Distributions of (a) mean normalized permeability $K' = K/L_p^2$ and (b) $\gamma_1^T$ for 500 random packs of polydisperse cylinders with $\sigma = 0.45$ and $D_\sigma = 0.25$. Also shown is the mean value (solid) and standard deviations $\pm 1.0\sigma_{std}$, $\pm 2.0\sigma_{std}$, $\pm 3.0\sigma_{std}$ (dash).

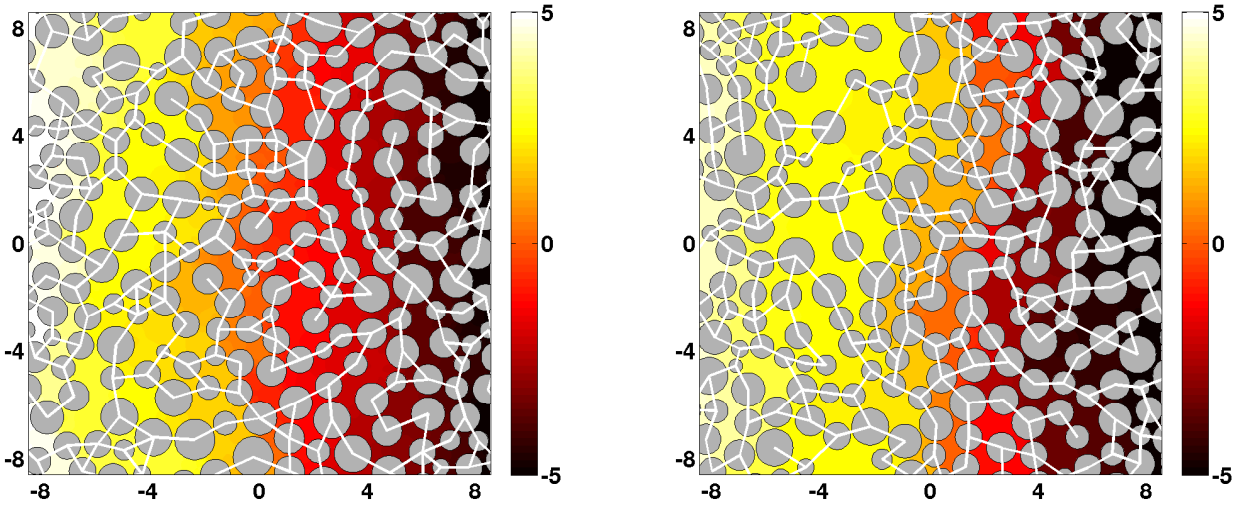


(a) Close to the mean (b) Rare event

Figure 4.25: Contour plots of pressure of polydisperse packs with porosity $\sigma = 0.45$, $D_\sigma = 0.25$ and for (a) a pack with permeability close to the mean, and (b) a pack for a rare event. Also shown as white line segments are the shortest edge of each Delaunay triangle. Here, $\Delta p = 10$.

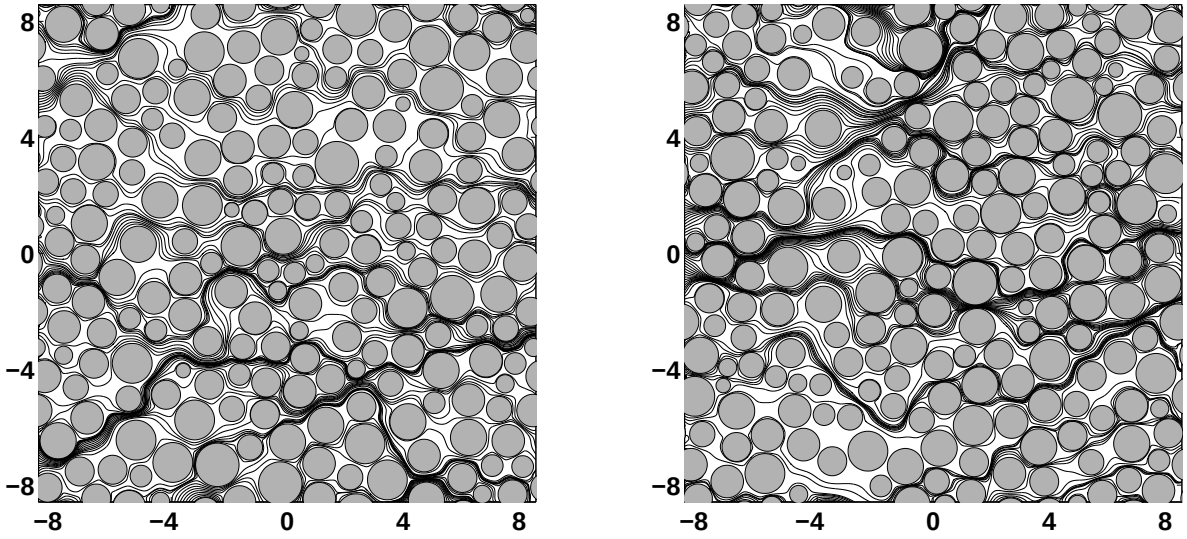


(a) Close to the mean (b) Rare event

Figure 4.26: Streamlines of polydisperse packs with porosity $\sigma = 0.45$, $D_\sigma = 0.25$ and for (a) pack with permeability close to the mean, and (b) pack for a rare event.

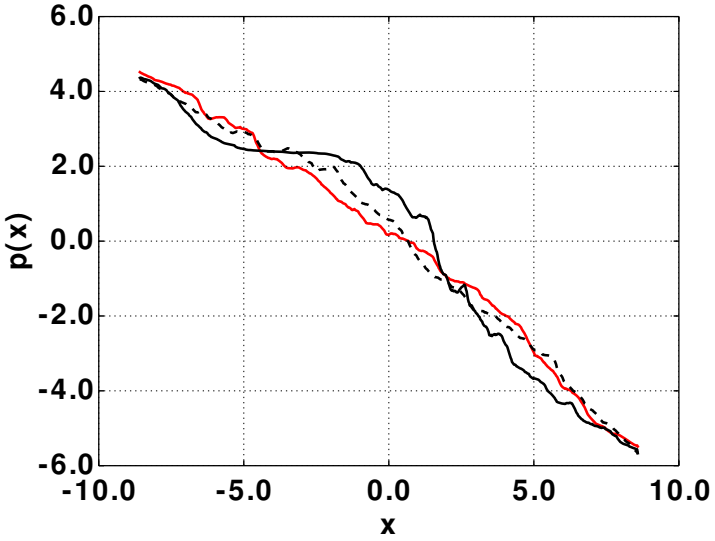


Figure 4.27: Plot of the pressure profile along the flow direction for a pack with the mean permeability (red line), a rare event with the permeability $K' = 0.81E-03$ (solid black line) and a rare event with the permeability $K' = 1.83E-03$ (dashed black line).

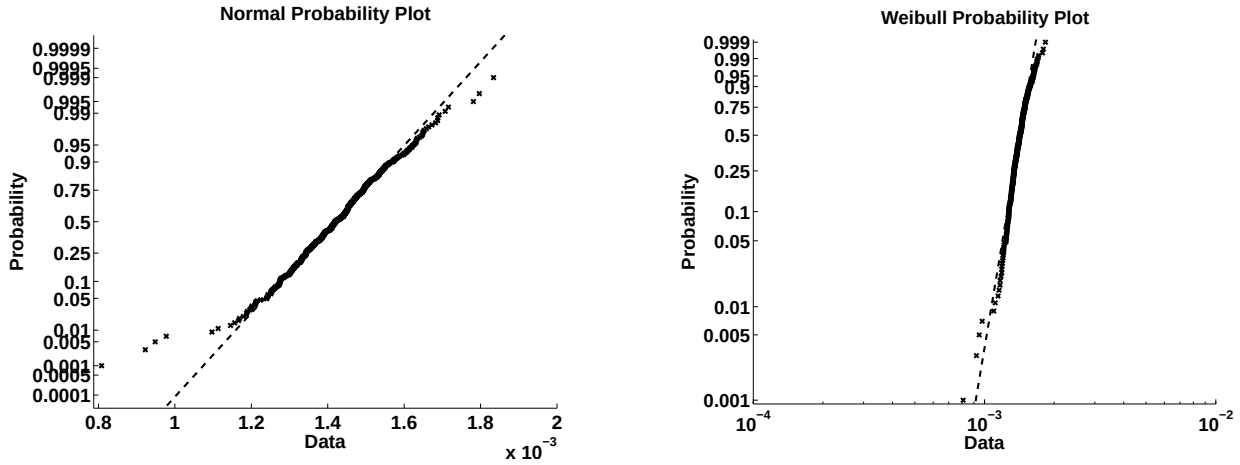


(a) Normal distribution

(b) Weibull distribution

Figure 4.28: Probability plots of the mean normalized permeability $K' = K/L_p^2$ over 500 samples and for $\sigma = 0.45$, $D_\sigma = 0.25$.

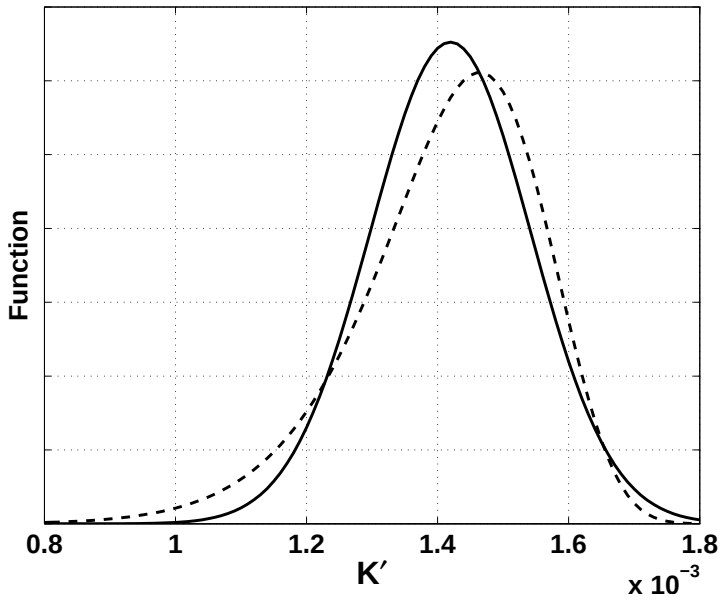


Figure 4.29: Plot of normal (solid line) and Weibull (dashed line) distributions as a function of normalized permeability $K' = K/L_p^2$ and for $\sigma = 0.45$, $D_\sigma = 0.25$.

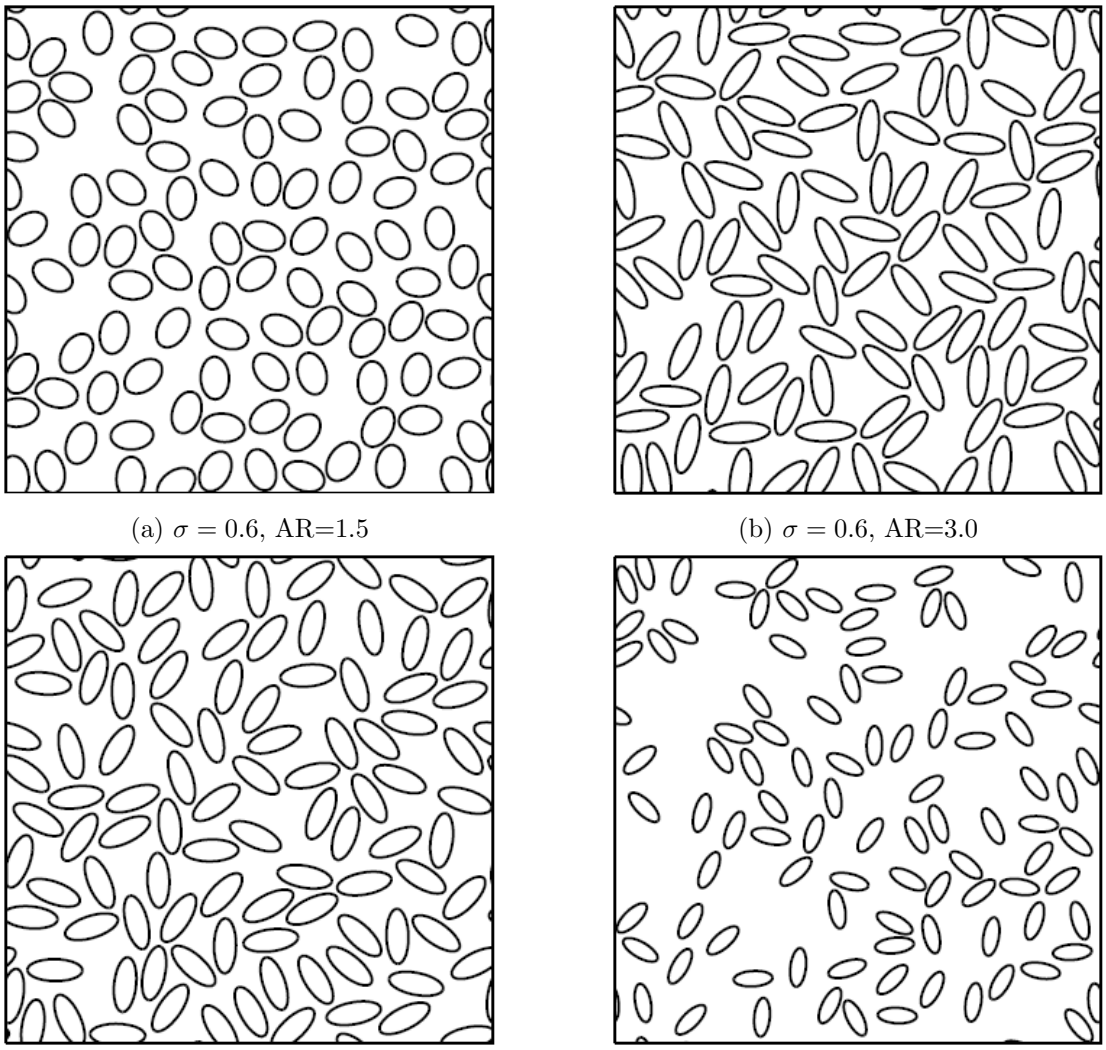

(a) $\sigma = 0.6$, AR=1.5

(b) $\sigma = 0.6$, AR=3.0

(c) $\sigma = 0.5$, AR=2.5

(d) $\sigma = 0.8$, AR=2.5

Figure 4.30: Periodic random packs of monodisperse ellipses for various aspect ratio $AR$ and porosity $\sigma$ with $N_p = 100$ particles.

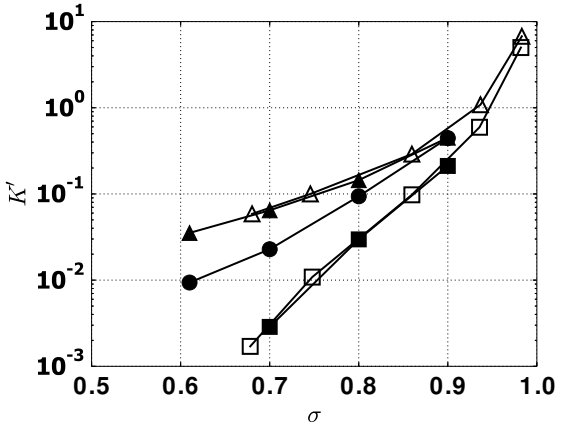


(a) Normalized permeability

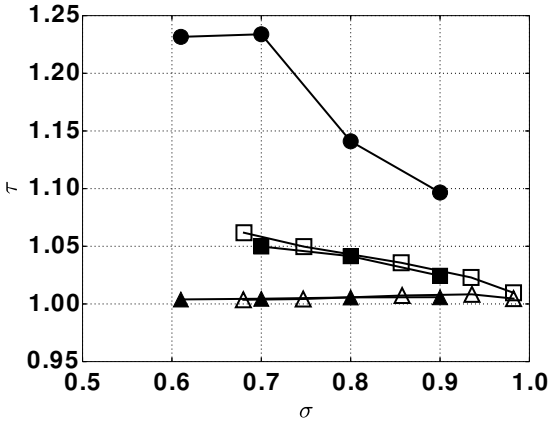


(b) Tortuosity1

Figure 4.31: (a) Normalized permeability $K' = \langle K \rangle / L_p^2$ and (b) tortuosity $\tau$ as a function of porosity $\sigma$ for a single ellipse and random packs. Here, an angle of the single ellipse $0^o$ (triangle) and $90^o$ (square), random (circle) with aspect ratio $AR = 2.0$ fixed. The closed symbols are from the current work, the open symbols from [37].

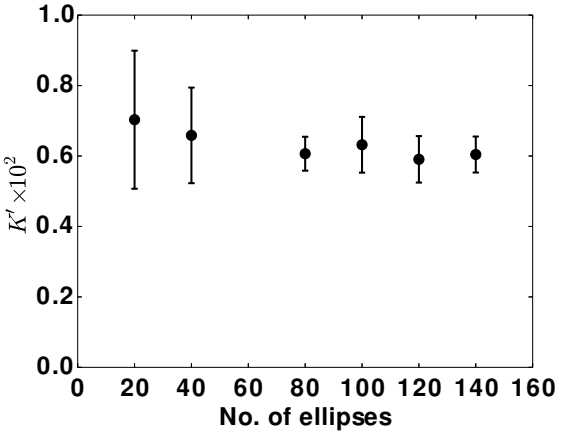


(a) Normalized permeability

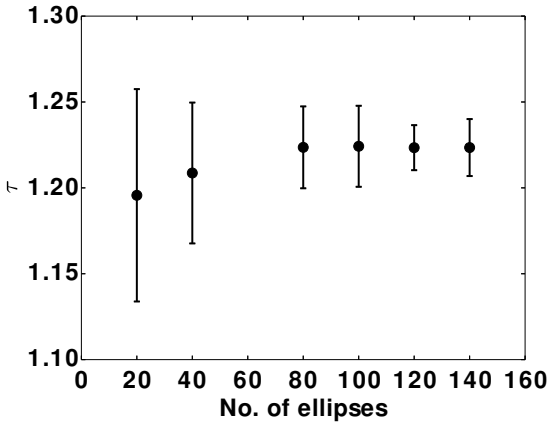


(b) Tortuosity

Figure 4.32: Mean normalized permeability $K' = \langle K \rangle / L_p^2$ (symbol) and standard deviation (error bar) as a function of particle number $N_p$ for random packs of monodisperse ellipses with porosity $\sigma = 0.7$ and aspect ratio $AR = 2.5$. Here, ensemble number $N_r = 15$.

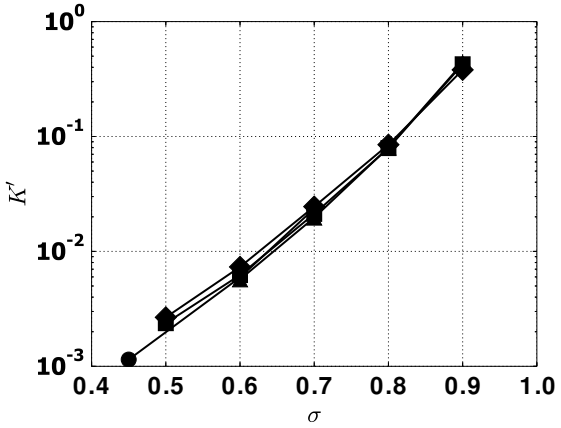


(a) Normalized permeability

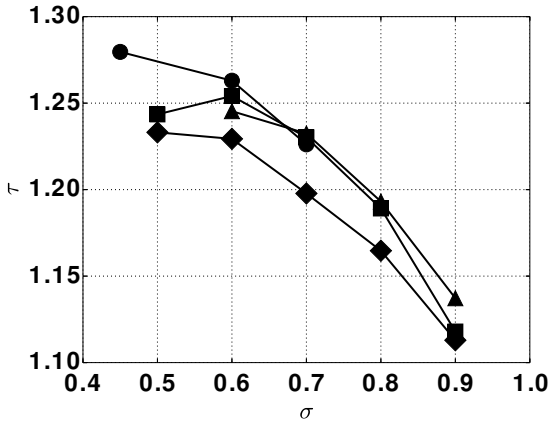


(b) Tortuosity

Figure 4.33: (a) Normalized permeability $K' = \langle K \rangle / L_p^2$ and (b) tortuosity $\tau$ as a function of porosity $\sigma$ and for various values of aspect ratio $AR$. Here, $AR = 1$ (circle); 1.5 (diamond); 2.5 (square); and 3.0 (triangle).

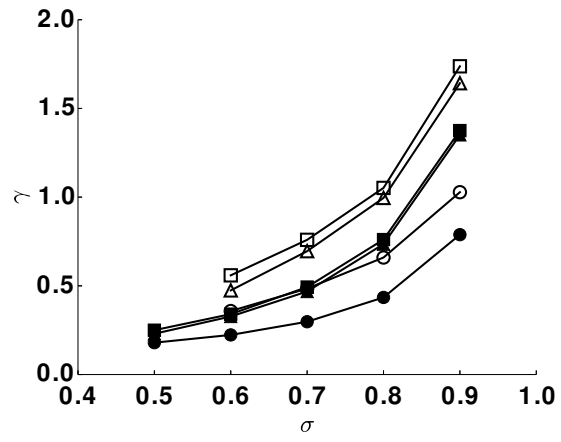


(a) Relevant length scale

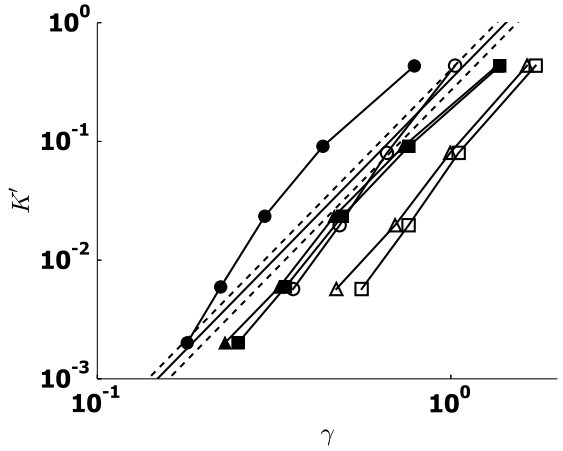


(b) Mean normalized permeability

Figure 4.34: (a) Plot of $\gamma_1$ (circle), $\gamma_2$ (triangle) and $\gamma_1^T$ (square) as a function of porosity $\sigma$. (b) Plot of the normalized permeability $K' = \langle K \rangle / L_p^2$ as a function of porosity $\sigma$. Here, $AR = 1.5$ (filled); 3.0 (blank). Also shown is the fit given by equation (4.8) (solid line) with $\pm 20\%$ variations (dashed line).

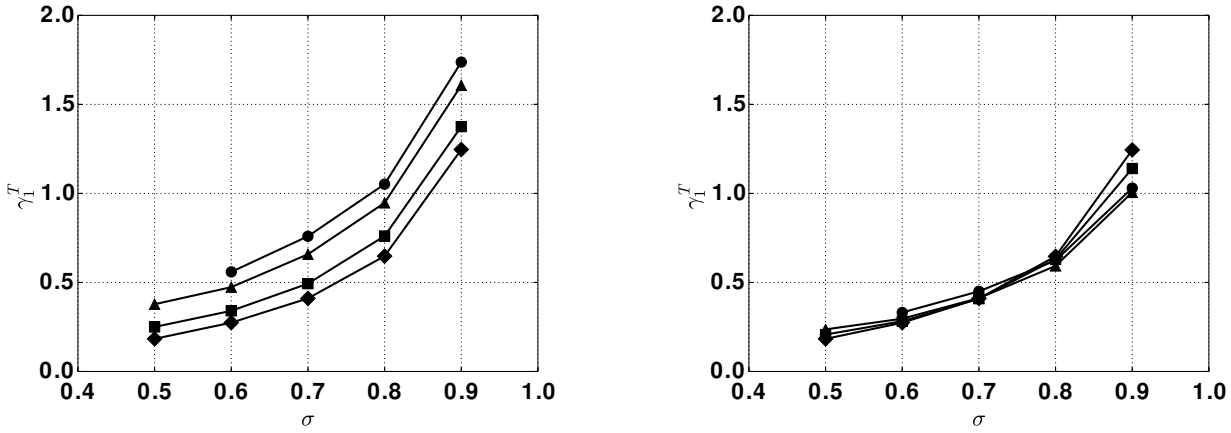


(a) Unscaled (b) Scaled

Figure 4.35: Plot of mean shortest Delaunay edge $\gamma_1^T$ as a function of porosity $\sigma$ and various aspect ratio $AR$. In (b) $\gamma_1^T$ is scaled according to equation (4.22). Here, AR=1.0 (diamond); AR=1.5 (square); AR=2.5 (triangle); AR=3.0 (circle).

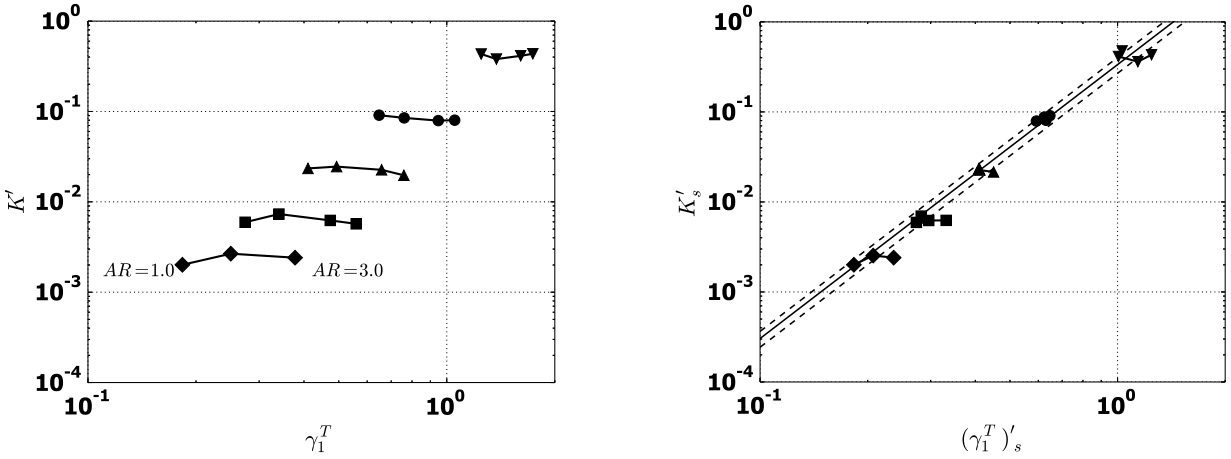


(a) Unscaled (b) Scaled

Figure 4.36: Plot of mean normalized permeability $K' = \langle K \rangle / L_P^2$ as a function of mean shortest Delaunay edge $\gamma_1^T$ and for various values of porosity $\sigma$ and aspect ratio $AR$. In (b) the permeability and $\gamma_1^T$ are scaled. Also shown in (b) is the fit given by equation (4.8) (solid), with $\pm 20\%$ variations (dash). Here, $\sigma = 0.5$ (diamond); 0.6 (square); 0.7 (triangle); 0.8 (circle); 0.9 (inverted triangle). Values of AR are marked in (a).

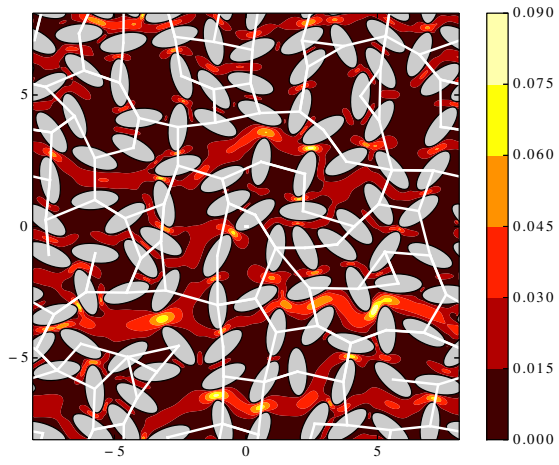


(a) $\sigma = 0.6$

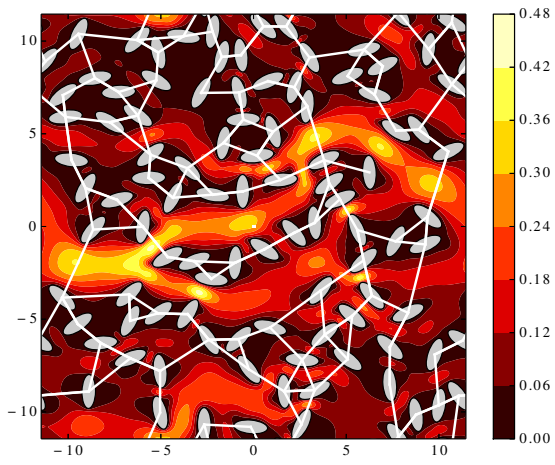


(b) $\sigma = 0.8$

Figure 4.37: Contours of the velocity magnitude through a pack at $AR = 2.5$ and porosity (a) $\sigma = 0.6$ and (b) 0.8. The white line segments corresponds to the shortest edge of each Delaunay triangle.

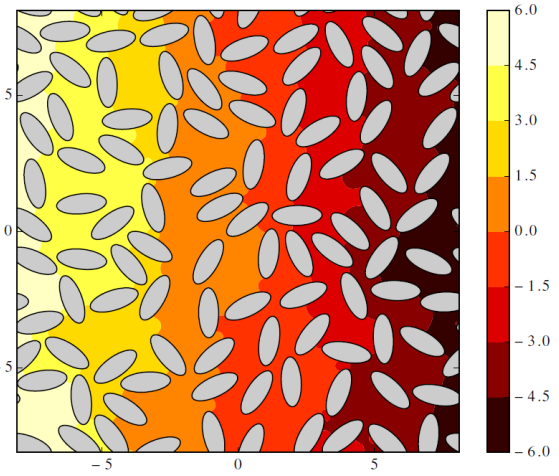


(a) $\sigma = 0.6$

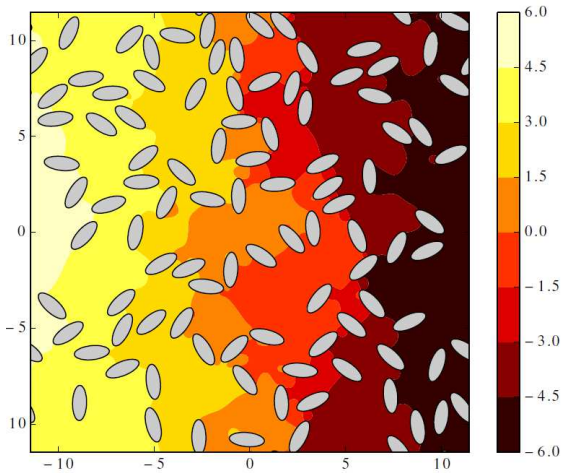


(b) $\sigma = 0.8$

Figure 4.38: Contour plots of pressure of ellipse packs with (a) porosity $\sigma = 0.6$ and (b) 0.8 with $AR = 2.5$ fixed.

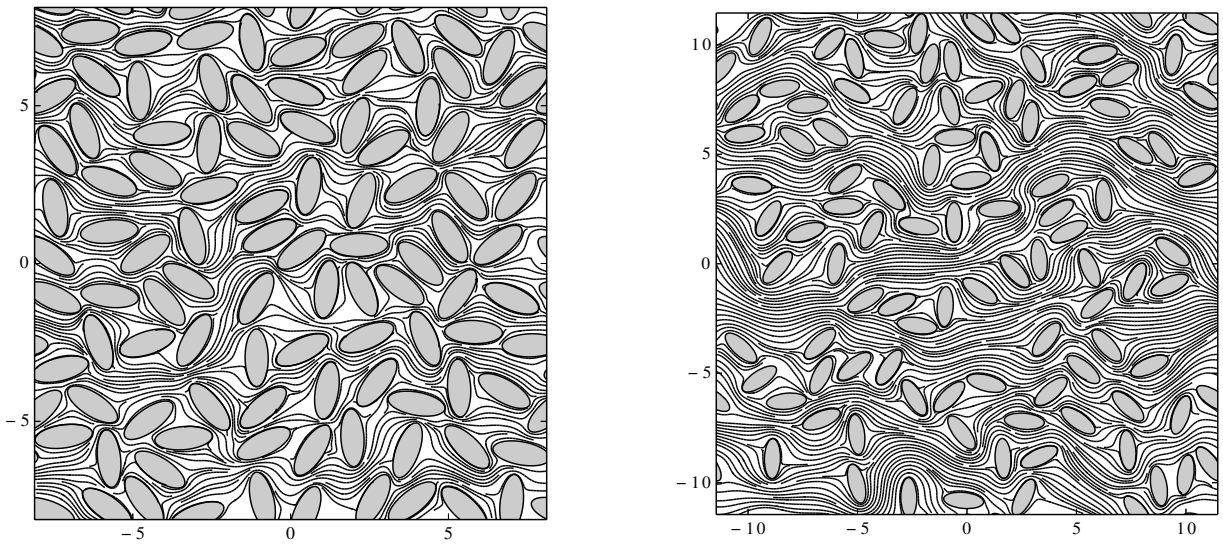


(a) $\sigma = 0.6$ (b) $\sigma = 0.8$

Figure 4.39: Streamlines of pressure of ellipse packs with (a) porosity $\sigma = 0.6$ and (b) 0.8 with $AR = 2.5$ fixed.

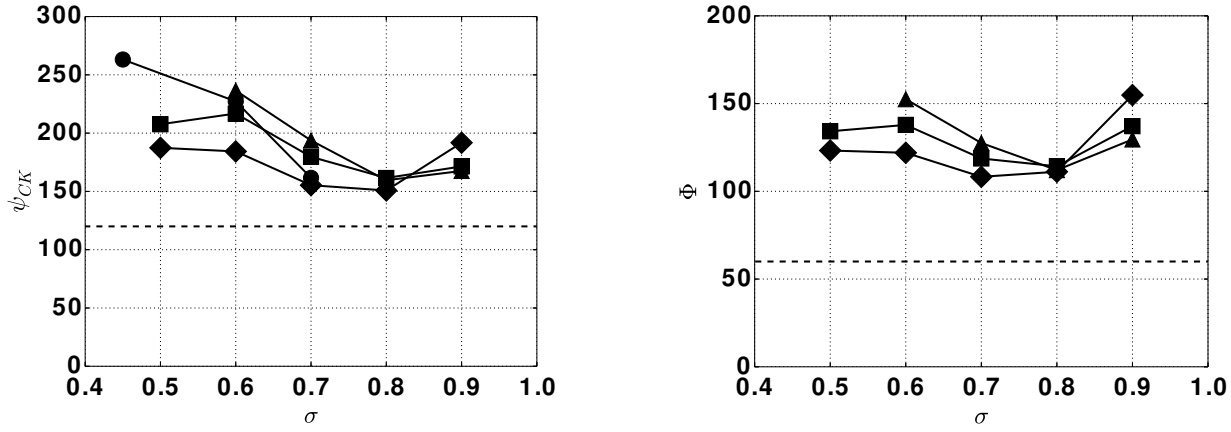


(a) CK factor (b) Shape factor

Figure 4.40: Carman-Kozeny factor $\Psi_{CK}$ and shape factor $\Phi$ as a function of porosity $\sigma$ and aspect ratio $AR$. Here, AR=1.0 (circle); AR=1.5 (diamond); AR=2.5 (square); AR=3.0 (triangle). Also shown is the corresponding factors for slab flow (dashed line).

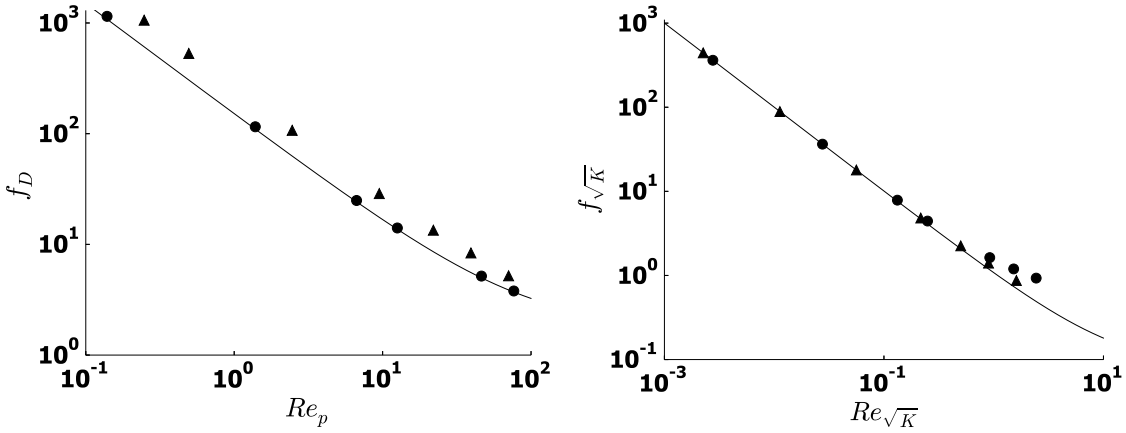


(a) Ergun's equation

(b) Modified Forchheimer equation

Figure 4.41: (a) Plot of friction factor $f_D$ as a function of Reynolds number $Re_p$ (symbols) and Ergun's equation (1.5; solid line). (b) Plot of friction factor $f_{\sqrt{K}}$ as a function of modified Reynolds number $Re_{\sqrt{K}}$ (symbols) and modified Forchheimer equation (3.6; solid line) with $F = 0.08$. Here, $\sigma = 0.45$ (triangle) and 0.7 (circle). Note the difference in scales between the two plots.

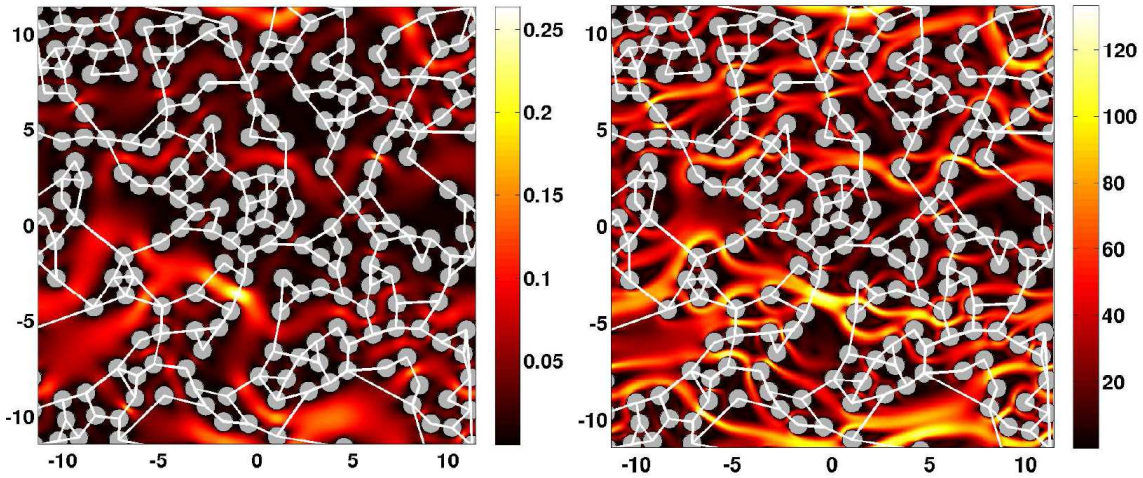


(a) Low $Re$

(b) $Re = 37.8$

Figure 4.42: Contour plot of velocity magnitude for $\sigma = 0.7$ for a monodisperse pack and for two different Reynolds numbers. Also shown as white lines are the shortest edge of each Delaunay triangle. Note the difference in magnitude.

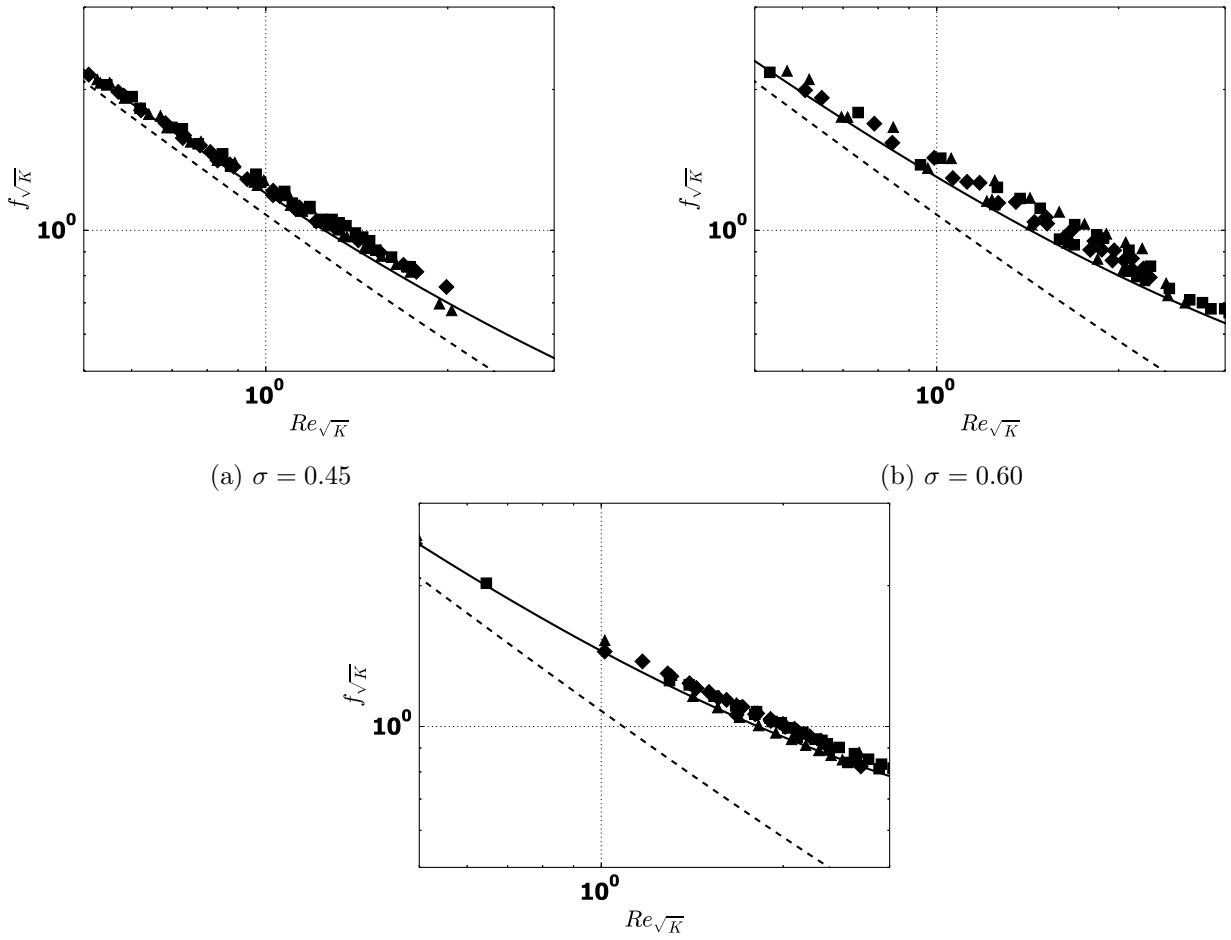


(a) $\sigma = 0.45$

(b) $\sigma = 0.60$

(c) $\sigma = 0.70$

Figure 4.43: Plot of friction factor $f_{\sqrt{K}}$ as a function of modified Reynolds number $Re_{\sqrt{K}}$ at large-to-total particle ratio $\mathcal{N} = 0.25$, 0.50 and 0.75 for porosity (a) $\sigma = 0.45$, (b) 0.60 and (c) 0.70. Here, diameter ratio $D_R = 0.3$ (square), 0.5 (triangle) and 0.7 (diamond). Also shown is the predictions by equation (4.24) (solid line) and F=0.08 (dashed line). The high Reynolds number regions are expanded.

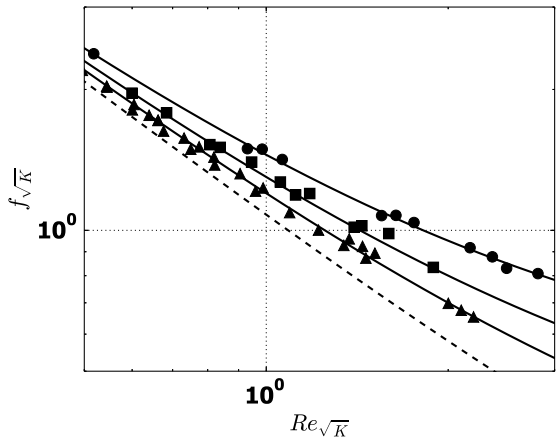


Figure 4.44: Plot of friction factor $f_{\sqrt{K}}$ as a function of modified Reynolds number $Re_{\sqrt{K}}$ for diameter variation $D_\sigma = 0.125$, 0.25, 0.375. Here, porosity $\sigma = 0.45$ (triangle), 0.6 (square), and 0.7 (circle). Also shown is the predictions by equation (4.24) (solid line) and F=0.08 (dashed line). The high Reynolds number regions are expanded.

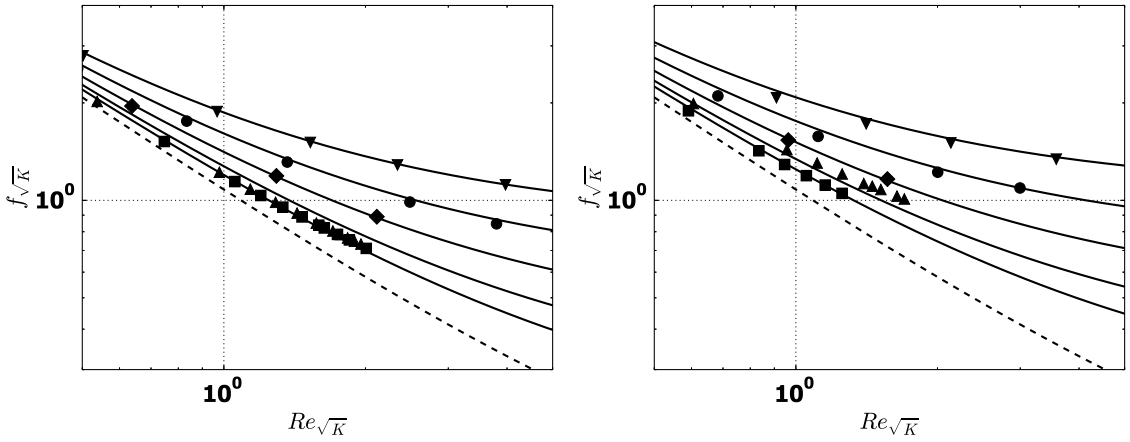


(a) $AR = 1.5$ (b) $AR = 2.5$

Figure 4.45: Plot of friction factor $f_{\sqrt{K}}$ as a function of modified Reynolds number $Re_{\sqrt{K}}$ for aspect ratio (a) $AR = 1.5$ and (b) 2.5, Here, porosity $\sigma = 0.5$ (square), 0.6 (triangle), 0.7 (diamond), 0.8 (circle), and 0.9 (inverted triangle). Also shown is the predictions by equation (4.24) (solid line) and F=0.08 (dashed line). The high Reynolds number regions are expanded.

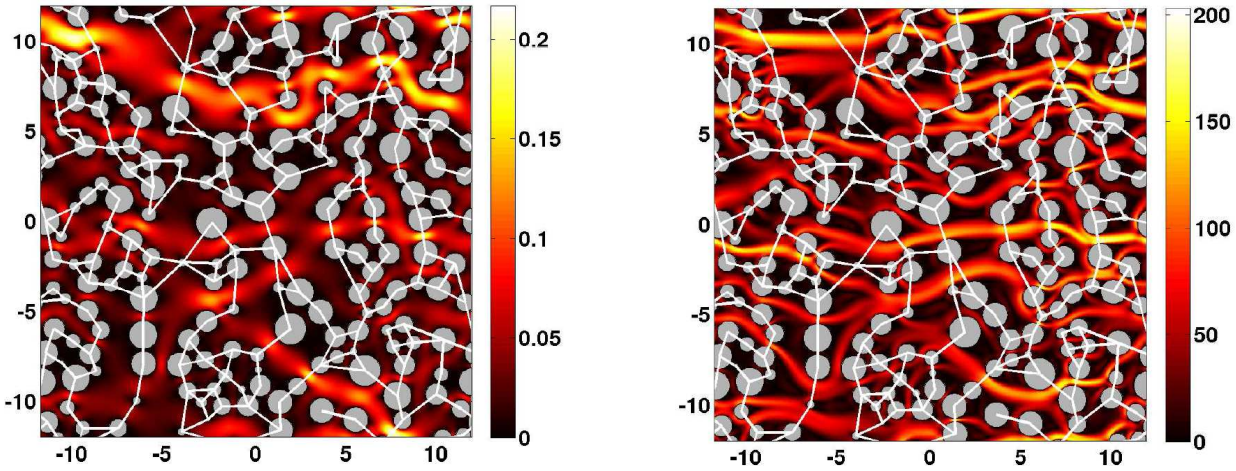


(a) Low $Re$ (b) $Re = 51.9$

Figure 4.46: Contour plot of velocity magnitude for a polydisperse at porosity $\sigma = 0.7$ and diameter variation $D_\sigma = 0.375$, and for two different Reynolds numbers. Also shown as white line segments are the shortest edge of each Delaunay triangle.

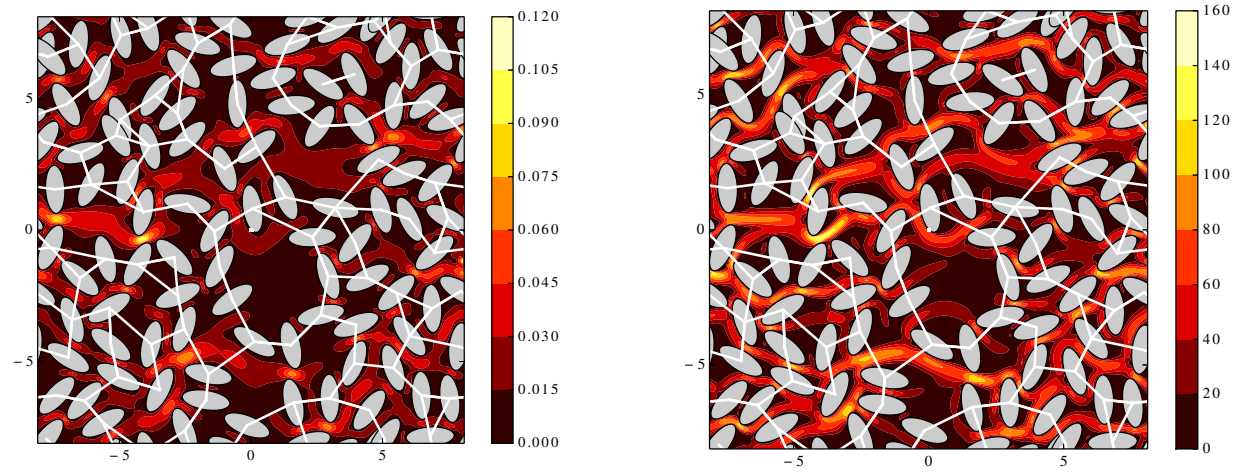


(a) Low $Re$ (b) $Re = 33.4$

Figure 4.47: Contour plot of velocity magnitude for pack of ellipses at porosity $\sigma = 0.6$ and aspect ratio $AR = 2.5$, and for two different Reynolds numbers. Also shown as white line segments are the shortest edge of each Delaunay triangle.

# Chapter 5

# Conclusions and future work

## 5.1 Summary and conclusions

The objectives of this dissertation was firstly; the implementation of the ghost cell immersed boundary method with a Navier-Stokes solver, and secondly; the analysis of fluid flow through random packs of circular or elliptic cylinders with various geometric parameters. The flow is solved using the new solver, and the macroscopic property of the packs, namely the permeability, obtained from the flow solution was examined.

### 5.1.1 The ghost cell immersed boundary method

As presented in the first chapter, the immersed boundary method has been widely used to treat objects immersed into fluid flow on non body-conformal grids. However, its application to flows through porous media is extremely rare. Thus in this dissertation, the ghost cell IB method, one of the variations of the IB method, was coupled with a finite difference based Navier-Stokes solver to analyze the flow with immersed objects. The two-dimensional, unsteady and viscous flow was examined with the new solver. The flow with immersed bodies is solved on the regular, non body-conformal Cartesian grid.

An extensive validation and verification study was carried out on known problems, and

it was shown that the new solver has the expected order of accuracy; third-order in velocity, second-order in pressure, and second-order for the ghost cell method. The solver was also tested on fluid flow with immersed objects. First, the flow past a single object, a standard benchmark for such problems, was solved at steady and unsteady flow regime. The results showed that the drag coefficient, the wake bubble length and the Strouhal number agreed with those from the literature to within about 1.0 %. The flow through an ordered array of cylinders were then solved to test flows through porous media. The tests were conducted on a periodic hexagonal and square array of mono- and bidisperse cylinders at various porosities $\sigma$ and diameter ratios $D_R$, and the friction factors were computed by Ergun's equation and by a modified Forchheimer equation [11]. The obtained friction factors agreed excellently with those by previous work in the range of $Re$, $\sigma$ and $R_D$. Having these problems tested, it has been concluded that the new Navier-Stokes solver has a necessary performance upon the problems of focus in the range of parameters of interest.

### 5.1.2 The permeability of random packs

Once the flow solver has shown its performance, various experiments were conducted on random packs of circular or elliptic cylinders. When analyzing the random packs, it is necessary to carry out ensemble averaging. To determine the sufficient representative volume element size, or RVE, the permeability of monodisperse random packs were computed by varying the ensemble average size $N_r$ and the number of particles $N_p$ at $\sigma = 0.45$ and 0.70. By examining the convergence of the mean permeability, it has been shown that $N_r = 10$ and $N_p = 200$ are sufficient for circular cylinders, and $N_r = 10$ and $N_p = 100$ for ellipses. The RVE chosen here is smaller than those found in the literature, since the current work imposes periodic boundary conditions on the flow domain, which eliminates boundary effects.

The macroscopic parameter of primary interest is the permeability, which is computed from Darcy's law, and normalized by the particle length $L_p$. One purpose is to examine the effects of the pack microstructures on the normalized permeability, such as porosity $\sigma$, polydispersity, numerical fractions of the unique diameters and aspect ratio for ellipses.

The tests have been conducted on random packs of monodisperse, bidisperse, polydisperse cylinders and monodisperse ellipses. For circular cylinders, the porosity was set to be $\sigma$=0.45, 0.60 and 0.70. The bidisperse packs used diameter ratios of $D_R$=0.3, 0.5 and 0.7, with large-to-total particle ratios $\mathcal{N}$ = 0.25, 0.50 and 0.75. For the polydisperse packs, nine unique diameters were employed with standard deviations of diameters $D_\sigma$ = 0.125, 0.25 and 0.375. For the packs of ellipses, $\sigma$=0.50, 0.60, 0.70, 0.80 and 0.90 was used, while aspect ratios of AR = 1.5, 2.5 and 3.0 were selected.

For each set of parameters, the flow field is solved until it reaches steady state, and the permeability computed. It was found that the permeability is highly affected by not just $\sigma$ but also by the pack microstructure; the permeability showed a tendency to increase as the geometry becomes less uniform. To correlate the permeability to some statistical descriptor of microstructure, we employed the mean shortest Delaunay edge, $\gamma_1^T$. With a proper scaling, $\sigma$ and $\gamma_1^T$ of the bidisperse, polydisperse and ellipses can essentially collapse onto monodisperse data, and the scaled permeability can be fitted as a function of the scaled $\gamma_1^T$ to a universal curve. It is also shown that the Carman-Kozeny factors depend on the microstructure, and that the assumption of constant Carman-Kozeny factor for macroscale modeling is highly inaccurate.

Finally, tests have been extended to the higher Reynolds number regime, at which the flow is still steady but the Darcy's law is no longer valid due to the presence of inertial effects. The friction factors correlated by Ergun's equation and the modified Forchheimer equation were calculated and compared with the prediction function. The Ergun's equation is found to be inaccurate especially at low porosities and/or less uniform geometries, whereas the modified Forchheimer equation shows better agreement with the prediction. However, the results still diverge from the prediction at high $Re$ inertial flow regime, so the equation is further modified to have a fitting parameter, which is a function of porosity and particle shape. The new friction factor shows a significant improvement on the prediction in inertial flow regime.

## 5.2 Future work

Although random packs of various geometries have been examined, the current work was limited to two-dimensional flow through random packs of regular shapes in the relatively low Reynolds number at middle to high porosities. The details of the flow through more realistic materials, such as polyhedral crystals and at lower porosities and/or high Reynolds numbers, were out of scope of this dissertation. The current solver is capable of handling those geometries in two-dimensional flow, however, little is known about the flow behavior through non-trivial shapes. This suggests that a more comprehensive statistical analysis is still needed.

Another extension of the current work is to modify the current solver to three-dimensional flows. Although it is relatively easy to implement the three-dimensional ghost cell method, it is still challenging to update the code, especially when there is a need to handle complex shapes. Since three-dimensional flows through random packs of non-trivial shape objects are still an active field of research, an ultimate goal of our work would be to establish more global correlations of the macroscopic property and the geometric descriptors of the packs of complex shapes on three-dimensional flows.

# Appendix A

# Drag computation

To analyze the performance of a packed bed, it is also important to measure the total drag of the bed. For a simple problem like flow with one or a few immersed bodies, the drag is usually computed from the pressure and viscous forces acting along the surface of the body. However in the present work, there could be multiple particles with random shapes and locations throughout the domain, which significantly complicate the calculation on each body. Thus, alternatively, it is more appropriate to compute the force on the control volume.

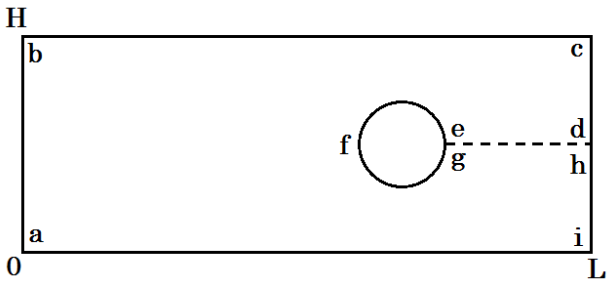


Figure A.1: Schematic of a control volume containing the flow domain

Figure A.1 is a schematic of the flow domain and the corresponding control volume. Here it shows only a single object for simplicity. The momentum equation is given by

$$(\rho\vec{u})_t + \nabla \cdot (\rho\vec{u}) = \nabla \cdot \underline{\underline{\sigma}}. \tag{A.1}$$

The force acting on the fluid due to the body can be written as

$$F_{fluid} = \sum_{i=1}^{N} \int_{efg} (\underline{\underline{\sigma}} \bullet \hat{n}) \bullet \overrightarrow{e_x} dS \tag{A.2}$$

where $N$ is the number of bodies in the control volume and S is the surface. By substituting equation (A.1) into (A.2), the momentum equation integrated over the whole control volume can be written as;

$$\iint_{abcia} \frac{\partial(\rho u)}{\partial t} dA + \oint_{abcia} [(\rho \vec{u}\vec{u} - \underline{\underline{\sigma}}) \bullet \hat{n}] \bullet \overrightarrow{e_x} dS - F_{fluid} = 0 \tag{A.3}$$

where $F_{fluid}$ is a sum of the drag acting on the immersed bodies. In the present work, the boundary conditions at top and bottom of the domain are set to be either periodic or solid wall, so the forces due to the momentum flux and the viscous stress in y-direction on the domain boundaries cancel each other or zero. The remaining terms can be now solved for $F_{fluid}$ as

$$\begin{aligned} F_{fluid} = & \iint_{A} \frac{\partial(\rho u)}{\partial t} dA + \int_0^H (\rho_L u_L^2 - \rho_0 u_0^2) dy + \\ & \int_0^H (p_L - p_0) dy + \int_0^H (\tau_{xx,0} - \tau_{xx,L}) dy + \int_0^L (\tau_{xy,bot} - \tau_{xy,top}) dy \end{aligned} \tag{A.4}$$

The above equation is normalized by the same reference variables as the governing equations. This leads the normalized stress terms $\tau$ to

$$\tau_{xx} = \frac{2}{Re} \frac{\partial u}{\partial x} \tag{A.5}$$

$$\tau_{xy} = \frac{1}{Re} \left[ \frac{\partial u}{\partial y} + \frac{\partial v}{\partial x} \right] \tag{A.6}$$

Finally, the drag coefficient is given as

$$C_D = \frac{F_{fluid}^{dimensional}}{\frac{1}{2}\rho U^2 L_p} = 2F_{fluid}^{nondimensional} \tag{A.7}$$

It is notable that, since this equation is independent on the geometry of immersed bodies, it is applicable to flow with any immersed bodies, from a single and simple shape to a pack of random shape particles. As presented on Section 3.3, the control volume approach for the drag coefficient has been employed for flows past a single object and validated by comparison with literature.

# Appendix B

# Lubrication theory

The flow between two cylinders can be correlated to interparticle spacing by the lubrication theory as shown on equation (4.7). Derivation of the equation was presented on for monodisperse and on [94, 95] for bidisperse packs. In this section, the derivation is represented for bidisperse and ellipses.

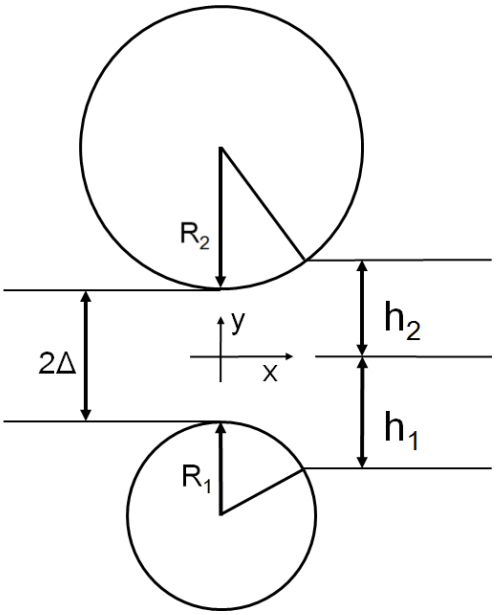


(a) Bidisperse cylinders

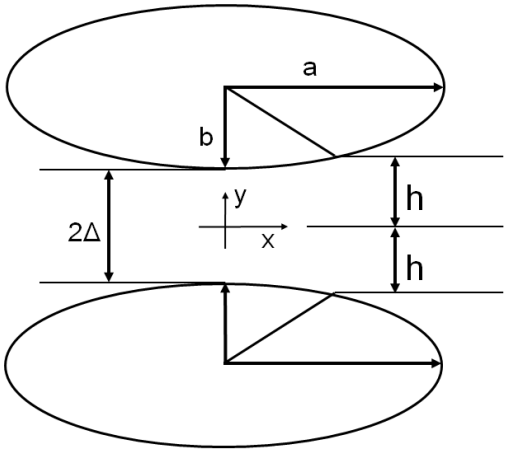


(b) Monodisperse ellipses

Figure B.1: Schematics of the coordinate system and the inters pacing between (a) bidisperse cylinders, and (b) monodisperse ellipses.

The schematics of the coordinates and corresponding lengths for a pair of bidisperse cylinders and monodisperse ellipses are shown on Figure B.1. The velocity between two cylinders can be expressed by a well known pipe flow, given as;

$$u(x,y) = Re\frac{h^2}{2}\frac{dp}{dx}\left(\frac{y^2}{h^2} - 1\right) \tag{B.1}$$

Note that equation (B.1) is normalized accordingly, and all the equations in the following sections are normalized as well. Integrating equation (B.1) with respect to y-axis yields;

$$q(y) = -Re\frac{2h^3}{3}\frac{dp}{dx} \tag{B.2}$$

where $q(y)$ is the volumetric flow rate per unit length. Solving it for $dp/dx$;

$$\frac{dp}{dx} = -\frac{3}{2}\frac{q}{h^3(x)Re} \tag{B.3}$$

Now, the distance between the centerline between two cylinders and surface of the cylinder $h(x)$ can be written and simplified by the second degree polynomial approximation as

$$\begin{aligned} h &= \Delta + R\left(1 - \sqrt{1 - \frac{x^2}{R^2}}\right) \\ &\simeq \Delta\left(1 + \frac{x^2}{2R\Delta}\right) \end{aligned} \tag{B.4}$$

Substituting equation (B.4) into equation (B.3), it can be integrated by changing a variable as;

$$\Delta p = -\frac{3}{2}\frac{q}{Re}\int_{x_2/\sqrt{2R\Delta}}^{x_1/\sqrt{2R\Delta}} \frac{dt}{(1+t^2)^3} \tag{B.5}$$

The solution now depends on the width of the interval at which the pressure drop is measured. It is stated on [94] that since the integrand drops rapidly as the distance from the origin increases, and the characteristic length of the integral $\sqrt{2R\Delta}$ is much smaller than R, it is possible to take the integral limits to be $\pm\infty$ with minimum loss of accuracy. This gives the solution of the integral as $3\pi/8$, so the the pressure drop across the length between fibers $L$ is yielded as;

$$\frac{\Delta p}{L} = -\frac{9\pi}{16L}\frac{q\sqrt{2L_p}}{Re}\Delta^{-5/2} \tag{B.6}$$

Finally, the permeability is determined from the Darcy's law as;

$$K = \frac{16Re}{9\pi\sqrt{2L_p}}\Delta^{5/2} \tag{B.7}$$

Here, note that since the lengths are scaled by $L_p$ and $\Delta$ is half a distance between cylinders, $2\Delta$ is equivalent to $\gamma$ as defined on Table 4.2 (notice that $\gamma_1 = \gamma_1^T$ for a pair of two cylinders), it shows that $K \sim \gamma^{5/2}$, confirming the exponent 2.5 of equation (4.7). In the similar fashion, the pressure drop across two bidisperse cylinders was derived on [95]. The distance $h(x)$ for bidisperse cylinders is given as

$$\begin{aligned} h_i &= \Delta + R_i\left(1 - \sqrt{1 - \frac{x^2}{R_i^2}}\right) \\ &\simeq \Delta\left(1 + \frac{x^2}{2R_i\Delta}\right) \end{aligned} \tag{B.8}$$

where i=1,2 for bidisperse cylinders. By applying $h(x)$, equations (B.6) and (B.7) can be rewritten as;

$$\frac{\Delta p}{L} = -\frac{9\pi}{8L}\frac{q\sqrt{2L_p}}{Re}\Delta^{-5/2}\frac{\sqrt{D_R}}{D_R+1} \tag{B.9}$$

$$K' = \frac{8Re}{9\pi\sqrt{2L_p}}\Delta^{5/2}\frac{D_R+1}{\sqrt{D_R}} \tag{B.10}$$

Notice that these equations are equivalent to equations (B.6) and (B.7) when $D_R = 1.0$. Hence, the permeability is correlated to $\gamma$ by exponent 2.5 for bidisperse cylinders. Finally, for a pack of ellipses, $h(x)$ is given as;

$$\begin{aligned} h &= \Delta + b\left(1 - \sqrt{1 - \frac{x^2}{a^2}}\right) \\ &\simeq \Delta\left(1 + \frac{bx^2}{2\Delta a^2}\right) \\ &= \Delta\left(1 + \frac{x^2}{2\Delta aAR}\right) \end{aligned} \tag{B.11}$$

This yields the permeability as;

$$K' = \frac{16Re}{9\pi\sqrt{2aAR}}\Delta^{5/2}, \tag{B.12}$$

which again has an exponent of 2.5. From these derived correlations, it is shown that the exponent 2.5 of equation (4.7) is valid not only for a pack of monodisperse cylinders but also bidisperse (and polydisperse) cylinders as well as monodisperse ellipses. In the current

work, the new correlation of the permeability to $\gamma_1^T$ (equation (4.8)) has an exponent slightly larger than 2.5. This difference is expected to be due to the random orientations.

# Bibliography

[1] Mattis, S.A., Dawson, C.N., Kees, C.E., and Farthing, M.W. (2012). Numerical modeling of drag for flow through vegetated domains and porous structures. Advances in Water Resources, Vol. 39, pp. 44-59.

[2] Jafari, A., Zamankhana, P., Mousavi, S. and Pietarinen, K. (2008). Modeling and CFD simulation of flow behavior and dispersivity through randomly packed bed reactors. Chemical Engineering Journal. Vol. 144, pp. 476-482.

[3] Keyser, M.J., Conradie, M., Coertzen, M., and Van Dyk, J.C. (2006). Effect of coal particle size distribution on packed bed pressure drop and gas flow distributions. Fuel, Vol. 85, pp. 1439-1445.

[4] Darcy, H. (1856). Les Fontaines Publiques de la Ville de Dijon, Dalmont, Paris.

[5] Forchheimer, P. (1901). Wasserbewegung durch Boden. Z. Ver. Deutsch Ing., Vol. 45, p. 1781.

[6] Zeng, Z. and Grigg, R. (2006). A criterion for non-Darcy flow in porous media. Transport in Porous Media, Vol. 63, pp. 57-69.

[7] Yang, Y.B., Nasserzadeh, V., Goodfellow, J. and Swithenbank, J. (2003). Simulation of channel growth in a burning bed of solids. Chemical Engineering Research and Design, Vol. 81(2), pp. 221-232.

[8] Nield, D. (1994). Modelling high speed flow of a compressible fluid in a saturated porous medium. Transport in Porous Media, Vol. 14, pp. 85-88.

[9] Ergun, S. (1952). Fluid flow through packed columns. Chemical Engineering Progress, Vol. 48, p. 89.

[10] Green, D. and Perry, R. (2008). Perry's Chemical Engineers' Handbook, 8th Edition. McGraw-Hill Professional, New York.

[11] Papathanasiou, T.D., Markicevic, B. and Dendy, E.D. (2001). A computational evaluation of the Ergun and Forchheimer equations for fibrous porous media. Physics of Fluids, Vol. 13(10), pp. 2795-2804.

[12] MacDonald, I.F., El-Sayed, M.S., Mow, K. and Dullien, F.A.L. (1979). Flow through porous media - the Ergun equation revisited. Ind. Eng. Chem. Fundam., Vol. 18(3), pp. 199-208.

[13] Comiti, J. and Renaud, M. (1989). A new model for determining mean structure parameters of fixed beds from pressure drop measurements: Application to beds packed with parallelepipedal particles. Chemical Engineering Science, Vol. 44(7), pp. 1539-1545.

[14] Martin, A.R., Saltiel, C. and Shyy, W. (1998). Frictional losses and convective heat transfer in sparse, periodic cylinder arrays in cross flow. International Journal of Heat and Mass Transfer, Vol. 41(15), pp. 2382-2397.

[15] Sangani, A.S. and Yao, C. (1988). Transport processes in random arrays of cylinders. II. Viscous flow. Phys. Fluids, Vol. 31(9), pp. 2435-2444.

[16] Narvaez, A., Yazdchi, K., Luding, S. and Harting, J. (2013). From creeping to inertial flow in porous media: a lattice Boltzmann-finite element study. Journal of Statistical Mechanics: Theory and Experiment, January 2013, P02038.

[17] Koch, D.L. and Ladd, A.J.C. (1997). Moderate Reynolds number flows through periodic and random arrays of aligned cylinders. Journal of Fluid Mechanics, Vol. 349, pp. 31-66.

[18] Gunjal, P.R., Ranade, V.V. and Chaudhari, V. (2005). Computational study of a single-phase flow in packed beds of spheres. Fluid Mechanics and Transport Phenomena, AIChE Journal, Vol. 51(2), pp. 365-378.

[19] Nagelhout, D., Bhat, M.S., Heinrich, J.C. and Poirier, D.R. (1995). Permeability for flow normal to sparse array of fibers. Materials Science and Engineering, Vol. 191, pp. 203-208.

[20] Clague, D.S. and Phillips, R.J. (1997). A numerical calculation of the hydraulic permeability of three-dimensional disordered fibrous media. Physics of Fluids, Vol. 9(6), pp. 1562-1572.

[21] Maier, R.S., Kroll, D.M., Davis, H.T. and Bernard, R.S. (1999). Simulation of flow in bidisperse sphere packings. Journal of Colloid and Interface Science, Vol. 217, pp. 341-347.

[22] van der Hoef, M.A., Beetstra, R. and Kuipers, J.A.M. (2005). Lattice-Boltzmann simulations of low Reynolds-number flow past mono- and bidisperse arrays of spheres: results for the permeability and drag force. Journal of Fluid Mechanics, Vol. 528, pp. 233-254.

[23] Beetstra, R., van der Hoef, M.A. and Kuipers, J.A. (2007). Drag force of intermediate Reynolds number flow past mono- and bidisperse arrays of sphere. Fluid Mechanics and Transport Phenomena, Vol. 53(2), pp. 489-501.

[24] Garcia, X., Akanji, L.T., Blunt, M.J., Matthai, S.K. and Latham, J.P. (2009). Numerical study of the effects of particle shape and polydispersity on permeability. Physical Review E, Vol. 80, 021304.

[25] Yin, X. and Sundaresan, S. (2009). Drag law for bidisperse gas-solid suspensions containing equally sized spheres. Ind. Eng. Chem. Res., Vol. 28, pp. 227-241.

[26] Liu, H.L. and Hwang, W.R. (2012). Permeability prediction of fibrous porous media with complex 3D architectures. Composites: Part A, Vol. 43, pp. 2030-2038.

[27] Jiang, P. and Lu, X. (2007). Numerical simulation and theoretical analysis of thermal boundary characteristics of convection heat transfer in porous media. International journal of Heat and Fluid Flow, Vol. 28, pp. 1144-1156.

[28] Rochette, D. and Clain, S. (2006). Two-dimensional computation of gas flow in a porous bed characterized by a porosity jump. Journal of Computational Physics, Vol. 219, pp. 104-119.

[29] Mousavi, S.M., Jafari, A., Yaghmaei, S., Vossoughu, M. and Sarkomaa, P. (2006). Computer simulation of fluid motion in a porous bed using a volume of fluid method: Application in heap leaching. Minerals Engineering, Vol. 19, pp. 1077-1083.

[30] Biswal, B., Manwart, C. and Hilfer, R. (1998). Three-dimensional local porosity analysis of porous media. Physica A, Vol. 255, pp. 221-241.

[31] Oren, P.E., Bakke, S. and Held, R. Direct pore-scale computation of material and transport properties for North Sea reservoir rocks. Water Resources Research, Vol. 43, W12S04.

[32] Lehmann, P., Berchtold, M., Ahrenholz, B., Tolke, J., Kaestner, A., Krafczyk, M., Fluhler, H. and Kunsch, H.R. (2008). Impact of geometrical properties on permeability and fluid phase distribution in porous media. Advances in Water Resources, Vol. 31, pp. 1188-1204.

[33] Ghassemi, A. and Pak, A. (2011). Pore scale study of permeability and tortuosity for flow through particulate media using Lattice Boltzmann method. International Journal for Numerical and Analytical Methods in Geomechanics, Vol. 35, pp. 886-901.

[34] Schwartz, L.M. and Banavar, J.R. (1989). Transport properties of disordered continuum systems. Physical Review B, Vol. 39(16), pp. 11965-11971.

[35] Pilotti, M. (1998). Generation of realistic porous media by grains sedimentation. Transport in Porous Media, Vol. 33, pp. 257-278.

[36] Coelho, D., Thovert, J.F., and Adler, P.M. (1997). Geometrical and transport properties of random packings of spheres and aspherical particles. Physical Review E, Vol. 55(2), pp. 1959-1978.

[37] Yazdchi, K., Srivastava, S. and Luding, S. (2011). Microstructural effects on the permeability of periodic fibrous porous media. International Journal of Multiphase Flow, Vol. 37, pp. 956-966.

[38] Yazdchi, K. and Luding, S. (2012). Towards unified drag laws for inertial flow through fibrous materials. Chemical Engineering Journal, Vol. 207-208, pp. 35-48.

[39] Chen, X. and Papathanasiou, T.D. (2008). The transverse permeability of disordered fiber arrays: a statistical correlation in terms of the mean nearest interfiber spacing. Transport in Porous Media, Vol. 71, pp. 233-251.

[40] Araujo, A.D., Bastos, W.B., Andrade, J.S. and Herrmann, H.J. (2006). Distribution of local fluxes in diluted porous media. Physical Review E, Vol. 74, 010401.

[41] Yazdchi, K., Srivastava, S. and Luding, S. (2012). Micro-macro relations for flow through random arrays of cylinders. Composites: Part A, Vol. 43, pp. 2007-2020.

[42] Yazdchi, K. and Luding, S. (2013). Upscaling and microstructural analysis of the flow-structure relation perpendicular to random, parallel fiber arrays. Chemical Engineering Science, Vol. 98, pp. 173-185.

[43] Peskin, C. S. (1972). Flow patterns around heart valves: a digital computer method for solving the equations of motion, PhD thesis. Physiol., Albert Einstein Coll. Med., Univ. Microfilms. 378:72-30.

[44] Mittal, R. and Iaccarino, G. (2005). Immersed boundary methods. Annual Review of Fluid Mechanics, Vol. 37, pp. 239-261.

[45] Sotiropoulos, F., Yang, X. (2014). Immersed boundary methods for simulating fluid structure interaction. Progress in Aerospace Sciences, Vol. 65, pp. 1-21.

[46] Peskin, C. S. (1981). The fluid dynamics of heart valves: experimental, theoretical and computational methods. Annual Review of Fluid Mechanics, Vol. 378, pp. 235-259.

[47] Beyer, R. P., Leveque, R. J. (1992). Analysis of a one-dimensional model for the immersed boundary method. Journal of Numerical Analysis, Vol. 29(2), pp. 332-364.

[48] Lai, M. C., Peskin, C. S. (2000). An immersed boundary method with formal second-order accuracy and reduced numerical viscosity. Journal of Computational Physics. Vol. 160, pp. 705-719.

[49] Goldstein, D., Handler, R., Sirovich, L. (1993). Modeling a no-slip flow boundary with an external force field. Journal of Computational Physics, Vol. 105, pp. 354-366.

[50] Angot, P., Bruneau, C. H., Fabrie, P. (1999). A penalization method to take into account obstacles in incompressible viscous flows. Numerical Mathematik. Vol. 81, pp. 497-520.

[51] Khadra, K., Angot, P., Parneix, S., Caltagirone, J. P. (2000). Fictious domain approach for numerical modeling of Navier-Stokes equations. International Journal for Numerical Methods in Fluids, Vol. 34, pp. 651-684.

[52] Stockie, J. M., Wetton, B. T. R. (1995). Stability analysis for the immersed fiber problem. Journal of Applied Mathematics, Vol. 55(6), pp. 1577-1591.

[53] Stockie, J. M., Wetton, B. R. (1999). Analysis of Stiffness in the immersed boundary method and implications for time-stepping schemes. Journal of Computational Physics, Vol. 154, pp. 41-64.

[54] Peskin, C. S. (2002). The immersed boundary method. Acta Numerica, pp. 479-517.

[55] Mohd-Yusof, J. (1997). Annual Research Briefs, Center for Turbulence Research, pp. 317-328.

[56] Verzicco, R., Mohd-Yusof, J., Orlandi, P., Haworth, D. (2000). Large eddy simulation in complex geometric configurations using boundary body forces. AIAA Journal, Vol.38, No.3, 427-733

[57] Fadlun, E. A., Verzicco, R., Mohd-Yusof, J., Orlandi, P. (2000). Combined immersed-boundary finite-difference methods for three-dimensional complex flow simulations. Journal of Computational Physics, Vol. 161, pp. 35-60.

[58] Majumdar, S., Iaccarino, G., Durbin, P. (2001). RANS solvers with adaptive structured boundary non-conforming grids. Annual Research Briefs, Center for Turbulence Research, pp. 353-366.

[59] Tseng, Y. H., Ferziger, J. H. (2003). A ghost-cell immersed boundary method for flow in complex geometry. Journal of Computational Physics, Vol. 192, pp. 593-623.

[60] Zhang, N., Zheng, Z. C. (2007). An improved direct-forcing immersed-boundary method for finite difference applications. Journal of Computational Physics, Vol. 221, pp. 250-268.

[61] Mittal, R., Dong, H., Bozkurttas, M., Najjar. F.M., Vargas, A. and von Loebbecbe, A. (2008). A versatile sharp interface immersed boundary method for incompressible flows with complex boundaries. Journal of Computational Physics, Vol. 227, pp. 4825-4852.

[62] Wang, W., Pletcher, R. (2007). Large eddy simulation of compressible flows in a rectangular duct containing cylindrical rods - an immersed boundary treatment. AIAA Aerospace Science Meeting and Exhibit, AIAA Paper No. 921

[63] Ghias, R., Mittal, R., Lund, T. S. (2004). A non-body conformal grid method for simulation of compressible flows with complex immersed boundaries. AIAA Aerospace Science Meeting and Exhibit, AIAA Paper No. 0080.

[64] Clarke, D. K., Salas, M. D., Hassan, H. A. (1986). Euler calculations for multielement airfoils using Cartesian grids. AIAA Journal, Vol. 24(3), pp. 353-358.

[65] Ye, T., Mittal, R., Udaykumar, H. S., Shyy, W. (1999). An accurate Cartesian grid method for viscous incompressible flows with complex immersed boundaries. Journal of Computational Physics, Vol. 156, pp. 209-240.

[66] Udaykumar, H. S., Shyy, W., Rao, M. M. (1996). ELAFINT: A mixed Eulerian-Lagrangian method for fluid flows with complex and moving boundaries. International Journal for Numerical Methods in Fluids, Vol. 22, pp. 691-712.

[67] Kirkpatrick, M. P., Armfield, S. W., Kent, J. H. (2003). A representation of curved boundaries for the solution of the Navier-Stokes equations on a staggered three-dimensional Cartesian grid. Journal of Computational Physics, Vol. 184, pp. 1-36.

[68] Meyer, M., Devesa, A., Hickel, S., Hu, X. Y., Adams, N. A. (2010). A conservative immersed interface method for Large-Eddy simulation of incompressible flows. Journal of Computational Physics, Vol. 229, pp. 6300-6317.

[69] Clague, D. S., Kandhai, B. D., Zhang, R., Sloot, P. M. A. (2000). Hydraulic permeability of (un)bounded fibrous media using the lattice Boltzmann method. Physical Review, Vol. 61(1), pp. 616-625.

[70] Hu, F.Q., Hussaini, M.Y. and Manthey, J.L. (1996). Low-Dissipation and Low-Dispersion Runge–Kutta Schemes for Computational Acoustics. Journal of Computational Physics, Vol. 124, pp. 177–191.

[71] Adams, J. (1989). Multigrid fortran software for the efficient solution of linear elliptic partial differential equations. Appl. Math. Comput., Vol. 34, pp. 113-146.

[72] Liu, X. D., Osher, S. and Chan, T. (1994). Weighted Essentially Non-oscillatory Schemes. Journal of Computational Physics, Vol.115, pp.200-212

[73] Jiang, G.S. and Shu, C. W. (1996). Efficient implementation of weighted ENO schemes. Journal of Computational Physics, Vol. 126, pp. 202-228.

[74] Shu, C. W. (1998). Essentially non-oscillatory and weighted essentially non-oscillatory schemes for hyperbolic conservation laws. Lecture Notes in Mathematics, Vol. 1697, pp 325-432.

[75] Jiang, G.S. and Peng, D. (2000). Weighted ENO schemes for Hamilton-Jacobi equations. Society for Industrial and Applied Mathematics, Vol 21(6), pp.2126-2143.

[76] Knott, G.M., Jackson, T.L. and Buckmaster, J. (2001). Random packing of heterogeneous propellants. AIAA Journal, Vol. 39(4), pp. 678-686.

[77] Kochevets, S., Buckmaster, J., Jackson, T.L. and Hegab, A. (2001). Random propellant packs and the flames they support. Journal of Propulsion and Power, Vol. 17(4), pp. 883-891.

[78] Maggi, F., Stafford, S., Jackson, T.L. and Buckmaster, J. (2008). Nature of packs used in propellant modeling. Physical Review E, Vol. 77, 046107.

[79] Lubachevsky, B.D. and Stillinger, F.H. (1990). Geometric properties of random disk packings. Journal of Statistical Physics, Vol. 60(5), pp. 561-583.

[80] Stafford, D.S. and Jackson, T.L. (2010). Using level sets for creating virtual random packs of non-spherical convex shapes. Journal of Computational Physics, Vol. 229, pp. 3295-3315.

[81] Jackson, T.L., Hooks, D.E. and Buckmaster, J. (2011). Modeling the microstructure of energetic materials with realistic constituent morphology. Propellants, Explosives, Pyrotechnics, Vol. 36(3), pp. 252-258.

[82] Zhang, J. and Jackson, T.L. (2009). A high-order incompressible flow solver with WENO. Journal of Computational Physics, Vol. 228, pp. 2426-2442.

[83] Kim, D. H., Yang, K. S., Senda, M. (2004). Large eddy simulation of turbulent flow past a square cylinder confined in a channel. Computers and Fluids, Vol. 33, pp. 81-96.

[84] Ol'shanskii, M. A., Staroverov, V. M. (2000). On simulation of outflow boundary conditions in finite difference calculations for incompressible fluid. International Journal for Numerical Methods in Fluids. Vol. 33, pp. 499-534.

[85] Dennis, S.C.R. and Chang, G. (1970). Numerical solutions for steady flow past a circular cylinder at Reynolds numbers up to 100. Journal of Fluid Mechanics, Vol. 42, pp. 471-489.

[86] Ye, T., Mittal, R., Udaykumar, H.S., Shyy, W. (1999). An accurate Cartesian grid method for viscous incompressible flows with complex immersed boundaries. Journal of Computational Physics, Vol. 156, pp. 209-240.

[87] Wang, X. and Jackson, T.L. (2005). The numerical simulation of two-dimensional aluminized composite solid propellant combustion. Combustion Theory and Modelling, Vol. 9, pp. 171-197.

[88] Okajima, A., Yi, D., Sakuda, A., and Nakano, T. (1997). Numerical study of blockage effects on aerodynamic characteristics of an oscillating rectangular cylinder. Journal of Wind Engineering and Industrial Aerodynamics, Vol. 67, pp. 91-102.

[89] Robichaux, J., Balachandar, S. and Vanka, S.P. (1999). Three-dimensional Floquet instability of the wake of square cylinder. Physics of Fluids, Vol. 11(3), pp. 560-578.

[90] Sharma, A. and Eswaran, V. (2004). Heat and fluid flow across a square cylinder in the two-dimensional laminar flow regime. Numerical Heat Transfer, Part A, Vol. 45, pp. 247-269.

[91] Yoon, D., Yang, K and Choi, C. (2010). Flow past a square cylinder with an angle of incidence. Physics of Fluids, Vol. 22, Article No. 043603.

[92] Koponen, A., Kataja, M. and Timonen, J. (1996). Tortuous flow in porous media. Physical Review E, Vol. 54(1), pp. 406-410.

[93] Nabovati, A. and Sousa, A.C.M. (2007). Fluid flow simulation in random porous media at pore level using the lattice Boltzmann method. Journal of Engineering Science and Technology, Vol. 2(3), pp. 226-237.

[94] Gebart, B.R. (1992). Permeability of unidirectional reinforcements for RTM. Journal of Composite Materials, Vol. 26(8), pp. 1100-1133.

[95] Lundstrom, T.S. and Gebart, B.R. (1995). Effect of perturbation of fibre architecture on permeability inside fibre tows. Journal of Composite Materials, Vol. 29(4), pp. 424-443.

[96] Tamayol, A., Wong, K.W., and Bahrami, M. (2012). Effects of microstructure on flow properties of fibrous porous media at moderate Reynolds number. Physical Review E, Vol. 85, 026318.